SURFACE MICROSTRUCTURE AND ITS EFFECT ON ELECTRODE RESPONSE

By

MICHAEL S. FREUND

A DISSERTATION PRESENTED TO THE GRADUATE SCHOOL
OF THE UNIVERSITY OF FLORIDA IN PARTIAL FULFILLMENT
OF THE REQUIREMENTS FOR THE DEGREE OF
DOCTOR OF PHILOSOPHY

UNIVERSITY OF FLORIDA

1992

I dedicate this work and dissertation to my family who have given me continuous unconditional support.

ACKNOWLEDGEMENTS

I would like to sincerely thank my chairperson, Dr. Anna Brajter-Toth, for her encouragement and support. She has been a tremendous source of knowledge and ideas while at the same time encouraging the development of individual ideas and solutions to scientific problems. She has always been there to provided focus and guidance.

I am most appreciative to the members of my committee, Dr. J. Winefordner, Dr. V. Young, Dr. D. Talham, and Dr. C. Batich. I am indebted to Dr. T. Cotton, Dr. E. Hendrickson, Dr. K. Oldham, and Dr. M. Ward for providing research opportunities and support. I would also like to express my thanks to Chen-Chan Hsueh for help with computer programming. I wish to acknowledge financial support of this work through the Joseph W. Richards Fellowship of the Electrochemical Society and the Shell Fellowship.

I would also like to thank all my friends and colleagues, especially Cecilia Basic, Liakatali Bodalbhai, Stacey Boyette, Kevin McKenna, Stephanie Myers, Kevin Volk and Allan Witkowski for their help and support.

TABLE OF CONTENTS

Page

ACKNOWLEDGEMENTS iii

LIST OF TABLES vii

LIST OF FIGURES viii

KEY TO SYMBOLS xiii

ABSTRACT xv

CHAPTERS

1 INTRODUCTION 1

1.1 Background 1
1.2 Mass Transport at Microelectrode Arrays 6
1.3 Mediation and Adsorption at Electrode Surfaces 18
1.4 Structural and Chemical Properties of Graphite 25
1.5 Structural and Chemical Properties of Tetrathiafulvalene-Tetracyanoquinodimethane (TTF-TCNQ) 29
1.6 Scope of the Dissertation 32

2 EXPERIMENTAL 35

2.1 Materials 35
2.2 Electrochemical Apparatus 35
2.3 Experimental Procedures 36
2.3.1 Electrode Preparation 36
2.3.1.1 Platinum 36
2.3.1.2 Rough pyrolytic graphite 36
2.3.1.3 Glassy carbon 37
2.3.1.4 TTF-TCNQ 37
2.3.2 Electrochemical Techniques 46
2.3.2.1 Cyclic and linear sweep voltammetry 46
2.3.2.2 Rotating disk electrode 47
2.3.2.3 Chronocoulometry and chronoamperometry 48
2.3.2.4 Decoration of electroactive areas by electrochemical copper deposits 50
2.3.3 Other Techniques 50

2.3.3.1 Quartz crystal microbalance 50
2.3.3.2 Scanning tunneling and atomic force microscopy 53
2.4 Numerical Methods 54
2.4.1 Simulation of Current Response at Microelectrode Arrays 54
2.4.2 Simulation of Reversible and Quasi-Reversible Voltammetric Response 62
2.4.3 Numerical Semi-integration 65

3 IDENTIFICATION AND CONTROL OF MICROELECTRODE ARRAY STRUCTURE AT ELECTRODE SURFACES 69

3.1 Effects of Microelectrode Array Structure on Response 69
3.2 Microelectrode Array Structure at TTF-TCNQ Electrodes 73
3.2.1 Scanning Electron Microscopy Imaging of TTF-TCNQ Electrode Surface Structures 73
3.2.2 Evidence of Microelectrode Array Structure in Electrochemical Response at TTF-TCNQ Electrodes . . . 74
3.2.3 Determination of Microelectrode Array Dimensions 80
3.2.4 Verification of Microelectrode Array Structure with Electrochemical Copper Deposition 91
3.3 Microelectrode Array Structure at Graphite Electrodes 94
3.3.1 Evidence for Microelectrode Array Structure at Graphite Electrodes 95
3.3.2 Electrochemical Characterization of Microelectrode Array Structure 96
3.3.3 Characterization of Graphite Surface Structure with Scanning Tunneling and Atomic Force Microscopy 96
3.4 Conclusions 110

4 ROLE OF SURFACE/SUBSTRATE INTERACTIONS IN THE RESPONSE OF ELECTRODES 112

4.1 Theory 112
4.1.1 Multiple Step Electron Transfer Reactions 113
4.1.2 Mediated Electron Transfer Reactions 116
4.1.3 Adsorption at Electrode Surfaces 119
4.2 Surface Chemistry of TTF-TCNQ Electrodes 120
4.2.1 Stability of TTF-TCNQ Electrodes Under Electrochemical Conditions 122
4.2.2 Mechanism of Electron Transfer at TTF-TCNQ Electrodes 129
4.3 Characterization of Weak Surface/Substrate Interactions Which Result in Increased Surface Concentrations 145
4.3.1 Identification and Quantitation of Weak Adsorption with Semi-integral Analysis 147
4.3.2 Weak Adsorption of p-Benzoquinone on Graphite Electrodes . . . 155
4.3.3 Thin-layer Model of Weak Adsorption 158

4.3.4 Semi-integral Analysis in the Presence of Thin-layer Behavior and Diffusion 167
4.4 Conclusions 173

5 SUMMARY AND FUTURE WORK 175

APPENDICES

A ACQUISITION, MANIPULATION, AND SEMI-INTEGRAL ANALYSIS PROGRAM SOURCE CODE 181

B CHRONOAMPEROMETRIC SIMULATION AND OPTIMIZATION PROGRAM SOURCE CODE 213

C CYCLIC VOLTAMMETRIC SIMULATION AND THIN-LAYER MODEL PROGRAM SOURCE CODE 218

REFERENCES 223

BIOGRAPHICAL SKETCH 231

LIST OF TABLES

Table		Page
Table 3.1	Electrochemical response of $Fe(CN)_6^{3-/4-}$ at TTF-TCNQ Electrodes	79
Table 3.2	Calculated values of diffusion layer thickness and dimensionless time for 10 and 119 μm microelectrodes	85
Table 4.1	Predicted transfer coefficients for a consecutive four step (ECEC) electrode reaction with different rate-determining steps	117
Table 4.2	Charge and calculated surface excess of both strong and weakly adsorbed p-benzoquinone on RPG; n=2 and A=0.047$\pm$0.005 cm^2	163

LIST OF FIGURES

Figure — Page

Figure 1.1 Free energy versus reaction coordinate for a single-electron reduction of Ox to Red at potential E. The pathway includes a precursor state, P, a transition state, A, and a successor state, S. $\Delta G^{\ddagger}$ is activation free energy for overall reduction, ΔG° is activation free energy for the elementary electron transfer step, ΔG° is the free energy driving force for the overall reduction, w_p is the work associated with the formation of a precursor state from bulk reactant (Ox) prior to electron transfer, w_s is the work associated with the formation of bulk product (Red) from the successor state following electron transfer 3

Figure 1.2 Schematic of a diffusion layer at a polarized disk electrode with radius r. (a) Growth of a diffusion layer as a function of time ($t_1 < t_2 < t_3 < t_4$) where lines represent a cross section of the interface between the diffusion layer and the bulk solution; and (b) direction of diffusion, represented by arrows, as a function of time, where diffusion perpendicular to the electrode surface is approximated by semi-infinite linear diffusion and diffusion extending out radially is approximated by radial diffusion 9

Figure 1.3 Schematic of an electrode array where dots represent areas of electroactivity separated by inactive regions: (a) distribution of electrodes across inert surface; (b) hexagonal array model; (c) hexagonal array model unit cell which can be approximated by a circular unit cell of equal cross sectional area. Dimensions of circular unit cell are given by r (radius of active area) and R_o (radius of geometric area including active area) 14

Figure 1.4 Schematic of diffusion layer growth at (a) a polarized array of disk electrodes; and (b) at a single unit cell of the array, where r and R_o are the radii of the active and total geometric areas of the unit cell, respectively 16

Figure 1.5 Free energy versus reaction coordinate for a single electron reduction of Ox to Red at potential E. Three different pathways are shown where PAS represents a pathway with energetically favorable precursor and successor states; P'A'S' represents a pathway where the precursor and successor states are further stabilized via surface

interactions although the transition state remains unaffected (weak overlap); and P'A''S' represents a similar pathway with the exception of the transition state which is affected by strong surface interactions (strong overlap). Definitions of $\Delta G^{\ddagger}$, ΔG^{*}, and ΔG^{o} are the same as in Figure 1.1 20

Figure 1.6 Schematic for (a) homogeneous mediated electrocatalysis; (b) heterogeneous mediated electrocatalysis; and (c) unmediated heterogeneous electrocatalysis. A/B represents the redox active mediator 22

Figure 1.7 Schematic of mediated (a) reduction (of Ox to Red) and (b) oxidation (of Red to Ox) where the A/B redox couple acts as a mediator with a formal potential (E^{o}) negative of the Ox/Red couple for a reduction or positive for an oxidation 24

Figure 1.8 Structures of (a) single crystal graphite, where the interplanar distance ($C_o/2$) is 3.354 Å, and (b) glassy carbon where the ribbon diameter and height is ca. 20 and 10 Å, respectively 28

Figure 1.9 (a) Molecular structures of tetrathiafulvalene (TTF) and tetracyanoquinodimethane (TCNQ); and (b) the crystal structure TTF-TCNQ molecular solid which has the form of face to face segregated stacks 31

Figure 2.1 Scanning electron micrographs of (a) unpolished 13:1 TTF-TCNQ/PVC polymer paste electrode surface, 200 X; (b) polished 13:1 TTF-TCNQ/PVC polymer paste electrode surface, 200 X. Bar represents 100 μm 40

Figure 2.1 (continued) (c) high pressure pressed pellet surface 5400 X. Bar represents 1μm 42

Figure 2.2 Scanning electron micrographs of a TTF-TCNQ/PVC spin coated film after copper deposition at -0.1 V versus SCE in 50 mM $CuSO_4 \cdot 5H_2O$: (a) 300 X (Bar = 100 μm); (b) 1000 X (Bar = 10 μm) 45

Figure 2.3 Schematic of (a) quartz crystal microbalance and electrochemical apparatus; and (b) gold electrode patterns deposited on AT cut quartz crystal 52

Figure 2.4 Chronoamperometric simulation and optimization program algorithm. Experimentally determined electrode geometric area, A, n, D, C^{*}, and chronoamperometric response, i(t), are accepted as input 57

Figure 2.5 (a) Microelectrode array model showing uneven distribution of microelectrodes (dots indicate active areas); (b) aggregates of smaller

microelectrodes; (c) approximation of microelectrode aggregates by a single larger microelectrode 60

Figure 2.6 Cyclic voltammetric simulation for thin-layer model program algorithm. Equilibrium constants accepted as input, $K_{eq,Ox}$ and $K_{eq,Red}$, describe concentration equilibrium of Ox and Red between the first and second volume element adjacent to the electrode surface in a finite element representation of diffusion 65

Figure 2.7 Numerical semi-integration program algorithm. Experimental voltammetric data, i(E), and scan rate are accepted as input. Step (2) performs the numerical semi-integration based on equations 2.24 and 2.25 67

Figure 3.1 Zone diagram of cyclic voltammetric characteristics (shown as inlays) as a function of $K\lambda^{1/2}$ and $\Lambda(1-\theta)$, and as a function of experimental parameters (unit cell radius, R_o, standard heterogeneous rate constant, k^o, fraction of active area, $1-\theta$, and scan rate, ν) for disk electrode array 72

Figure 3.2 Experimental (——) and calculated (O) cyclic voltammograms of 5 mM $Fe(CN)_6^{3-/4-}$ in 1.0 M KCl at high-pressure pellet (A, C) and 13:1 unpolished polymer paste (B, D) TTF-TCNQ electrodes. Scan rates were 100 mV-s^{-1} (C,D) and 5000 mV-s^{-1} (A, B) 77

Figure 3.3 (a) Plot of $(\Sigma e_i^2)^{-1}$ versus R_o for unpolished 13:1 TTF-TCNQ/PVC polymer paste electrode after background subtraction, where CA was performed in 2 mM $Fe(CN)_6^{3-/4-}$/1 M KCl and potential was stepped from +0.400 to 0.000 V versus SCE with a pulse width of 1000 ms. (b) Experimental (O) and simulated (solid and dashed lines) chronoamperometric response based on microelectrode dimensions determined from the least-squares optimization program; first iteration r=10, R_o=12 μm (——); second iteration r=119, R_o= 121 μm (- - -) 82

Figure 3.4 Plot of log $i_{p,c}$ versus log ν for 2 mM $Fe(CN)_6^{3-/4-}$/1 M KCl at an unpolished TTF-TCNQ/PVC electrode. Slope of the solid line is 0.5 88

Figure 3.5 Plot of Q versus $t^{1/2}$ for 2 mM $Fe(CN)_6^{3-/4-}$/1 M KCl at an unpolished TTF-TCNQ/PVC electrode. Potential step +0.400 to 0.000 V versus SCE 90

Figure 3.6 Scanning electron micrographs of TTF-TCNQ/PVC electrodes after copper deposition at -0.155 V versus SCE in 50 mM $CuSO_4$, 1000X magnification. (a) unpolished; (b) polished 93

Figure 3.7 Plot of $(\Sigma e_i^2)^{-1}$ versus R_o for (——) untreated GC and (- - -) ECGC electrode after background subtraction. Experimental conditions are the same as those in Figure 3.3 98

Figure 3.8 (a) Constant current STM image (tip bias +100 mV, tunneling current 2 nA) and (b) constant cantilever displacement AFM image (100 μm Si_3N_4 triangular cantilever, spring constant 0.58 N/m) of polished GC in air. XYZ axis in nm 101

Figure 3.9 (a) Constant current STM image (tip bias +100 mV, tunneling current 2 nA) and (b) constant cantilever displacement AFM image (100 μm Si_3N_4 triangular cantilever, spring constant 0.58 N/m) of GC in air following electrochemical treatment in 0.1 M KNO_3. XYZ axis in nm . . 104

Figure 3.10 Constant cantilever displacement AFM image (100 μm Si_3N_4 triangular cantilever, spring constant 0.58 N/m) of GC in air showing typical defect formed as a result of electrochemical treatment in 0.1 M KNO_3. XYZ axis in nm 106

Figure 3.11 Constant cantilever displacement AFM image (100 μm Si_3N_4 triangular cantilever, spring constant 0.58 N/m) GC in air following electrochemical treatment in 0.1 M KNO_3, showing (a) grooves and (b) irregular shaped defects. XYZ axis in nm 108

Figure 4.1 Frequency change as a function of time of a TTF-TCNQ/PVC spin coated electrode in 0.5 M phosphate buffer, pH 7; (a) at open circuit; (b) +0.55; (c) +0.45; (d) +0.25; (e) -0.05; (f) -0.15 V versus Ag/AgCl. The Electrode was held initially at open circuit potential for 60 s to establish frequency stability. Reaction inlays account for observed mass changes 126

Figure 4.2 Frequency change as a function of time of a TTF-TCNQ/PVC spin coated electrode in 0.5 M phosphate buffer, pH 7; (a) 5 $mV\text{-}s^{-1}$; (b) 20 $mV\text{-}s^{-1}$. Bracket signifies one full cycle between 0.000 and +0.450 V versus Ag/AgCl. The Electrode was held initially at open circuit potential for 60 s to establish frequency stability 128

Figure 4.3 Current-potential curves for the reduction of 15 mM $Fe(CN)_6^{3-}$ in 1 M KNO_3, at a rotating disk TTF-TCNQ/PVC electrode as a function of electrode rotation rate. Electrode rotation rates, rpm: (a) 4000; (b) 3000; (c) 2000; (d) 1000; (e) 700; (f) 500; (g) 100. Scan rate 5 $mV\text{-}s^{-1}$ 131

Figure 4.4 Levich plot for data presented in Figure 4.3 at various potentials. Potentials: (a) 0.08; (b) 0.10; (c) 0.12; (d) 0.15; (e) 0.18 V versus SCE 133

Figure 4.5 Koutecky-Levich plot for data presented in Figure 4.3 at various potentials. Potentials: (a) 0.08; (b) 0.10; (c) 0.12; (d) 0.15; (e) 0.18 V versus SCE 135

Figure 4.6 Plot of ln k_f versus E for the reduction of 15 mM $Fe(CN)_6^{3-}$ in 1 M phosphate buffer, pH 7.0, where values of k_f were determined from intercepts in Figure 4.5. 138

Figure 4.7 Plot of ln k_s versus E for the oxidation of 4 mM ascorbic acid (○) and 2 mM catechol (□) in 0.5 M phosphate buffer, pH 7.0 142

Figure 4.8 (a) Plot of (————) (1/4)sech^2(at/2), (·····) $\chi(at)$, and (— — —) (1/4)sech^2(at/2) + $\chi(at)$ versus at; (b) plot of (————) $\chi(at)$, (·····) (1/2) + (1/2)tanh(at/2), and (— — —) $\chi(at)$ + (1/2) + (1/2)tanh(at/2) versus at 152

Figure 4.9 Plot of (————) $\chi(at)$, (·····) (1/2) + (1/2)tanh(at/2), and (— — —) $\chi(at)$ + (1/2) + (1/2)tanh(at/2) versus $(\pi at)^{-1/2}$ 154

Figure 4.10 Cyclic voltammetry of RPG in blank 1 M phosphate buffer solution, pH 7, (— — —) before, and (·····) after cyclic voltammetry of (————) 1 mM p-benzoquinone/1 M phosphate buffer, pH 7, at a scan rate of 1 V-s^{-1} 157

Figure 4.11 (a) Linear sweep voltammogram and (b) semi-integrated linear sweep voltammogram of 1 mM p-benzoquinone/1 M phosphate buffer, pH 7, on RPG following background subtraction, scan rate of 1 V-s^{-1} 160

Figure 4.12 Plot of semi-integrated current from Figure 4.11b versus $(\pi at)^{-1/2}$, where values of at were determined as described in text (eq 4.44) 162

Figure 4.13 Thin-layer model illustrated in a plot of concentration, C, versus distance, x, from the electrode surface, where x=0 represents the electrode surface/thin-layer interface and x=ℓ represents the thin-layer/solution interface. C^* and C^* are the concentrations of the reacting species at t=0 in bulk solution and within the thin-layer, respectively. C*(t) and C(ℓ,t) are the concentrations of the reacting species within the thin-layer and in solution at the surface of thin-layer, respectively, at t>0, where C*(t) and C(ℓ,t) are in equilibrium described by K_{eq} 166

Figure 4.14 Simulated cyclic voltammogram in the presence of the thin-layer model, where Ox is weakly adsorbed ($K_{eq,Ox}$=4) while Red is not adsorbed 169

Figure 4.15 Plot of surface concentrations of (— — —) Ox and (————) Red determined in the first volume element (i.e. within the thin-layer) in the simulation and $C_{Ox}(0,t)$ (Δ) and $C_{Red}(0,t)$ (O) from semi-integrated simulated current, equation 4.61, and equation 4.63. $K_{eq,Ox}$=4 and Red not adsorbed 171

KEY TO SYMBOLS

A	area	cm^2
A_{piezo}	piezoelectrically active area	cm^2
b_j	strength of adsorption, $\beta_j\Gamma_{j,s}$	$mol\text{-}cm^{-2}$
C	capacitance	F
C_j	concentration of species j	$mol\text{-}cm^{-3}$
C_j^*	initial bulk concentration of species j	$mol\text{-}cm^{-3}$
D_j	diffusion coefficient of species j	$cm^2\text{-}s^{-1}$
E	potential of an electrode versus an reference electrode	V
ΔE_p	$\lvert E_{p,a}\text{-}E_{p,c}\rvert$ in CV	V
$E^{o'}$	formal potential of an electrode	V
$E_{p,a}$	anodic peak potential in CV	V
$E_{p,c}$	cathodic peak potential in CV	V
$E_{1/2}$	reversible half wave potential	V
F	faraday; charge of one mole of electrons	C
$f(\tau,\theta)$	normalized current at a unit cell electrode in an array	none
f	F/RT	V^{-1}
f_o	parent frequency	Hz
Δf	shift in resonant frequency	Hz
$\Delta G^{\ddagger}$	activation free energy for overall redox reaction	$J\text{-}mole^{-1}$
ΔG^{*}	activation free energy for elementary electron-transfer step	$J\text{-}mole^{-1}$
ΔG_a	free energy of adsorption	$J\text{-}mole^{-1}$
ΔG^{o}	free energy driving force for the overall redox reaction	$J\text{-}mole^{-1}$
i	current	A
i_D	diffusional component of observed current	A
i_k	kinetic current; current in the absence of mass transfer effects	A
i_l	limiting current	A
i_p	peak current	A
$i_{p,a}$	anodic peak current in CV	A
$i_{p,c}$	cathodic peak current in CV	A
i_m	current at a single unit cell electrode in an array	A
I	semi-integrated current	$C\text{-}s^{-1/2}$
k_{ob}	observed rate coefficient	$M^{-1}\text{-}s^{-1}$; $cm\text{-}s^{-1}$
k_{corr}	work corrected rate coefficient	$M^{-1}\text{-}s^{-1}$; $cm\text{-}s^{-1}$
k^o	standard heterogeneous rate constant	$cm\text{-}s^{-1}$
k_b	heterogeneous rate coefficient for oxidation	$cm\text{-}s^{-1}$
k_f	heterogeneous rate coefficient for reduction	$cm\text{-}s^{-1}$
K_p	equilibrium constant for forming precursor state	M^{-1}; cm
n	electrons per molecule oxidized or reduced; faradays per mole	none
Δm	change in mass	g

Ox	oxidized form of a redox couple	none
Q	total charge passed	C
Q_{ads}	charge due to adsorbed material	C
Q_{dl}	charge due to double-layer capacitance	C
Q_Q	quality factor of quartz crystals	none
R	gas constant (8.31441)	$J\text{-}mol^{-1}\text{-}K^{-1}$
R_o	radius of microelectrode unit cell	cm
Red	reduced form of a redox couple	none
r	radius of active area of an ultramicroelectrode	cm
T	temperature	K
w_p	work associated with the formation of a precursor state from bulk reactant prior to electron transfer	$J\text{-}mol^{-1}$
w_s	work associated with the formation of bulk product from a a successor state following electron transfer	$J\text{-}mol^{-1}$
x	distance from electrode surface	cm
$(1-\alpha)$	anodic transfer coefficient	none
α	cathodic transfer coefficient	none
β	symmetry factor	none
β_j	energy parameter for species j in an adsorption isotherm, $\exp^{-\Delta G_{ad}/RT}$	none
Γ_j	surface excess of species j at equilibrium	$mol\text{-}cm^{-2}$
Γ_j^*	initial surface excess of species j at equilibrium	$mol\text{-}cm^{-2}$
$\Gamma_{j,s}$	surface excess of species j at saturation	$mol\text{-}cm^{-2}$
Γ_n	nuclear tunneling factor	none
δ	diffusion layer thickness	cm
δ_o	convective controlled diffusion layer thickness	cm
δ_{ss}	steady-state diffusion layer thickness	cm
θ	fraction of inactive area	none
θ_j	fractional coverage of an interface by species j	none
κ_{el}	electronic transmission coefficient	none
Λ	dimensionless standard heterogeneous rate constant	none
μ_q	shear modulus of quartz	$N\text{-}cm^{-2}$
ν	scan rate in CV and LSV	$V\text{-}s^{-1}$
ν_n	nuclear frequency factor	s^{-1}
ν_w	kinematic viscosity of water (0.01)	$cm^2\text{-}s^{-1}$
ρ_q	density of quartz	$g\text{-}cm^{-3}$
τ	dimensionless time	none
ψ	dimensionless rate parameter in CV	none
ω	angular frequency of rotation	s^{-1}

Abstract of Dissertation Presented to the Graduate School
of the University of Florida in Partial Fulfillment of the
Requirements for the Degree of Doctor of Philosophy

SURFACE MICROSTRUCTURE AND ITS EFFECT ON ELECTRODE RESPONSE

By

MICHAEL S. FREUND

August 1992

Chairperson: Dr. Anna Brajter-Toth
Major Department: Chemistry

The objective of this work is to determine the effects of surface microstructure on electrochemical response characteristics of the organic conducting salt tetrathiafulvalene-tetracyanoquinodimethane (TTF-TCNQ) and graphite electrodes. Influence of mass transport and surface/substrate interactions on response is determined and a surface structure model is presented.

The effect of surface microstructure on mass transport is investigated at both TTF-TCNQ and graphite electrodes. Surface imaging and electrochemical techniques demonstrate that the surfaces of both materials can be described by a microelectrode array model where localized areas of electrochemical activity are separated by inactive regions. In the case of graphite, atomic force microscopy reveals microelectrode array structure, where surface defects act as localized areas of high electroactivity. Changes in activity resulting from electrode preparation procedures can be accounted for by changes in dimensions of the microelectrode array. The time scale over which the effects of nonlinear diffusion to

individual microelectrodes is observed in transient electrochemical responses is used for determining the dimensions of microelectrode arrays at TTF-TCNQ electrodes. The dimensions of the microelectrode arrays, determined at both TTF-TCNQ and graphite electrodes, are in agreement with dimensions of copper deposits used to image electroactive sites.

The role of surface/substrate interactions in the response of TTF-TCNQ and graphite electrodes is also investigated. Mass changes at TTF-TCNQ electrodes, determined with a quartz crystal microbalance, in addition to kinetic studies, show that a $TCNQ^0$ rich surface is produced under typical electrochemical conditions, and that $TCNQ^0$ mediation is responsible for the catalytic behavior of TTF-TCNQ electrodes toward the oxidation of some biological molecules.

Numerical semi-integration of voltammetric responses is used to identify and quantify weak adsorption in the presence of diffusion. The utility of this method is demonstrated with p-benzoquinone which weakly adsorbs on active graphite electrodes. In addition, a thin-layer model is introduced which is consistent with weak adsorption. This model is used to demonstrate the utility of semi-integral analysis and predicts the behavior of porous thin films into which redox species partition, and predicts the behavior of new surface structure.

CHAPTER 1
INTRODUCTION

1.1 Background

Electrochemists are primarily interested in reactions between species in solution and electrode surfaces where the net reaction results in the transfer of electrons (heterogeneous electron transfer reactions). In the case of a reduction, a general form of the heterogeneous electron transfer reaction can be written as

$$Ox + ne^- \rightleftharpoons Red \tag{1.1}$$

where Ox and Red are the oxidized and reduced forms (i.e. reactant and product) of the species undergoing an n electron reduction. The main difference between a heterogeneous (eq 1.1) and a homogeneous electron transfer reaction, i.e.

$$A^a + B^b \overset{ne^-}{\rightleftharpoons} A^{a-n} + B^{b+n} \tag{1.2}$$

lies in the fact that homogeneous reactions (eq 1.2) involve two reactants in bulk (i.e. A^a and B^b) coming together, whereas heterogeneous reactions involve reactant in solution moving into the proximity of a surface. In both cases, a precursor state is formed, involving A and B in a homogeneous reaction or Ox and the electrode surface in a heterogeneous reaction. This is followed by electron transfer resulting in a successor state and finally the product in bulk solution. These steps are illustrated in Figure 1.1 for a heterogeneous reduction reaction.

Figure 1.1 Free energy versus reaction coordinate for a single-electron reduction of Ox to Red at potential E. The pathway includes a precursor state, P, a transition state, A, and a successor state, S. $\Delta G^{\ddagger}$ is activation free energy for overall reduction, ΔG^{*} is activation free energy for the elementary electron transfer step, ΔG^{o} is the free energy driving force for the overall reduction, w_p is the work associated with the formation of a precursor state from bulk reactant (Ox) prior to electron transfer, w_s is the work associated with the formation of bulk product (Red) from the successor state following electron transfer.

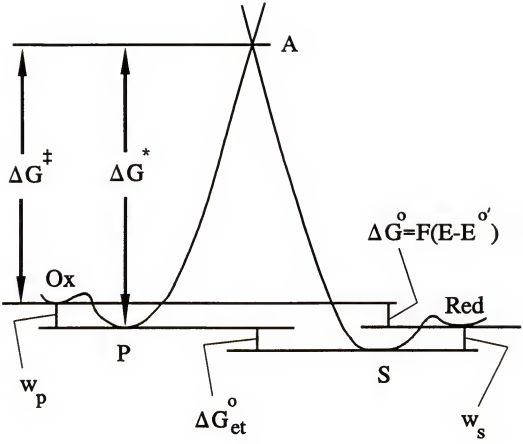
A
$\Delta G^{\ddagger}$
ΔG^{*}
$\Delta G^{o}=F(E-E^{o'})$
Ox
Red
P
S
w_p
ΔG^{o}_{et}
w_s

The observed rate coefficient, k_{ob}, for one-electron transfer redox reactions, either homogeneous or heterogeneous (the heterogeneous rate coefficient is often referred to as the potential dependent rate constant) can be expressed by (Weaver, 1987)

$$k_{ob} = K_p \nu_n \kappa_{el} \Gamma_n \exp\left(\frac{-\Delta G^{\ddagger}}{RT}\right) \tag{1.3}$$

where units of k_{ob} for a heterogeneous reaction are expressed in cm-s^{-1} and for a homogeneous reaction are expressed in M^{-1}-s^{-1}, K_p is the equilibrium constant for forming the precursor state (units in cm for heterogeneous and M^{-1} for a homogeneous reaction), ν_n is the nuclear frequency factor (s^{-1}), κ_{el} is the electronic transmission coefficient or fractional electron-tunneling probability in the transition state, Γ_n is the nuclear tunneling factor, a quantum mechanical correction factor, and $\Delta G^{\ddagger}$ is the activation free energy for the overall reaction (kJ-mol^{-1}). For purposes of comparing homogeneous to heterogeneous electron transfer rate coefficients, a "work corrected" rate coefficient, k_{corr}, is often used, which is the rate coefficient observed in the absence of free energy changes (or work terms) associated with the precursor and successor states (Figure 1.1). This corresponds to the elementary electron transfer and can be expressed as (Weaver, 1987)

$$k_{corr} = K_o \nu_n \kappa_{el} \Gamma_n \exp\left(\frac{-\Delta G^{*}}{RT}\right) \tag{1.4}$$

where K_o describes the probability that the precursor state will form in the absence of the work terms and ΔG^{*} is the activation free energy for the elementary electron transfer step. The work terms referred to above, in the case of a heterogeneous redox reaction, are associated with the movement of charged species through the potential drop at an electrode surface resulting from the electrostatic double-layer. It is possible to relate heterogeneous and homogeneous rate coefficients by the relationship (Weaver, 1987)

$$4\pi N r_h^2 k_{corr}^e \approx k_{corr}^h \tag{1.5}$$

where k_{corr}^e and k_{corr}^h are the corrected rate coefficients for the electrochemical and homogeneous reactions, N is Avogadro's number and r_h is the reactant internuclear distance.

Because the conversion of reactant to product in a heterogeneous redox reaction results in the passing of electrons across the electrode/solution interface (eq 1.1), the rate of the reaction corresponds directly to the rate at which electrons pass through the interface, i.e. the observed current (A or C-s^{-1}). The overall rate, ν_{net} (mol-cm^{-2}-s^{-1}), or observed current, i, of a heterogeneous redox reaction (eq 1.1) can in turn be expressed as

$$\nu_{net} = k_f C_{Ox}(0,t) - k_b C_{Red}(0,t) = \frac{i}{nFA} \tag{1.6}$$

where k_f and k_b are the observed forward (reduction) and reverse (oxidation) rate coefficients (cm-s^{-1}), respectively, $C_{Ox}(0,t)$ and $C_{Red}(0,t)$ are the surface concentrations of Ox and Red (mol-cm^{-3}), respectively, n is the number of electrons transferred per molecule, F is Faraday's constant (96485 C-eq^{-1}), and A is the electrode area (cm^2). By monitoring current one can obtain a direct measure of the overall rate of the electrode reaction.

One of the most powerful aspects of electrochemistry is the ability to alter the rate of a redox reaction by changing the potential at a working electrode. There are several kinetic models which describe the dependence of the rate coefficient on potential (Bockris and Nagy, 1973; Albery, 1975; Bard and Faulkner, 1980; Weaver, 1987). For the scope of this work it will be sufficient to consider the Butler-Volmer model of electrode kinetics described by the equations

$$k_f = k^o \exp^{\frac{-\alpha nF}{RT}(E-E^{o'})} \quad (1.7)$$

$$k_b = k^o \exp^{\frac{(1-\alpha)nF}{RT}(E-E^{o'})} \quad (1.8)$$

where k^o is the standard heterogenous rate constant, α is the transfer coefficient and $E^{o'}$ is the formal potential of the redox reaction. The driving force or the overpotential ($E-E^o$) is related to the standard free energy of the reaction (ΔG^o) as shown in Figure 1.1. For multiple-step processes, values of α will be dependent on the reaction mechanism (Bockris and Nagy,1973) and will be discussed in detail in section 4.1.

When considering equation 1.6, two important factors in the observed rate or current come to mind. These include mass transport (i.e. moving reactant to the surface and product away) which can affect the surface concentrations of both the reactant and the products ($C_{Ox}(0,t)$ and $C_{Red}(0,t)$ in eq 1.6), and surface/substrate interactions which can affect $\Delta G^{\ddagger}$ and ΔG^o, and as a result influence the observed kinetics (eq 1.3) and the thermodynamics (i.e. $\Delta G^o = F(E-E^o)$ as shown in Figure 1.1) of the redox reaction. Another important facet of equation 1.6 is that when the rate of mass transport becomes the rate-determining step in the overall reaction (referred to as diffusion limited) any increase in the rate coefficient for the electron transfer will not affect the observed rate. As a result, an increase in driving force (i.e. over-potential) will not increase the observed rate, and will ultimately limit the efficiency of the reaction.

1.2 Mass Transport at Microelectrode Arrays

Mass transport of reacting species to a polarized electrode, and as a result the efficiency of the reaction under diffusion limited conditions, can be dramatically affected by

surface structure. This is a direct result of the fact that the rate of mass transport changes as a function of time, electrode size, and structure. In order to understand the factors affecting mass transfer it is helpful to introduce two modes of diffusion: radial and semi-infinite linear diffusion.

To visualize these two modes of diffusion, one must first picture the growth of a diffusion layer, or the depletion of reactant at a surface, resulting from a heterogeneous reaction. If the rate of a reaction at a surface is significantly faster that the rate of mass transport to the surface (i.e. diffusion limited conditions), a diffusion layer will begin to grow as a function of time where the diffusion layer thickness, δ (cm), is the distance from the electrode surface over which there is a concentration gradient. The concentration of the reactant ranges from 0, at the surface/solution interface, to bulk concentration (C*), at the diffusion layer/bulk solution interface. Under diffusion limited conditions, δ at any time, t (s), can be described by

$$\delta=(\pi Dt)^{1/2} \tag{1.9}$$

where D is the diffusion coefficient of the diffusing species (cm^2-s^{-1}). Figure 1.2a illustrates the growth of a diffusion layer as a function of time, at a disk electrode. The lines in Figure 1.2 represent the cross section of the diffusion layer at progressively longer times (i.e. $t_1 < t_2 < t_3 < t_4$).

Consider a disk electrode with radius, r, under diffusion limited conditions. When the diffusion layer thickness is significantly smaller than the dimensions of the electrode ($\delta \ll r$) as shown in Figure 1.2a for t_1, the diffusion layer can be approximated by semi-infinite linear diffusion where diffusion is perpendicular to the electrode surface (Figure 1.2b). As the diffusion layer thickness becomes larger than the dimensions of the electrode ($\delta \gg r$) as shown

Figure 1.2 Schematic of a diffusion layer at a polarized disk electrode with radius r. (a) Growth of a diffusion layer as a function of time ($t_1 < t_2 < t_3 < t_4$) where lines represent a cross section of the interface between the diffusion layer and the bulk solution; and (b) direction of diffusion, represented by arrows, as a function of time, where diffusion perpendicular to the electrode surface is approximated by semi-infinite linear diffusion and diffusion extending out radially is approximated by radial diffusion.

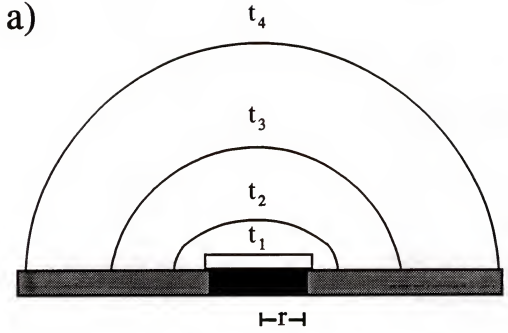
a)
t_4
t_3
t_2
t_1
r

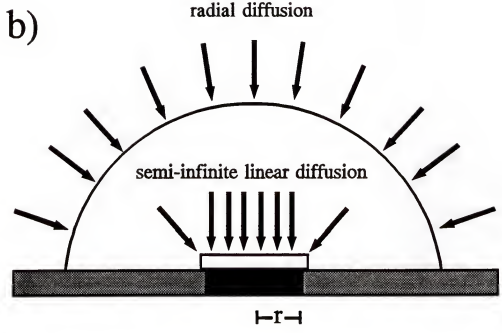
b)
radial diffusion
semi-infinite linear diffusion
r

in Figure 1.2a for t_4, the diffusion layer can be approximated by radial diffusion where the direction of diffusion is no longer perpendicular the electrode surface but instead extends out radially (Figure 1.2b). The time scale over which a diffusion layer will grow from a thickness significantly smaller than the dimensions of the electrode to significantly larger than the dimensions of the disk electrode will depend on D and r. Under typical experimental conditions, r must be on the order of micrometers or less in order to observe both diffusional modes. Electrodes of these dimensions are usually referred to as micro- or ultramicroelectrodes.

The main differences between radial and semi-infinite linear diffusion arise from the geometries of the diffusion layers. In the case of semi-infinite linear diffusion, the surface area of the planar interface between the diffusion layer and the bulk solution remains essentially constant as a function of time (i.e. as the diffusion layer thickness grows) whereas in the case of radial diffusion, the surface area of the hemispherical interface between the diffusion layer and the bulk solution increases as a function of time. For this reason, radial diffusion is inherently more efficient in terms of mass transport than semi-infinite linear diffusion.

It is evident from the discussion thus far that the diffusion profile of a single disk electrode will undergo a transition from semi-infinite linear diffusion to radial diffusion as time progresses, and that the time scale over which the transition occurs will depend on the dimensions of the electrode and the diffusion coefficient. Since these two diffusional modes result in different mass transfer rates, under conditions where a transition between the two diffusional modes occur, the observed rate (or current) will reflect the transition. A rigorous expression for diffusion controlled currents at an embedded disk electrode has been derived and expressed as an asymptotic expansion (Aoki and Osteryoung, 1981; Oldham, 1981),

$$i=4rnFDC^{*}[\frac{\sqrt{\pi}}{2\sqrt{\tau}}+\frac{\pi}{4}-\frac{3\pi\tau}{2^{10}}-\frac{315\pi\tau^{2}}{2^{21}}\ldots] \tag{1.10}$$

where τ is dimensionless time,

$$\tau=\frac{4Dt}{r^{2}} \tag{1.11}$$

Dimensionless time is an important parameter in that it accounts for the interrelationship between the diffusion coefficient, the dimensions of the electrode, and time. Based on equations 1.10 and 1.11 it becomes apparent that when τ is small (i.e. $t\rightarrow 0$ and/or $r\rightarrow\infty$), the first bracketed term dominates the response. If equation 1.11 is substituted into equation 1.10, considering only the first bracketed term, the Cottrell equation is obtained,

$$i=\frac{nFD^{1/2}C^{*}\pi^{1/2}r^{2}}{t^{1/2}} \tag{1.12}$$

corresponding to semi-infinite linear diffusion behavior (Bard and Faulkner, 1980). Under conditions where τ is large (i.e. $t\rightarrow\infty$ or $r\rightarrow 0$), the second bracketed term dominates the response. When equation 1.11 is substituted into equation 1.10, considering only the second bracketed term, a steady-state response is obtained (i.e. independent of time),

$$i=4nFDC^{*}r \tag{1.13}$$

Equation 1.13 is characteristic of radial diffusion or steady-state behavior. The remaining terms in the asymptotic expansion shown in equation 1.10 account for the contribution of edge effects when neither semi-infinite nor radial diffusion modes dominate.

The time required to reach steady-state behavior will depend on the dimensions of the electrode and the diffusion coefficient of the reactant and is defined as (Sleszynski and Osteryoung, 1984)

$$t=\frac{\pi r^2}{16D} \tag{1.14}$$

Considering equations 1.9 and 1.14, the steady-state diffusion layer thickness, δ_{ss}, can be expressed as (Sleszynski and Osteryoung, 1984)

$$\delta_{ss}=\frac{\pi r}{4} \tag{1.15}$$

Microstructure of typical solid electrodes can be described in terms of areas of activity separated by inactive regions, with the two limits of totally active and totally inactive surfaces. This type of surface structure is often referred to as a partially covered or partially blocked electrode (Gueshi et al., 1978; Amatore et al.,1983; Kovach et al., 1986). One of the most straightforward ways to represent such a surface is as an array of evenly spaced disk electrodes embedded in an insulating plane (Gueshi et al., 1978; Reller et al., 1982; Weisshaar and Tallman, 1983; Shoup and Szabo, 1984). Figure 1.3a shows such an array structure where dots represent areas of activity. Gueshi and coworkers proposed a model consisting of a hexagonal array of disk electrodes (Figure 1.3b), where the hexagonal unit cell could be approximated by a circle of equal cross sectional area (Figure 1.3c). The dimensions of the unit cell shown in Figure 1.3c are described by r which represents the radius of the active area and R_o which represents the radius of the geometric area including active and inactive regions. The fraction of inactive area for the unit cell or the entire array, θ, can in turn be expressed by

$$\theta=1-(\frac{r}{R_o})^2 \tag{1.16}$$

Figure1.4 shows the cross section of an array and an individual unit cell, and the effect on mass transport. One can see based on the diffusion profiles shown as solid lines in Figure

Figure 1.3 Schematic of an electrode array where dots represent areas of electroactivity separated by inactive regions: (a) distribution of electrodes across inert surface; (b) hexagonal array model; (c) hexagonal array model unit cell which can be approximated by a circular unit cell of equal cross sectional area. Dimensions of circular unit cell are given by r (radius of active area) and R_o (radius of geometric area including active area).

a)

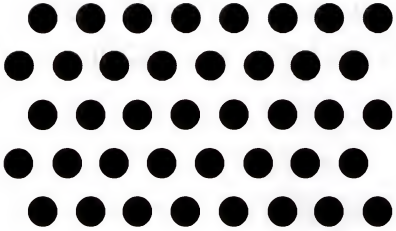

b)

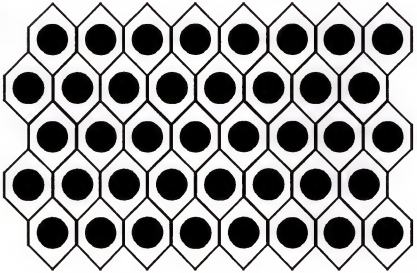

c)

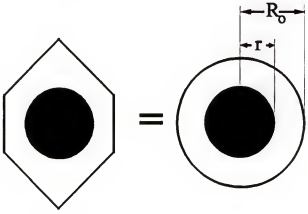

Figure 1.4 Schematic of diffusion layer growth at (a) a polarized array of disk electrodes; and (b) at a single unit cell of the array, where r and R_o are the radii of the active and total geometric areas of the unit cell, respectively.

a)

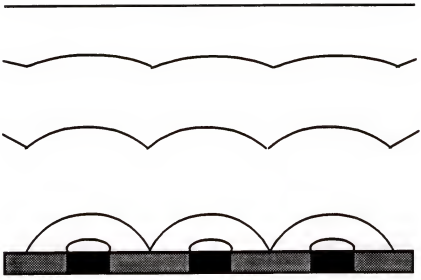

b)

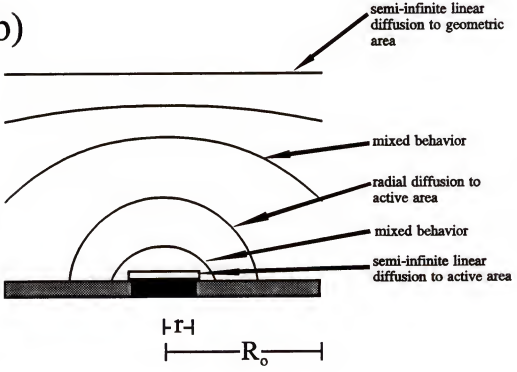
semi-infinite linear diffusion to geometric area
mixed behavior
radial diffusion to active area
mixed behavior
semi-infinite linear diffusion to active area
r
R_o

1.4, that an array structure complicates diffusion to electrode surfaces. At short and intermediate times, the thickness of the diffusion layers is on the order of the dimensions of the microelectrodes, and as a result a transition from semi-infinite linear diffusion to radial diffusion is observed (eqs 1.10-1.13), as for a single disk electrode (Figure 1.2). At sufficiently long times, diffusion layer overlap between adjacent electrodes will result in a diffusional profile which can be approximated by semi-infinite linear diffusion to the entire geometric area of the array as shown by the single, horizontal, solid line in Figure 1.4a.

It is clear from the discussion that surface microstructure can affect electrode response. The ability to control surface microstructure can be used to produce analytically useful electrode surfaces. For example, under conditions where a response is controlled by semi-infinite linear diffusion to the geometric area of the microelectrode array, the electrode response will be proportional to the electrode geometric area, regardless of the fraction of active area. Since the charging current or background is proportional to the active area, an increase in S/N can be achieved by decreasing the fraction of active area, which will reduce background without reducing the magnitude of the response.

Although there are advantages in reducing the fraction of active area at an electrode surface, there are other factors which must be considered. For example, the theory, which will be introduced in detail in section 3.1, demonstrates that the fraction of the active area also controls the apparent heterogeneous rate constant, which decreases with decreasing active area. In practice, this means that if an electrode reaction is slow, decreasing the fraction of active area will result in a response which appears less reversible (i.e. peaks which are smaller and more spread out), offsetting any advantage gained by reducing the background. On the other hand, if the electrode reaction is sufficiently fast, changes in the fraction of active area over a limited range may not affect apparent reversibility, resulting in a net S/N

increase. Because of the importance of controlling electrode surface structure there is considerable interest in developing methods for fabricating and manipulating microelectrode structures (Sleszynski and Osteryoung, 1984; Freund and Brajter-Toth, 1989; Strohben et al., 1990; Freund and Brajter-Toth, 1991).

1.3 Mediation and Adsorption at Electrode Surfaces

Electrocatalysis is of interest in many areas of science including energy conversion, synthesis, and analysis. The role of electrocatalysts is to promote electrode reactions without being consumed, and as a result they are utilized to minimize the driving force (i.e. reduce ΔG°) and/or to increase the rate for the reaction (i.e. reduce $\Delta G^{\ddagger}$) (see Figure 1.5) thereby increasing reaction selectivity and efficiency. Electrocatalysis can occur either through a heterogeneous or a homogeneous mechanism involving interactions of the reacting species with the surface or by electron transfer to intermediate species in solution or on the surface (mediation) as illustrated in Figure 1.6. In the case of homogeneous catalysis or mediation (Andrieux et al.,1979; Andrieux et al.,1990) a redox couple (represented by the A/B couple in Figure 1.6) is chosen which is electrochemically fast (small $\Delta G^{\ddagger}$). To mediate a reduction reaction (Figure 1.7a), a formal potential of a catalyst positive of Ox is chosen. The opposite is the case for oxidations as shown in Figure 1.7b.

Heterogeneous catalysis, on the other hand, can involve interaction between the Ox/Red couple and the electrode surface. As illustrated in Figure 1.5, the free energy of the precursor (P), the successor (S), and the transition state (A) can be affected by their interactions with the electrode surface. These interactions can be divided into two classifications, weak and strong overlap electron transfer reactions (Weaver, 1987). Weak

Figure 1.5 Free energy versus reaction coordinate for a single electron reduction of Ox to Red at potential E. Three different pathways are shown where PAS represents a pathway with energetically favorable precursor and successor states; P'A'S' represents a pathway where the precursor and successor states are further stabilized via surface interactions although the transition state remains unaffected (weak overlap); and P'A''S' represents a similar pathway with the exception of the transition state which is affected by strong surface interactions (strong overlap). Definitions of $\Delta G^{\ddagger}$, ΔG^{*}, and ΔG^{o} are the same as in Figure 1.1.

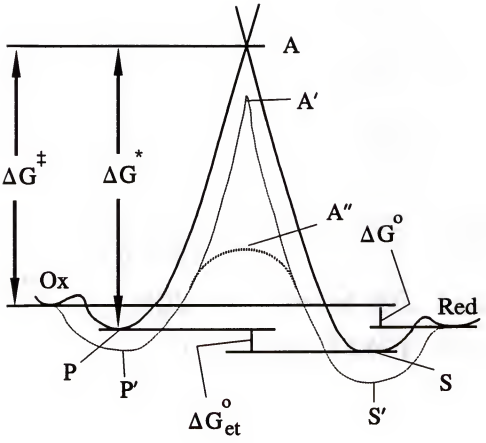
A
A′
A″
ΔG‡
ΔG*
ΔG°
Ox
Red
P
P′
S
S′
ΔG°et

Figure 1.6 Schematic for (a) homogeneous mediated electrocatalysis; (b) heterogeneous mediated electrocatalysis; and (c) unmediated heterogeneous electrocatalysis. A/B represents the redox active mediator.

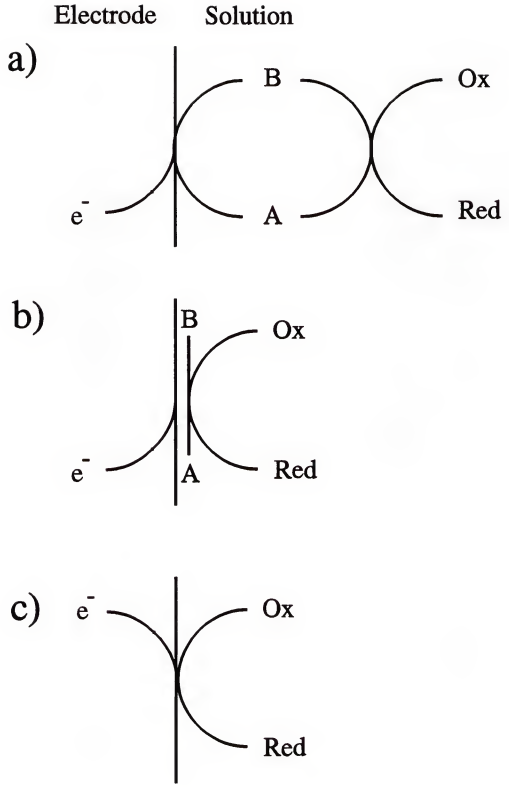
Electrode
Solution
a)
B
Ox
e⁻
A
Red
b)
B
Ox
e⁻
A
Red
c)
e⁻
Ox
Red

Figure 1.7 Schematic of mediated (a) reduction (of Ox to Red) and (b) oxidation (of Red to Ox) where the A/B redox couple acts as a mediator with a formal potential ($E^{o'}$) negative of the Ox/Red couple for a reduction or positive for an oxidation.

a)

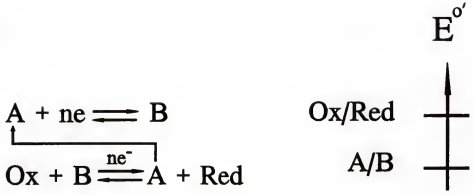

b)

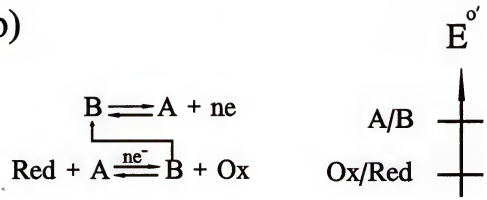

overlap interactions between the reacting species and the electrode surface are weak and nonspecific and as a result do not affect the activation free energy for the fundamental electron transfer step (ΔG^*) (P'A'S' in Figure 1.5). Therefore, the activation free energy is controlled by the properties of the isolated reactant. Strong overlap, on the other hand, involves strong enough interactions between the reacting species and the electrode surface so as to affect the activation free energy (P'A"S' in Figure 1.5).

Adsorption can also alter the kinetics and/or the thermodynamics of the redox reaction by changing the relative free energies of the reactant, product, and/or the transition state relative to those in bulk solution. Adsorption of species from solution results in the formation of a partial or complete layer on the surface. The resulting surface coverage (or surface excess, Γ (mol-cm^{-2})) as a function of concentration can be described by an adsorption isotherm (Laviron, 1982; Parsons, 1990). Since the kinetics and/or thermodynamics of the adsorbed species may be different from those of species in solution, adsorption can complicate responses observed in the presence of nonadsorbed species. Adsorption is often referred to as strong or weak adsorption (Wopschall and Shain, 1967), which is different from strong or weak overlap discussed above. Instead, the strength of adsorption is related to the free energy of adsorption, ΔG_a (i.e. the difference in free energy between the adsorbed species and the species in solution), and the concentration of adsorbing species in solution. Adsorption will be discussed in more detail in sections 4.1.3 and 4.3.

1.4 Structural and Chemical Properties of Graphite

Graphite has attracted attention as an electrode material for numerous reasons including: high conductivity, availability, low cost, low chemical reactivity, and relatively wide stable potential window (Kinoshita, 1988). The forms of graphite most widely used as

electrode materials include pyrolytic graphite and glassy (or vitreous) carbon (Dryhurst and McAllister, 1984). Pyrolytic graphite consists of conjugated hexagonal rings of carbon atoms (C-C bond length of 1.42 Å) arranged in planes as shown in Figure 1.8a (Kinoshita, 1988). These planes are held together in ABAB... stacks by weak van der Waals forces. The stacks are separated by 3.354 Å. The conductivity along the planes (edge plane) is metallic (10^{-2} Ω^{-1}-cm^{-1}), whereas conductivities perpendicular to the planes (basal plane) are 2 orders of magnitude lower, i.e. semiconducting (Kinoshita, 1988).

Glassy or vitreous carbon (Cowlard and Lewis, 1967), on the other hand, is an amorphous material consisting of interlocking, randomly oriented, ribbons (see Figure 1.8b). The interlocking ribbons increase tensile strength and resistivity (10-50 Ω-cm) (Kinoshita, 1988). The individual ribbons (or crystallites) have a layered structure similar to the structure of pyrolytic graphite, with ribbon diameter and height of ca. 20 and 10 Å, respectively (Jenkins and Kawamura, 1971; McCreery, 1991).

Numerous methods have been proposed to improve electrochemical reversibility, sensitivity, and reproducibility of graphite electrodes including electrochemical treatment (Engstrom, 1982; Engstrom and Strasser, 1984; Wightman et al., 1984; Hu et al., 1985; Cabaniss et al., 1985; Nagaoka and Yoshino, 1986a; Nagaoka and Yoshino, 1986b; Wang and Tuzhi, 1986; Kovach et al., 1986; Wang and Lin, 1988; Kepley and Bard, 1988; Nagaoka et al., 1988; Gewirth and Bard, 1988; Bowling et al., 1989a; Bodalbhai and Brajter-Toth, 1990; Wang et al., 1990; Smyrl et al., 1989), laser irradiation (Poon and McCreery, 1986; Poon and McCreery, 1988; Bowling et al., 1989b; Sternitzke and McCreery, 1990), rf plasma (Evans and Kuwana, 1977) and heat treatment (Stutts et al., 1983; Kazee et al., 1985; Fagan et al., 1985; Hu et al., 1986). Electrochemical treatment and laser irradiation are particularly attractive because they are relatively inexpensive, quick, and can be performed

Figure 1.8 Structures of (a) single crystal graphite, where the interplanar distance ($C_o/2$) is 3.354 Å, and (b) glassy carbon where the ribbon diameter and height is ca. 20 and 10 Å, respectively.

a)

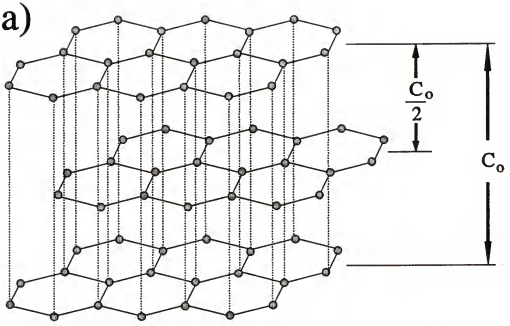

b)

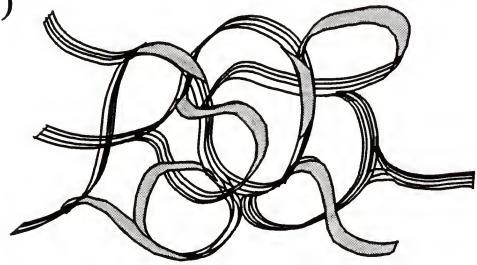

without removing the electrode from solution. The majority of the methods have been developed empirically and only recently has an understanding of parameters controlling surface activity begun to emerge (Bowling et al., 1989b; Chang and Bard, 1990). Activation, common to these procedures, may be increased due to exposed edge plane density (Bowling et al., 1989a; Bowling et al., 1989b; McCreery, 1991) which has been associated with faster kinetics (Wightman et al., 1984). For example, the standard heterogeneous rate coefficient for $Fe(CN)_6^{3-/4-}$ is reported to be 4 orders of magnitude faster at the exposed edge plane of highly oriented pyrolytic graphite than the basal plane (Bowling et al., 1989b).

1.5 Structural and Chemical Properties of Tetrathiafulvalene-Tetracyanoquinodimethane (TTF-TCNQ)

There has been great interest in molecular materials (Ward, 1989) with the discovery of tetrathiafulvalene-tetracyanoquinodimethane (TTF-TCNQ) (Ferraris et al., 1973). Perhaps the most attractive features of these materials are their electronic properties which can be altered by modifying the properties of the molecular components. This ability to alter the electronic properties through rational modification has lead to the discovery of organic superconductors (Bechgaard and Jerome, 1982; Williams et al.,1985).

The structure of the TTF-TCNQ molecular crystal is shown in Figure 1.9 where TTF and TCNQ form face to face segregated stacks due to intermolecular π-π interactions (Ward, 1989). Each component possesses an average nonintegral charge ($TTF^{0.59+}$-$TCNQ^{0.59-}$). Intermolecular π orbital overlap and the resulting delocalization of charge results in metallic conductivity. The segregated stack structure is the source of the quasi-one-dimensional nature of TTF-TCNQ (i.e. metallic conductivity along the stacks, semiconducting across).

TTF-TCNQ was first used as an electrode material by Jaeger and Bard (Jaeger and Bard, 1979; Jaeger and Bard, 1980). The stable potential window for TTF-TCNQ in aqueous

Figure 1.9 (a) Molecular structures of tetrathiafulvalene (TTF) and tetracyanoquinodimethane (TCNQ); and (b) the crystal structure TTF-TCNQ molecular solid which has the form of face to face segregated stacks.

a)

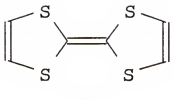

TTF

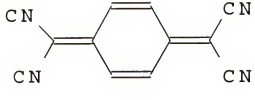

TCNQ

b)

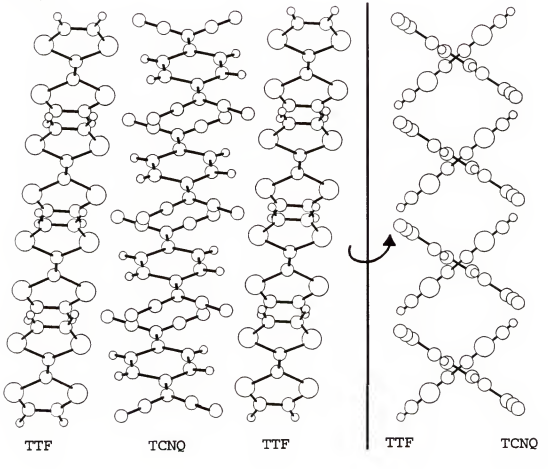

solutions was reported to be between ca. +500 mV and -200 mV versus SCE, and depends on the supporting electrolyte. At potentials outside this window, lattice oxidation or lattice reduction occur. Within the stable window, the electrode demonstrated reversible behavior for $Fe(CN)_6^{3-/4}$, similar to the behavior observed on Pt electrodes (Jaeger and Bard, 1979).

More recent reports have shown that TTF-TCNQ can be used as an electrode material for the electrocatalytic oxidation of β-NADH (Albery and Bartlett, 1984) and flavoenzymes (McKenna and Brajter-Toth, 1987; Albery et al., 1985; Cenas and Kulys, 1981; Albery et al., 1986; Albery et al., 1987a; Kulys et al., 1981; Hale and Wightman, 1988; Hill et al., 1988). Although the properties of this electrode material have been investigated actively, the mechanism of electrocatalysis is not clear (Albery et al., 1985; Albery et al., 1987a; Jaeger and Bard, 1979; McKenna et al., 1988). A mechanism involving homogeneous mediation by small amounts of dissolved electrode material have been proposed, where TTF^+ or $TCNQ^-$ mediate electron transfer (Cenas and Kulys, 1981; Albery et al., 1987a; Hale and Slotheim, 1989). Heterogeneous mediation has also been proposed, where electron transfer occurs via surface bound TCNQ° produced by dissociation of TTF-TCNQ on the electrode surface (Albery et al., 1987b).

1.6 Scope of the Dissertation

The objective of this dissertation is to evaluate the effect of surface microstructre on the electrochemical response of the quasi-one-dimensional organic conducting salt, TTF-TCNQ, and graphite electrodes. The hypothesis tested is that a microelectrode array model is general and can explain the activity of exotic surfaces such as TTF-TCNQ as well as commonly used surfaces such as graphite. An additional objective of this work is to investigate the role of surface/substrate interactions in increasing electrode activity at TTF-

TCNQ and graphite electrodes. The role of surface chemistry and adsorption is explored experimentally and theoretically as a means to explain increased electrode activity. Based on the results of this study, a surface structure model is introduced.

Background related to this research is discussed in Chapter 1, including theory covering electron transfer kinetics, mass transport at surfaces, and mediation. Chapter 2 deals with the experimental approaches used in this work including materials, methods, apparatus, and experimental techniques. Finally, numerical techniques, used to simulate voltammetric responses and to evaluate experimental results, are described.

The objective of Chapter 3 is to evaluate the structure reactivity relationship at TTF-TCNQ and graphite electrodes. After a description of the effects of microstructure on mass transport, and predicted responses as a function of microstructure dimensions, TTF-TCNQ and graphite electrode surface structures are characterized. Surface imaging and electrochemical techniques are used to establish the surface structures of both materials in terms of electroactivity, and a correlation between surface structure and activity is demonstrated.

In Chapter 4, the role of surface/substrate interactions in the response of TTF-TCNQ and graphite electrodes is investigated. This chapter begins with kinetic theory pertaining to multiple-step redox reactions followed by results characterizing factors affecting response at TTF-TCNQ and graphite electrodes. The role of surface chemistry in the electrocatalytic behavior of TTF-TCNQ electrodes is investigated with a combination of surface characterization techniques and kinetic measurements.

Following a discussion of TTF-TCNQ surface chemistry and the mechanism of electrocatalysis, the role of surface/substrate interactions, specifically weak adsorption, on electrode response is investigated. The ability of numerical semi-integration to separate the

contributions of diffusion and adsorption in a response characteristic of weak adsorption is demonstrated in theory, and the utility of the semi-integral analysis method for the identification and quantitation of weak adsorption is then demonstrated in experimental studies.

Chapter 4 concludes with the introduction of a surface structure model (thin-layer model) which is consistent with weak adsorption, and represents a new, analytically useful, electrode surface structure. In addition to predicting the behavior of thin porous films into which redox species can diffuse and adsorb, the thin-layer model is used to demonstrate the utility of semi-integral analysis to determine concentrations within a film. Finally, Chapter 5 summarizes the results of this work and discusses the direction of future research.

CHAPTER 2
EXPERIMENTAL

2.1 Materials

All chemicals were reagent grade and were used as received. Potassium ferricyanide was obtained from Mallinckrodt. Ascorbic acid was obtained from Chem Service. Tetrathiafulvalene (TTF), 7,7,8,8-tetracyanoquinodimethane (TCNQ), poly(vinyl chloride) (PVC), and catechol were obtained from Sigma. Concentrated sulfuric acid, potassium chloride, p-benzoquinone, and tetrahydrofuran (THF) were obtained from Fisher. Sodium phosphate monobasic, dibasic, $CuSO_4 \cdot 5H_2O$, and potassium nitrate were obtained from Baker.

All solutions were made with deionized/distilled water and were deoxygenated by bubbling N_2 through solutions for at least 5 minutes prior to electrochemical experiments. Solutions containing ascorbic acid, catechol, and p-benzoquinone were prepared fresh daily, and care was taken to protect these solutions from exposure to light. All measurements were made at room temperature.

2.2 Electrochemical Apparatus

Electrochemical measurements were carried out with a Bioanalytical Systems electrochemical analyzer, BAS-100®, which was interfaced to an IBM® compatible PC for data storage and manipulation, unless otherwise stated. In experiments performed with the BAS-100®, solution resistance was compensated with the BAS-100®. Electrodes used in

electrochemical experiments included saturated calomel (SCE) and Ag/AgCl reference electrodes and a 1 cm^2 platinum foil auxiliary electrode. Potentials are reported versus SCE unless otherwise specified.

2.3 Experimental Procedures

2.3.1 Electrode Preparation

2.3.1.1 Platinum

Platinum (Pt) working electrodes consisted of a platinum wire (ca. 2 mm diameter) sealed in glass. These electrodes were polished to a mirrorlike finish on an Alpha A* cloth (Mark V Laboratory) with grade B gamma alumina (particle size < 0.1 μm) obtained from Fisher using metallographic polishing wheel (Buehler Ecomet I polisher-grinder). The Pt electrodes were then ultasonicated for 5 minutes, exposed to concentrated H_2SO_4 for 5 minutes, and finally rinsed with copious amounts of deionized/distilled water. The cleanliness of the Pt electrode was verified with cyclic voltammetry in 0.5 M H_2SO_4 at 1 $V\text{-}s^{-1}$. Observation of well defined cathodic peaks corresponding to the adsorption of hydrogen and the reduction of platinum oxide; and anodic peaks corresponding to the oxidation of adsorbed hydrogen and the formation of platinum oxide was indicative of a clean Pt electrode (Bard and Faulkner, 1980).

2.3.1.2 Rough pyrolytic graphite

Rough pyrolytic graphite (RPG) electrodes (Dryhurst, 1984; Bodalbhai and Brajter-Toth, 1990) consisted of pyrolytic graphite (Pfizer) sealed with Epoxy-Patch* epoxy (Dexter corporation) in glass. Electrical contact between the pyrolytic graphite and the copper lead was achieved through a mercury drop. Pyrolytic graphite electrodes were resurfaced with

600-grit silicon carbide (SiC) paper (Mark V Laboratory) on a polishing wheel. After resurfacing, pyrolytic graphite electrodes were rinsed with deionized/distilled water.

2.3.1.3 Glassy carbon

Glassy carbon (GC) electrodes consisted of a 2 mm length of 3 mm diameter GC-10 glassy carbon rod (Electrosynthesis) sealed in epoxy. Electrical contact between the glassy carbon and the copper lead was achieved through a drop of mercury. These electrodes were polished on Alpha A® cloth with grade B gamma alumina (particle size < 0.1 μm, Fisher) using a polishing wheel, and ultrasonicated for 5 minutes. GC prepared by this method is referred to as untreated GC.

Glassy carbon electrodes used in STM/AFM experiments were resurfaced with 5, 0.3 and finally 0.05 μm alumina on separate microcloths using a polishing wheel. The electrodes were finally ultrasonicated for 5 minutes in distilled water. Electrochemical treatment for these experiments was achieved by poising a polished GC electrode at +1.8 V versus Ag/AgCl for 5 minutes followed by -0.1 V versus Ag/AgCl for 2 minutes in 0.1 M supporting electrolyte (Engstrom et al., 1984). Electrochemically treated GC electrodes were rinsed with copious amounts of distilled water and were allowed to dry under ambient conditions for 24 hours.

2.3.1.4 TTF-TCNQ

TTF-TCNQ salt (Ferraris et al., 1973) was prepared by refluxing TTF and TCNQ separately in equimolar quantities in acetonitrile (Jaeger and Bard, 1979). After 30 minutes of refluxing, the hot solutions were mixed, resulting in the immediate formation of a black precipitate. The combined solutions were protected from light and allowed to cool. The precipitate was filtered and washed 5 times with cold acetonitrile and 5 times with cold diethyl ether to remove any traces of neutral materials. The precipitate was then dried for 24 hours

under vacuum while care was taken to protect it from light. The resulting salt was stored in a freezer until it was used.

The TTF-TCNQ/PVC polymer paste electrodes were constructed by using the procedure described by McKenna and coworkers (McKenna et al., 1988). First, the polymer, PVC, was thoroughly dissolved in THF after which TTF-TCNQ complex was added to make a TTF-TCNQ/PVC mixture of 13:1 (w/w). Care was taken to ensure that all PVC was dissolved before the salt was added, and care was also taken to maintain a uniform suspension by stirring constantly until the paste had thickened. The paste was then spread into platinum-lined Teflon® holders (Albery et al., 1985; McKenna et al., 1988). Teflon® holders were 6 mm in diameter and 1 mm thick. The electrodes were allowed to dry for 24 hours before use. The resistance of these electrodes was ca. 100 Ω. Figure 2.1a shows a scanning electron micrograph (SEM) of an unpolished 13:1 TTF-TCNQ/PVC electrode produced by this method.

The geometric areas of several unpolished 13:1 TTF-TCNQ/PVC polymer paste electrodes were determined by chronocoulometry using 1.0 mM $K_3Fe(CN)_6$ in 1 M KCl. The potential was stepped from 0.400 to 0.100 V with a pulse width of 250 msec. The resulting slopes of the plots of charge versus the square root of time for three electrodes prepared in an identical fashion were 3.04, 2.44 and 2.94 $\mu C/msec^{1/2}$, with correlation coefficients no less than 0.9990. The resulting areas which were calculated using $D_{ox} = 7.63 \times 10^{-6}$ cm^2/s (Gerhardt and Adams, 1982) yielded an average value of 0.292 ± 0.036 cm^2. Polished TTF-TCNQ/PVC polymer paste electrodes, as shown in Figure 2.1b, were prepared by lightly polishing with a Kimwipe®.

High-pressure pellet electrodes (Jaeger and Bard, 1979) were prepared with a hydraulic press producing a pressure of ca. 3000 psi. The TTF-TCNQ powder was pressed

Figure 2.1 Scanning electron micrographs of (a) unpolished 13:1 TTF-TCNQ/PVC polymer paste electrode surface, 200 X; (b) polished 13:1 TTF-TCNQ/PVC polymer paste electrode surface, 200 X. Bar represents 100 μm.

a)

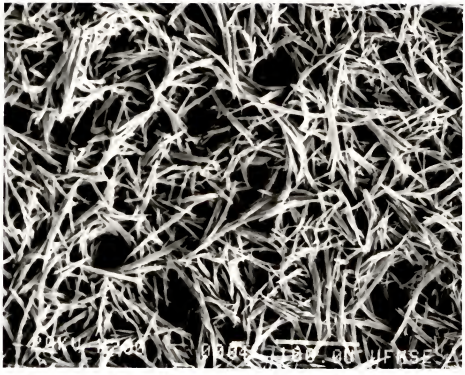

b)

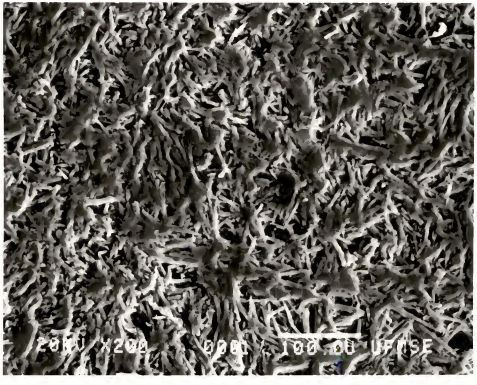

Figure 2.1 (continued) (c) high pressure pressed pellet surface 5400 X. Bar represents 1 μm.

c)

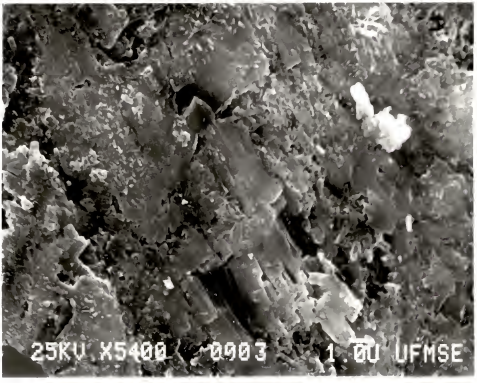

into disks of ca. 2 mm thickness. The electrical contact was made by attaching a piece of copper wire to the pellet with nickel paint (GC Electronics, Rockford, IL). The resistance of the pellet electrodes was ca. 50 Ω. Figure 2.1c shows an SEM of the surface of a pressed pellet electrode. Typical electrode areas determined by chronocoulometry (pulse width of 250 ms) were 0.195 $\pm$ 0.001 cm^2.

Spin coated TTF-TCNQ/PVC electrodes were used in quartz crystal microbalance experiments. Spin coated TTF-TCNQ/PVC electrodes were prepared with a 3:10:200 of TTF-TCNQ/PVC/THF (w/w/w) solution. The solutions were made by first dissolving the PVC in THF, after which the TTF-TCNQ was added. Higher concentrations of TTF-TCNQ led to instability in the crystal response, whereas smaller amounts led to films with decreased electrical conductivity. Frequency instability exhibited by crystals with high concentrations of TTF-TCNQ in the coating was attributed to a deterioration of the quality factor of the quartz crystal, which is known to be dependent on preparation procedures. The solution/suspension was kept cool (in ice) and used immediately.

Spin coating was accomplished on the quartz crystals at 1700 RPM for 20 seconds at room temperature. The crystal was then placed under vacuum (10^{-3} Torr) for 15 minutes to remove excess solvent. The electrochemically active area, A_{elec}, was determined by chronocoulometry using a 4.0 mM $K_3Fe(CN)_6$ solution in 0.1 M KCl (D_{ox} = 7.63 X 10^{-6} cm^2/s) to be 0.35 cm^2. The piezoelectrically active area, A_{piezo}, was determined geometrically with calipers. The area was also determined by comparison of the frequency response associated with electrochemical deposition and stripping of copper with the amount of charge passed. Assuming rigid layer behavior, the area determined, 0.18 cm^2, agreed to within 1% with that measured geometrically.

Figure 2.2 Scanning electron micrographs of a TTF-TCNQ/PVC spin coated film after copper deposition at -0.1 V versus SCE in 50 mM $CuSO_4 \cdot 5H_2O$: (a) 300 X (Bar = 100 μm); (b) 1000 X (Bar = 10 μm).

a)

b)

Scanning electron microscopy was used to verify that the resulting spin coated electrodes had an even distribution of TTF-TCNQ crystals in a uniform PVC film (Figure 2.2). TTF-TCNQ and PVC could be distinguished visually. The electroactive sites on these electrodes were identified by electrodepositing copper. SEM micrographs indicated the presence of dispersed spherical copper deposits with an estimated site density of 10^5 sites/cm^2 (Figure 2.2). The average projected area of the Cu^0 deposits was 1 X 10^{-6} cm^2. This data suggests that the fraction of electroactive area (1-θ) (Amatore et al., 1983) is 0.1. Figure 2.2 suggests that the spin coated electrodes can be described as a random microelectrode array, similar to the characterization reported for the 13:1 TTF-TCNQ/PVC electrodes (Freund and Brajter-Toth, 1989).

2.3.2 Electrochemical Techniques

2.3.2.1 Cyclic and linear sweep voltammetry

Cyclic and linear sweep voltammetry (CV and LSV) were performed to: (i) identify adsorption; (ii) determine kinetic information; and (iii) determine mechanistic information. CV and LSV involve ramping of potential at a working electrode in the presence of redox active species in solution (Nicholson and Shain, 1964). In CV and LSV experiments the potential is scanned from an initial value where no reaction occurs to a value where the reaction rate is limited by diffusion. In CV only, the potential is then ramped back to the initial potential. The time scale of the experiment is expressed as scan rate, ν (V-s^{-1}), and is the rate at which the potential is ramped.

CV or LSV can be used to identify the presence of adsorption. Identification may be achieved using log-log plots of peak current versus scan rate (log i_p versus log ν) (Bard and Faulkner, 1980). In the case of weak adsorption, the slope of a plot of log i_p versus log ν will lie somewhere between a value 0.5 and 1.0, where a slope of 0.5 is characteristic of a

purely diffusion controlled response, and a slope of 1.0 is characteristic of a purely adsorption controlled response (Bard and Faulkner, 1980). Identification of weak adsorption may also be achieved via semi-integration of CV (Bowling and McCreery, 1988). The appearance of a peak on top of the typically sigmoidal semi-integrated voltammetric response for a diffusion controlled reaction indicates weak adsorption.

Kinetic information may also be determined from CV data using the method of Nicholson (Nicholson, 1965). The standard heterogeneous rate constant, k°, can be calculated from

$$k^{\circ}=\psi(\pi a D_{Red})^{1/2}(D_{Red}/D_{Ox})^{\alpha/2} \qquad (2.1)$$

where $a = nF\nu/RT$. Values of ψ used in calculations were determined from separation of anodic and cathodic peak potentials, ΔE_p, and have been published (Nicholson, 1965). In calculations using equation 2.1 it was assumed that $D_{Ox} = D_{Red}$.

2.3.2.2 Rotating disk electrode

Rotating disk electrode measurements were carried out using the BAS-100 with an IBM® Model EC/219 Rotating Disc Electrode Controller and a Model EC/219 rotator. Rotating disk electrode experiments (RDE) were performed to obtain kinetic and mechanistic information. The inverse of the limiting current obtained from LSV in RDE measurements, i_l^{-1}, contains kinetic and diffusion current components (Bard and Faulkner, 1980),

$$i_l^{-1}=i_k^{-1}+i_D^{-1} \qquad (2.2)$$

In equation 2.2, only i_D depends on the angular frequency of rotation, ω, (s^{-1}), where

$$i_D=0.620nFAC^{*}D^{2/3}\nu_w^{-1/6}\omega^{1/2} \qquad (2.3)$$

and ν_w is the kinematic viscosity of water (0.01 cm^2-s^{-1}). At the limit $\omega\rightarrow\infty$, $i_l^{-1} = i_k^{-1}$ where, for a reduction

$$i_k = nFAk_f C^*_{Ox} \tag{2.4}$$

and for an oxidation

$$i_k = nFAk_b C^*_{Red} \tag{2.5}$$

i_k is the kinetic current in the absence of mass transfer effects and k_f and k_b are apparent heterogenous rate coefficients for a reduction and oxidation, respectively, as defined in equations 1.7 and 1.8. Mechanistic information is obtained by the dependence of apparent heterogeneous rate coefficient on potential and is described in detail in section 4.1.

2.3.2.3 Chronocoulometry and chronoamperometry

Chronocoulometric (CC) and chronoamperometric (CA) experiments involve stepping the potential of a working electrode. The instantaneous step is from a potential value where the rate of the redox reaction of interest is negligible to a potential value where the rate is diffusion limited. Typical values of pulse width range from 100 to 1000 ms. The transient response, charge in the case of CC and current in the case of CA, is then monitored as a function of time. In the case of CA under semi-infinite linear diffusion conditions, the transient response, i(t), is described by the Cottrell equation,

$$i(t) = \frac{nFAD^{1/2}C^*}{\pi^{1/2}t^{1/2}} \tag{2.6}$$

while for CC, the transient response, Q(t), is described by the integrated Cottrell equation,

$$Q(t) = \frac{2nFAD^{1/2}C^*t^{1/2}}{\pi^{1/2}} \tag{2.7}$$

CA experiments were performed with a Princeton Applied Research (PAR) model 173 potentiostat with a model 175 universal programmer and a Bausch & Lomb Omnigraphic 2000 X-Y recorder. Due to the response time limitations of the X-Y recorder, data from CA

experiments were collected 100 ms after application of the potential step in increments of 100 ms. CC experiments were performed on a BAS-100® where data were collected 1 ms after application of the potential step in increments of 1 ms.

In this work, CC was used for a number of purposes including: (i) to determine electrode area; (ii) to determine diffusion coefficients; and (iii) to quantitate adsorption. Electrode area and diffusion coefficient were determined from the slopes of CC plots of Q versus $t^{1/2}$ (eq 2.7). For the purpose of quantitating adsorption, one can take advantage of the fact that in CC the contribution from the redox reaction of the adsorbed material to measured charge is independent of time (on the time scale of a typical CC experiment) whereas the contribution of species diffusing to the surface has a square root dependance on time (eq 2.7). As a result, the charge due to adsorbed material can be determined from the intercept of Q versus $t^{1/2}$ plot where the intercept, Q, contains two components due to double layer charging, Q_{dl}, and adsorption, Q_{ads},

$$Q=Q_{dl}+Q_{ads} \tag{2.8}$$

and where Q_{ads}, is related to the amount of adsorbed material (surface excess, Γ^*, mol-cm^{-2}) by

$$Q_{ads}=nFA\Gamma^* \tag{2.9}$$

The transient response obtained from CA was used in this work to characterize the dimensions of microelectrode arrays by determining the best fit between experimental and simulated CA responses (Shoup and Szabo, 1984), and will be discussed in more detail in section 2.4.1.

2.3.2.4 Decoration of electroactive areas by electrochemical copper deposits

In order to image electroactive sites on electrode surfaces, electrodeposition of copper on TTF-TCNQ electrodes was performed. At TTF-TCNQ this was accomplished by exposing the differently treated electrodes to 50 mM $CuSO_4$ in 0.5 M potassium acetate at a potential of -0.15 V versus Ag/AgCl until 20 C of charge had passed (approximately 30 seconds). Copper deposition was performed in a similar manner using the spin coated TTF-TCNQ/PVC films (see page 46).

2.3.3 Other Techniques

2.3.3.1 Quartz crystal microbalance

The QCM apparatus used (Figure 2.3a) was similar to the setup described in the literature (Ward, 1988; Buttery, 1991), and consisted of a 5 MHz AT-cut quartz crystal (Valpey-Fisher) driven by a homemade oscillator designed to drive the crystal at its resonant frequency. The frequency of the QCM was monitored with a Hewlett-Packard 5384A frequency counter and recorded with a Digital Equipment Corporation PDP-11/73 computer.

Gold electrodes (2000 Å thick) were deposited on chromium underlayers (200 Å) on both sides of the crystal by evaporative techniques. The patterns were arranged so that the gold leads from the outer edges of the crystal to the center circular pad on opposite sides did not overlap (Figure 2.3b). The quartz crystal was mounted between two O-rings confined by standard glass fittings and a metal clamp.

The quality factor of the quartz crystals (a resonant system) can be expressed as $Q_Q = 2\pi$(energy stored per cycle/energy dissipated per cycle). Quartz crystals exhibit values of $Q_Q > 80{,}000$ in air, although values > 2000 are generally sufficient for frequency stability (Bottom, 1982; Salt, 1987). Impedance analysis to determine quartz crystal

Figure 2.3 Schematic of (a) quartz crystal microbalance and electrochemical apparatus; and (b) gold electrode patterns deposited on AT cut quartz crystal.

a)

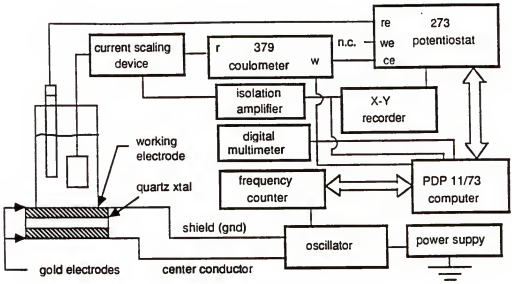
current scaling device
r 379 coulometer w
n.c.
re 273 potentiostat
we
ce
isolation amplifier
X-Y recorder
digital multimeter
working electrode
quartz xtal
frequency counter
PDP 11/73 computer
shield (gnd)
oscillator
power suppy
gold electrodes
center conductor

b)

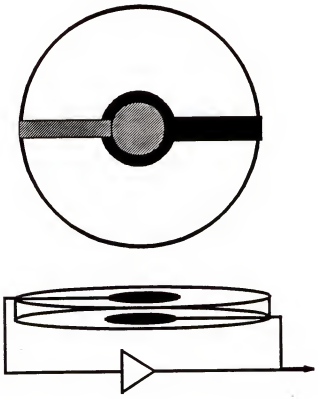

conductances and quality factors was performed with a Hewlett-Packard 4194A Impedance/Gain-Phase Analyzer.

For thin films exhibiting rigid-layer behavior (Lu and Lewis, 1972), electrochemically induced mass changes at one of the electrodes of a QCM can be determined from frequency changes by the Sauerbrey relationship (Sauerbrey, 1959),

$$\Delta f = \frac{-2f_o^2 \Delta m}{A_{piezo}(\rho_q \mu_q)^{1/2}} \tag{2.10}$$

where Δf is the shift in resonant frequency, f_o is the parent frequency of the quartz crystal, Δm is the corresponding mass change, A_{piezo} is the piezoelectrically active area, ρ_q is the density of quartz (2.648 g cm^{-3}), and μ_q is the shear modulus (2.947 X 10^6 N cm^{-2} for AT-cut crystal) (Stockbridge, 1966). A positive change in frequency corresponds to a mass loss (17.68 ng Hz^{-1} cm^{-2} for crystals used in these studies). Rigid-layer behavior of the spin coated TTF-TCNQ/PVC films was verified by impedance analysis which showed sharp conductance peaks and reasonably high quality factors (Q_Q > 20,000). Rigid-layer behavior was also confirmed by comparing the mass of electrodeposited copper, Cu^0, as determined from the observed frequency change, to the amount of Cu^0 determined from the charge measured during controlled potential deposition of Cu^0. Assuming 100% faradaic efficiency during deposition, the amount of Cu^0 determined by both methods agreed within 1%. For example, an electrode yielding 9.8 X 10^{-3} C of total charge, corresponding to 2.54 X 10^{-8} moles Cu^0/A_{piezo}, afforded Δf = 500 Hz, corresponding to 2.52 X 10^{-8} moles Cu^0/A_{piezo}.

2.3.3.2 Scanning tunneling and atomic force microscopy

STM (Binnig and Rohrer, 1986) and AFM (Rugar and Hansma, 1990) were performed in air using a Nanoscope II® (Digital Instruments). Both STM and AFM images were generated by maintaing a constant signal (current and force, respectively) between the

tip and the sample. This was achieved by controlling the potential applied to a calibrated piezo element in a feedback circuit. Pt-Ir (80/20) Nanotips®, used to obtain STM images, were used as received. STM images were obtained in the constant current mode with a tunneling current of 2 nA, a tip bias of +100 mV and a scan rate of 40 Hz. To insure that the STM tips were free from contamination, HOPG was intermittently imaged with atomic resolution.

AFM studies were performed in the constant force mode or constant cantilever displacement, using 100 μm Si_3N_4 triangular cantilevers with a spring constant of 0.58 N/m at a scan rate of 20 Hz. Under these conditions, a constant force between 1 and 100 nN was being applied to the sample. All AFM images produced by this method were stable during continuous scanning of the surface, suggesting that the surface was not being damaged as a result of rastering the tip across the surface.

The images presented here are representative of many images taken at different points on each sample. All STM and AFM images were lowpass filtered to remove high frequency noise which did not alter the topographical heights (Chang and Bard, 1990).

2.4 Numerical Methods

All calculations were performed on an Intel® 80386 based PC. All programs were written in compilable BASIC.

2.4.1 Simulation of Current Response at Microelectrode Arrays

Dimensions of microelectrode arrays were determined by fitting simulated CA data generated for microelectrode arrays of varying dimensions to experimental data. The dimensions of the arrays were expressed in terms of the dimensions of a unit cell in the array (see Figure 1.3c) where r is the radius of the active area and R_o is the radius of the geometric

area of the unit cell. The quality of the fit was determined from the sum of the square of the residuals (Massart et al., 1988), Σe_i^2, where e_i is a residual or the difference between a set of corresponding experimental and simulated data points. The best fit was taken as the maximum value of $(\Sigma e_i^2)^{-1}$. In plots of $(\Sigma e_i^2)^{-1}$ versus R_o, each value of $(\Sigma e_i^2)^{-1}$ corresponds to the maximum value of $(\Sigma e_i^2)^{-1}$ determined as a function of r at a constant R_o value. The program keeps track of the value of r and R_o corresponding to each $(\Sigma e_i^2)^{-1}$ value. Plots of $(\Sigma e_i^2)^{-1}$ versus R_o give the observer information about the distribution and quality of the fit at various values of R_o. The best fit (i.e. the maximum of a plot of $(\Sigma e_i^2)^{-1}$ versus R_o) is taken as the dimensions of the average unit cell of the array.

The current measured at a unit cell microelectrode, i_m, with dimensions r and R_o (Figures 1.3c and 1.4b) can be described by the expression

$$i_m = 4rnFDC^* f(\tau,\theta) \qquad (2.11)$$

where $f(\tau,\theta)$ is the normalized current which is a function of dimensionless time (τ) and the fraction of inactive area (θ), where τ and θ are defined in equations 1.11 and 1.16, respectively. The normalized current in equation 2.11 is similar to that described by the bracketed terms in equation 1.10 for a single electrode with the exception that in addition to describing the current response transition from semi-infinite linear diffusion to the active area to radial diffusion to the active area as time (or τ) increases, $f(\tau,\theta)$ also described an additional transition from radial diffusion to the active area to semi-infinite linear diffusion to the entire geometric area. These transitions are schematically represented in Figure 1.4 where diffusion layer profiles (solid lines) range from semi-infinite linear diffusion to the active area to semi-infinite linear diffusion to the geometric area.

Simulation of CA responses at arrays of microelectrodes in this work is based on the analytical expression introduced by Shoup and Szabo for dimensionless current at a microelectrode unit cell in an array

$$f(\tau,\theta)=\sqrt{\frac{\pi}{4\tau}}+\frac{\pi}{4}+(1-\frac{\pi}{4})\exp[\frac{-B\theta^2(3-2\theta)}{\sqrt{\tau}}]- \exp\{-[\frac{\sqrt{\pi}}{2(\frac{\theta}{1-\theta})}+B(1-\frac{\pi}{4})\theta^2(3-2\theta)]/\sqrt{\tau}\}(1+\frac{3\sqrt{\pi}\theta^3}{2\tau(1-\theta)})^{-1} \quad (2.12)$$

where B = 0.7823 (Shoup and Szabo, 1984). This function accurately describes the normalized current at short times (i.e., characteristic of the active area), long times (i.e., characteristic of the geometric area), and at intermediate times. In the simulation $0<\theta<1$, $r<R_o$ and i_m is determined from equation 2.11. The number of microelectrodes, N, with a dimension R_o is determined by

$$N=\frac{A}{\pi R_o^2} \quad (2.13)$$

where A is the geometric area of the microelectrode array, and the total simulated current, i, is expressed as

$$i=Ni_m \quad (2.14)$$

Optimal values of r and R_o can be determined from the best fit between the experimental and simulated currents.

The optimization program, whose source code is presented in Appendix B, determines the dimensions of the microelectrode array which best fit the normalized experimental current in terms of magnitude, and the transition from currents reflecting active to total geometric area. As illustrated in the program algorithm in Figure 2.4, the program accepts as input the geometric area of the microelectrode array (determined by CC) and the CA response (i(t)).

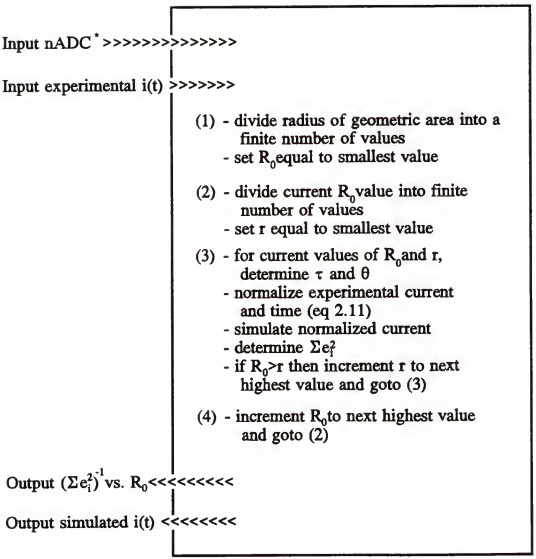
Input nADC* >>>>>>>>>>>>>>
Input experimental i(t) >>>>>>>
(1) - divide radius of geometric area into a finite number of values
- set R_0 equal to smallest value
(2) - divide current R_0 value into finite number of values
- set r equal to smallest value
(3) - for current values of R_0 and r, determine τ and θ
- normalize experimental current and time (eq 2.11)
- simulate normalized current
- determine Σe_i^2
- if R_0>r then increment r to next highest value and goto (3)
(4) - increment R_0 to next highest value and goto (2)
Output $(\Sigma e_i^2)^{-1}$ vs. R_0 <<<<<<<<<
Output simulated i(t) <<<<<<<<

Figure 2.4 Chronoamperometric simulation and optimization program algorithm. Experimentally determined electrode geometric area, A, n, D, C^*, and chronoamperometric response, i(t), are accepted as input.

The program then divides the number of possible R_o values into 50 values between 0 and the radius of the entire geometric area of the electrode. Beginning with the smallest R_o value and proceeding through to the largest value, for each value of R_o, the program divides the number of r values into 50 values ranging between 0 and R_o. Based on each value of R_o and r, τ and θ are determined from equations 1.11 and 1.16, respectively. For each value of R_o, equation 2.13 is used to determine the number of unit cells within the total geometric area. The experimental current is then reduced to the magnitude that would be produced by a single unit cell, i_m, by dividing the total current by N (eq 2.14). Finally, the current is normalized with respect to $4rnFDC^*$ (eq 2.11) resulting in $f(\tau,\theta)$. Values of $f(\tau,\theta)$ are then simulated (eq 2.12) corresponding to the normalized time for each experimental data point, and the sum of the square of the residuals, Σe_i^2, is determined. The program keeps track of the value of r which correspond to the maximum $(\Sigma e_i^2)^{-1}$ for each value of R_o and outputs these values, $(\Sigma e_i^2)^{-1}$ versus R_o, and simulated i(t) based on the values of R_o and r which resulted in the best fit.

In most of the experiments in this study, the optimization procedure resulted in a best fit simulated current greater than the experimental current. This result suggests a nonuniform microelectrode structure. For example, a structure where microelectrodes are not evenly distributed over the entire surface of the electrode, as shown schematically in Figure 2.5a, may result in aggregates of microelectrodes (Figure 2.5b). At sufficiently short times, the observed CA response will be characteristic of the individual microelectrodes which form the aggregates (small dots in Figure 2.5b). As time progresses and diffusion layer overlap between microelectrodes occurs, the response will become characteristic of the geometric area of microelectrode aggregates (larger dots in Figure 2.5c). A structure such as shown in Figure 2.5a is therefore bimodal in the sense that small microelectrodes form microelectrode aggregates (Figure 2.5b) which result in responses characteristic of larger microelectrodes

Figure 2.5 (a) Microelectrode array model showing uneven distribution of microelectrodes (dots indicate active areas); (b) aggregates of smaller microelectrodes; (c) approximation of microelectrode aggregates by a single larger microelectrode.

a)

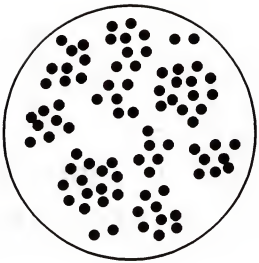

b)

c)

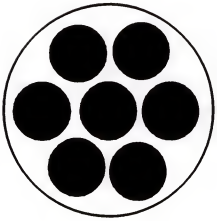

(Figure 2.5c) at sufficiently long times. Because the simulation of the total current assumes an equal distribution of microelectrodes, under conditions of nonuniform distribution of microelectrodes (Figure 2.5a), N determined from R_o and A is artificially large, and as a result, so is the total simulated current.

In order to accommodate a structure where microelectrodes are not evenly distributed, the optimization program is run twice. In the first iteration, values of r and R_o are determined for the best fit, then a new geometric area, A_{new}, is determined,

$$A_{new}=A(1-\theta_1) \tag{2.15}$$

where θ_1 is determined from the optimal values of r and R_o determined in the first iteration. A_{new} which is obtained, is a geometric area without the inactive area associated with the smaller microelectrodes in the array obtained in the first iteration. When the simulation is run the second time (with A_{new} instead of A), the smaller dimensions of r and R_o no longer give the best fit. The new optimal dimensions of r and R_o are characteristic of much larger microelectrodes, which are the next best approximation (Figure 2.5c). It is likely that the larger dimensions are a good approximation because the aggregates of small microelectrodes such as in Figure 2.5b result in a response similar to a larger microelectrode such as in Figure 2.5c at long times, due to diffusion layer overlap. Typically, the second iteration resulted in an excellent fit between experimental and simulated results.

The simulated CA response is determined from the values of $f(\tau,\theta)$ which resulted in the best fit as described above. Equations 2.11 and 2.15 are used to convert $f(\tau,\theta)$ into a CA response which can in turn be compared to the original experimental data. In order to determine the total inactive area, θ, associated with the inactive area between microelectrodes in the aggregates (determined from the first iteration, θ_1) and the inactive area between the

aggregates themselves (determined from the second iteration, θ_2), the total active area after the second iteration, A_{active}, is determined,

$$A_{active} = (1 - \theta_2) A_{new} \tag{2.16}$$

The ratio of the total active area to the original geometric area (i.e. the fraction of active area) is in turn used to determine the total fraction of inactive area,

$$\theta = 1 - \frac{A_{active}}{A} \tag{2.17}$$

2.4.2 Simulation of Reversible and Quasi-Reversible Voltammetric Response

Simulations of diffusion controlled voltammetric response were performed for two purposes: (i) to determine variations from diffusion controlled behavior of experimental data due to nonlinear diffusion; (ii) to generate ideal diffusion controlled responses on which to demonstrate the effect of semi-integration techniques; and (iii) to simulate voltammetric responses in the presence of a thin-layer model.

As described in section 2.3.2.1, CV and LSV involve ramping of potential at a working electrode in the presence of redox active species in solution (Nicholson and Shain, 1964). For a heterogeneous electron transfer reaction when the potential is scanned, the heterogeneous rate coefficients (eqs 1.7 and 1.8) change exponentially. Under conditions where the rate of electron transfer for the forward and reverse reaction is fast enough to maintain nernstian conditions at the electrode surface (i.e. the ratio of surface concentrations of Ox and Red are determined by the Nernst equation),

$$E(t) = E^{o'} + \frac{RT}{nF} \ln \frac{C_{Ox}(0,t)}{C_{Red}(0,t)} \tag{2.18}$$

the response is referred to as reversible. Reversible CV responses can be identified by a separation of anodic and cathodic peak potentials, ΔE_p, of 59/n mV where n is the number of

electrons transferred in the redox reaction. As will be discussed in more detail in section 4.3.2 the current potential curve is proportional to the transcendental function, $\sqrt{\pi}\,\chi(at)$, where at is normalized potential (eq 4.44). Values of $\sqrt{\pi}\,\chi(at)$ where determined using an analytical function ($x=at$)

$$\sqrt{\pi}\,\chi(x)=L+Mx-Nx^2+\left(\frac{\pi}{2}\right)^{1/2}\sum_{k=1}^{\infty}\left[\frac{(\beta-x)^{1/2}(\beta+2x)}{\beta^3}-\frac{8b^2+12bx-15x^2}{8b^{7/2}}\right] \qquad (2.19)$$

and where L = 0.380104813, M = 0.118680871, N = 0.043920560, ß = $[(2k-1)^2\pi^2 + x^2]^{1/2}$, and b = $(2k-1)\pi$ (Oldham, 1979). In this work it was found that summing from k=1 to 100 in equation 2.19 resulted in values of $\sqrt{\pi}\,\chi(x)$ which were in agreement with those reported in the literature for values of x between -10 and 10 (Oldham, 1979).

Under conditions where the rate of electron transfer is not sufficiently fast to maintain nernstian conditions at the electrode surface as the potential is scanned, the voltammetric response deviates from that expected for a reversible response. The deviation is observed as an increase in ΔE_p, or the shifting of peak potentials away from the formal potential. For values of ΔE_p ranging from 61/n to 212/n mV, the response is considered quasi-reversible. In practice, under quasi-reversible conditions, ΔE_p increases as scan rate increases or as k^o decreases. Nicholson has determined the dependance of ΔE_p on k^o and ν, expressed as the kinetic parameter, ψ (eq 2.1) (Nicholson, 1965). The kinetic parameter introduced by Nicholson, shown in equation 2.1, is similar to the dimensionless standard heterogeneous rate, Λ, introduced by Matsuda and Ayabe (Matsuda and Ayabe, 1955; Bard and Faulkner, 1980),

$$\Lambda=\sqrt{\pi}\psi=k^o(aD_{Red})^{-1/2}(D_{Ox}/D_{Red})^{\alpha/2} \qquad (2.20)$$

($a=nF\nu/RT$) which can be considered as a measure of reversibility.

Quasi-reversible cyclic voltammograms were simulated by digitizing current function values (Bard and Faulkner, 1980) at Λ values closest to those determined from the experimental results. Values of Λ were determined from experimental results by first obtaining ψ from peak separations (ΔE_p) using the methods of Nicholson (Nicholson, 1965) as described in section 2.3.2.1. The ψ values were in turn used to calculate Λ using equation 2.20 (0.7 and 0.8 at pressed pellet and unpolished polymer paste TTF-TCNQ/PVC electrodes, respectively). The voltammograms were simulated using current function values provided in the literature for $\Lambda = 1.0$ (Bard and Faulkner, 1980), which was the closest Λ value to those determined for pressed pellet and polymer paste.

Digital simulations of CV responses in the presence of a thin-layer model were based on routines published in the literature (Feldberg, 1969). In the simulation, the solution adjacent to the electrode surface is divided into finite volume elements. Diffusion is simulated by altering the concentration in each volume element based on the concentrations in the volume elements on either side. A concentration gradient can be produced by altering the concentration within the volume element at the electrode surface, which in turn causes a gradual change in concentrations within each volume element as a function of distance from the electrode surface (Feldberg, 1969). In the simulation used in this work an additional step was added, step (4) in the algorithm shown in Figure 2.6, to account for the equilibrium between bulk solution and a thin film at the electrode surface. This involved altering the surface boundary condition in the simulation to include equilibrium (K_{eq}) between the first and second volume element for Ox and Red where the thin film was represented by the first volume element having the same thickness as all the volume elements.

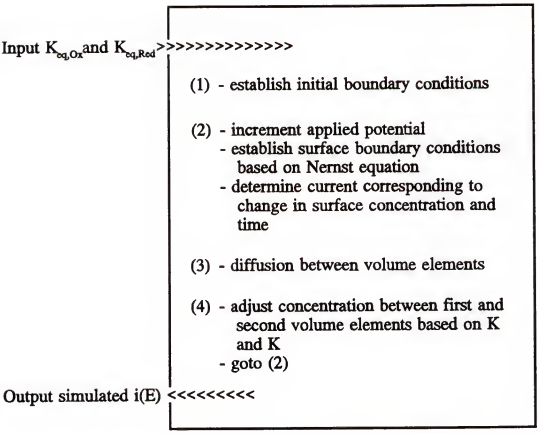
Input $K_{eq,Ox}$ and $K_{eq,Red}$ >>>>>>>>>>>>>
(1) - establish initial boundary conditions
(2) - increment applied potential
- establish surface boundary conditions based on Nernst equation
- determine current corresponding to change in surface concentration and time
(3) - diffusion between volume elements
(4) - adjust concentration between first and second volume elements based on K and K
- goto (2)
Output simulated i(E) <<<<<<<<<

Figure 2.6 Program algorithm for cyclic voltammetric simulation in the presence of the thin-layer model. Equilibrium constants, $K_{eq,Ox}$ and $K_{eq,Red}$, describe concentration equilibrium of Ox and Red between the first and second volume elements adjacent to the electrode surface in a finite element representation of diffusion.

2.4.3 Numerical Semi-integration

The solution to the diffusion equations for semi-infinite linear diffusion conditions where only Ox is initially present results in an expression which relates surface concentration to observed current,

$$C_{O_x}(0,t)=C_{O_x}^{*}-\frac{1}{nFAD_{O_x}^{1/2}}\left[\frac{1}{\pi^{1/2}}\int_0^t \frac{i(u)}{(t-u)^{1/2}}du\right] \tag{2.21}$$

where the bracketed term represents the semi-integration of the response resulting from diffusing species, i(t). Semi-integration is often represented by the operator $d^{-1/2}/dt^{-1/2}$, so that the semi-integrated experimental data, I(t), is represented as

$$\frac{d^{-1/2}i(t)}{dt^{-1/2}}=I(t) \tag{2.22}$$

Semi-integration is achieved through a numerical technique described in the literature (Bard and Faulkner, 1980). The source code for the program which performs numerical semi-integration is shown in Appendix A. In the case of LSV, the voltammograms are expressed as discrete evenly spaced data points (i, E). As illustrated in the program algorithm in Figure 2.7, the voltammogram is converted from a current potential curve (i(E)) to a current time curve (i(t)) by setting the initial potential (E_i) to t=0 and converting each subsequent potential value to a time value based on the potential with respect to the initial potential and the scan rate,

$$t=|Ei-E|\nu \tag{2.23}$$

This conversion results in evenly spaced data points (i.e. the time difference between data points, Δt, is constant). Once the data is expressed with respect to time, numerical integration is obtained with the algorithm

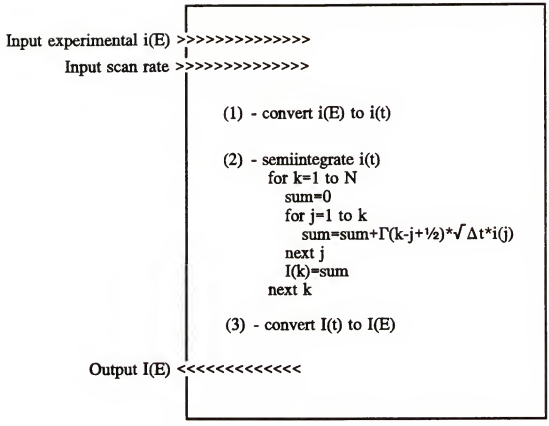

Figure 2.7 Numerical semi-integration program algorithm. Experimental voltammetric data, i(E), and scan rate are accepted as input. Step (2) performs the numerical semiintegration based on equations 2.24 and 2.25.

$$I(k\Delta t)=\frac{1}{\pi^{1/2}}\sum_{j=1}^{j=k}\frac{\Gamma(k-j+\frac{1}{2})}{(k-j)!}\,\Delta t^{1/2}i(j\Delta t) \tag{2.24}$$

which utilizes the Gamma function which has the form (Spanier and Oldham, 1987),

$$\Gamma(n+\frac{1}{2})=\sqrt{\pi}\;\frac{1\cdot3\cdot5\cdot7\ldots(2n-1)}{2^n} \tag{2.25}$$

and should not to be confused with surface excess. In this algorithm, as shown in Figure 2.7, the voltammogram, expressed as a function of time, is divided into N discrete values. For each data point, from k=0 to k=N, the summation in equation 2.24 is determined from j=1 to **k**. Semi-integration of experimental linear sweep voltammograms was performed following background subtraction.

CHAPTER 3
IDENTIFICATION AND CONTROL OF MICROELECTRODE ARRAY STRUCTURE AT ELECTRODE SURFACES

In this chapter, several methods for the characterization of electrode surface microstructure will be discussed. Specifically, these techniques will be used to identify the surface microstructure of TTF-TCNQ and graphite electrodes. It will be demonstrated that the surface microstructure of these electrodes can be approximated by a microelectrode array model, and that increases in activity at these electrodes, afforded by various methods of treatment, can be accounted for by changes in the dimensions of the microelectrode arrays. Characterization of microelectrode arrays is achieved with the following methods: (i) observed copper deposits using SEM; (ii) by fitting simulated CA responses to experimental data; and (iii) by direct observation of surface defects with AFM.

3.1 Effects of Microelectrode Array Structure on Response

The effects of nonlinear diffusion at partially blocked electrode surfaces have been addressed theoretically by Amatore and coworkers (Amatore et al., 1983). In their work, they developed models of surfaces involving microscopic inhomogeneities (i.e. localized active sites). Using a microelectrode array model, as shown in Figure 1.3, it was found that a voltammetric response, in terms of reversibility and shape, depends on four experimental parameters including k^o, R_o, ν, and θ. The significance of this work is that the voltammetric behavior of a microelectrode array, of known dimensions (R_o and r), fabricated with a characterized material (i.e. k^o known for reaction of interest), can be predicted. In addition,

the dependence of voltammetric response on scan rate (ν) can be predicted, including transitions from responses characteristic of diffusion to individual microelectrodes to responses characteristic of diffusion to the entire geometric area as discussed in section 1.2 and illustrated in Figure 1.4. The predicted voltammetric behavior of a microelectrode array is shown as inlays in zone diagram 3.1. The dependence of response on the four experimental parameters is shown in the upper right hand corner of the zone diagram.

Because of the interrelationship between experimental parameters and their effect on response (as was discussed for a completely active electrode in section 2.4.2 for the dependance of Λ on ν and k^o in eq 2.20), it is convenient to express the effects of the experimental parameters in terms of dimensionless parameters. Amatore and coworkers introduced two dimensionless parameters: $\Lambda(1-\theta)$ and $K\lambda^{1/2}$ which are shown in zone diagram 3.1 and are defined as follows (Amatore et al., 1983). The first dimensionless parameter,

$$\Lambda(1-\theta) = k^o(1-\theta)\left(\frac{nF\nu D_{Red}}{RT}\right)^{-1/2}\left(D_{Ox}/D_{Red}\right)^{\alpha/2} \qquad (3.1)$$

expresses the degree of reversibility, and is the product of the dimensionless standard heterogeneous rate constant, Λ, defined in equation 2.20, and the fraction of active area, $(1-\theta)$, where θ is a function of r and R_o and is defined in equation 1.16. The significance of this parameter is that not only does Λ affect reversibility, as was discussed in section 2.4.2 for completely active electrodes, but so does θ. For example, if the diffusion layer is sufficiently thicker than the dimensions of the array (depicted in the right hand side of Figure 3.1), a decrease in the fraction of active area $(1-\theta)$ will result in an increase in peak separation (ΔE_p) which corresponds to a decrease in the apparent standard heterogeneous rate constant as discussed in section 2.4.2. The effect of $(1-\theta)$ on ΔE_p demonstrates the influence of surface

Figure 3.1 Zone diagram of cyclic voltammetric characteristics (shown as inlays) as a function of $K\lambda^{1/2}$ and $\Lambda(1-\theta)$, and as a function of experimental parameters (unit cell radius, R_o, standard heterogeneous rate constant, k^o, fraction of active area, $1-\theta$, and scan rate, ν) for disk electrode array.

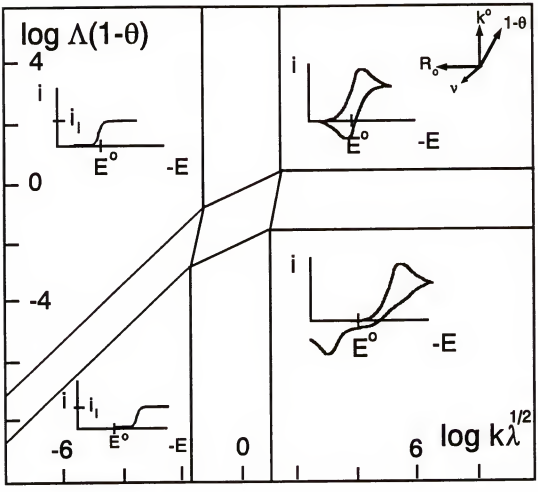
log Λ(1-θ)
4
0
-4
i
i_l
E^o
-E
-6
0
6
log $k\lambda^{1/2}$
k^o
1-θ
R_o
ν

structure in terms of microelectrode array dimensions on the reversibility and in turn apparent electrode kinetics.

The second dimensionless parameter describes the dominant diffusional mode and as a result the shape of the voltammetric response, and is defined as

$$K\lambda^{1/2} = \frac{(\frac{DRT}{nF\nu})^{1/2}}{2R_o 0.3(1-\theta)^{-1/2}} \tag{3.2}$$

where K is the ratio of active to inactive area,

$$K = \frac{(1-\theta)}{\theta} \tag{3.3}$$

and

$$\lambda^{1/2} = (\frac{RT}{nFv})^{1/2} \frac{D^{1/2}}{2R_o} \frac{\theta}{(1-\theta)} 0.3(1-\theta)^{1/2} \tag{3.4}$$

Equation 3.2 accounts for the dependence of the diffusional mode (i.e radial or semi-infinite linear diffusion) on the dimensions of the array, expressed as R_o and θ, and the time scale of the experiment expressed as scan rate. For example, as log $k\lambda^{1/2}$ decreases (i.e. R_o and/or ν increases), it can be predicted from Figure 3.1 that the shape of cyclic voltammograms will approach a steady-state, or sigmoidal, voltammogram (Amatore et al., 1983). This will be observed for the array where the fraction of active area is fairly low as the scan rate increases.

3.2 Microelectrode Array Structure at TTF-TCNQ Electrodes

3.2.1 Scanning Electron Microscopy Imaging of TTF-TCNQ Electrode Surface Structures

Scanning electron microscopy (SEM) data, in Figure 2.1a, clearly show the arraylike structure of the polymer paste TTF-TCNQ/PVC electrode. The polymer paste electrode

consists of very small TTF-TCNQ crystals which, with the insulating PVC as a binder, form a heterogeneous surface. The micrograph shows that if the TTF-TCNQ crystals (ca. 10-100 μm) represent electroactive regions and insulating regions, depending on whether the conducting crystals are in electrical contact with the rest of the working electrode or isolated by insulating PVC, the electrochemical response may exhibit microelectrode array behavior.

As shown in Figure 2.1c, heterogeneity at the high-pressure pellet electrode surface is on a much smaller scale (ca. 1-10 μm) than that observed for the polymer paste electrode. The reduced size of inhomogeneities is presumably due to the crushing of the original TTF-TCNQ crystals during compression. Because of the combination of the reduced size of inhomogeneities and the absence of insulating PVC as a binder in the case of high-pressure pellet electrodes, microelectrode array behavior should reflect an array with significantly smaller dimensions (ca. 1-10 μm) than that of the polymer paste electrode (ca. 10-100 μm).

Polishing the polymer paste electrode (Figure 2.1b) results in compression of TTF-TCNQ crystals at the electrode surface and produces relatively smooth areas more closely resembling the surface of the pellet electrode seen in Figure 2.1c than the original unpolished polymer paste electrode. As a result, polishing is expected to increase the fraction of active area relative to the unpolished polymer paste electrode (Figure 2.1a).

3.2.2 Evidence of Microelectrode Array Structure in Electrochemical Response at TTF-TCNQ Electrodes

As discussed in section 3.2.1, the heterogeneity of TTF-TCNQ electrode surfaces as seen in SEMs (Figure 2.1) suggests that the surface structure can be approximated by a microelectrode array model (Figure 1.3) with dimensions r and R_s. Qualitative verification of a microelectrode array structure can be obtained by varying the time scale of the electrochemical experiment (e.g. scan rate in CV) as discussed in section 3.1. For example,

the theory predicts that at sufficiently slow scan rates, a microelectrode array with a large fraction of active area (log $k\lambda^{1/2} > 1$, Figure 3.1) will result in faradaic currents proportional to the total geometric area (Reller et al., 1984; Penner and Martin, 1987) without evidence for the microelectrode structure (i.e. effects of nonlinear diffusion will not be observed in the shape of the voltammetric response). As the scan rate increases or the time scale decreases (i.e. log $k\lambda^{1/2}$ is decreased), the diffusion layer thickness will be reduced, eventually resulting in nonlinear diffusion to individual microelectrodes (log $k\lambda^{1/2} < 1$, Figure 3.1). Under these conditions, the diffusion layer thickness is on the order of, or less than, the separation between individual microelectrodes ($\delta \leq R_s$) as illustrated in Figure 1.4a. In addition, the theory discussed in section 3.1 also predicts that at a microelectrode array, with a large fraction of active area and at sufficiently slow scan rates (log $k\lambda^{1/2} > 1$, see Figure 3.1), the only evidence of a microelectrode array structure will be in the apparent standard heterogeneous rate constant (i.e. ΔE_p). As the fraction of active area decreases (log $\Lambda(1-\theta) < 0$, see Figure 3.1), ΔE_p will increase which corresponds to a decrease in the apparent standard heterogeneous rate constant as discussed in section 2.4.2.

Figure 3.2 shows the CV response for the reduction of $Fe(CN)_6^{3-/4-}$ at TTF-TCNQ/PVC unpolished polymer paste and high pressure pellet electrodes. $Fe(CN)_6^{3-/4}$ was chosen as a probe because it undergoes a fast, simple, outer sphere one-electron transfer, and undergoes unmediated one-electron reduction at TTF-TCNQ/PVC electrodes as will be demonstrated in section 4.2.2. As shown in Figure 3.2b and 3.2d, the behavior of $Fe(CN)_6^{3-/4-}$ at the unpolished TTF-TCNQ/PVC polymer paste electrode follows the predicted changes in response as a function of scan rate. With an increase in scan rate the shape of cyclic voltammograms approaches that of a steady-state voltammogram (Figure 3.2b), while at slow scan rates, the response is characteristic of semi-infinite linear diffusion (Figure 3.2d).

Figure 3.2 Experimental (——) and calculated (O) cyclic voltammograms of 5 mM $Fe(CN)_6^{3-/4-}$ in 1.0 M KCl at high-pressure pellet (A, C) and 13:1 unpolished polymer paste (B, D) TTF-TCNQ electrodes. Scan rates were 100 $mV\text{-}s^{-1}$ (C,D) and 5000 $mV\text{-}s^{-1}$ (A, B).

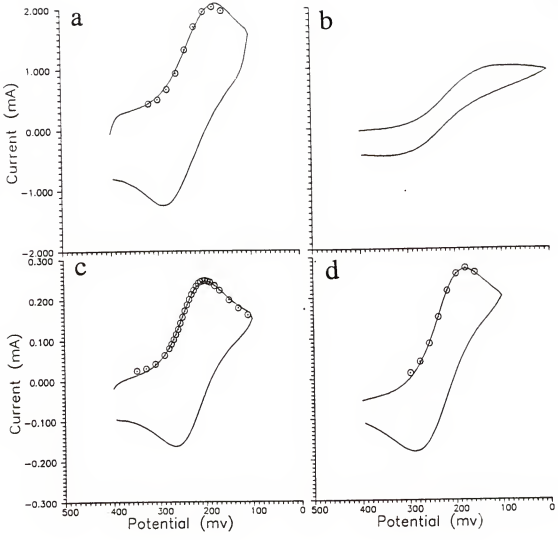
a
b
c
d
Current (mA)
Current (mA)
2.000
1.000
0.000
-1.000
-2.000
0.300
0.200
0.100
0.000
-0.100
-0.200
-0.300
500
400
300
200
100
0
Potential (mv)
Potential (mv)

At high-pressure pellet electrodes the distance between the microelectrodes in the array, as predicted from SEM data in section 3.2.2, should be significantly smaller and so, as a result, should be the fraction of inactive area. At these electrodes the predicted and observed (Figure 3.2a and 3.2c) shapes of CVs are the same (i.e. characteristic of semi-infinite linear diffusion) over a wider range of scan rates as at electrodes of standard size where the active and geometric areas are the same.

As described earlier in this section, theory also predicts that when the diffusion layer thickness is sufficiently larger than R_a, the shape of CVs are the same as that at electrodes of equivalent total geometric area. The apparent standard heterogeneous rate constant will provide the only indication that the array structure is indeed present. The apparent standard heterogeneous rate constant will be a function of the fraction of active area and will decrease as the active area decreases. In practice this means that peak-to-peak separation, ΔE_p, will be larger at an array electrode than at normal electrodes where the total area is active (see lower right inlay in Figure 3.1). At TTF-TCNQ pellet electrodes, peak-to-peak separation for $Fe(CN)_6^{3-/4-}$ is ca. 69 mV at slow scan rates (Table 3.1), characteristic of a reversible or fast reaction. At unpolished polymer paste electrodes, under conditions where semi-infinite linear diffusion response is observed (at same low scan rate), ΔE_p is ca. 86 mV (Table 3.1), which is consistent with a decrease in the fraction of active area at the unpolished polymer paste electrode relative to the pellet electrode.

Further evidence of the difference in the fraction of active area between the polymer paste and pellet electrodes is seen in Figure 3.2 by the change in relative magnitudes of peak currents of the two electrodes at the two scan rates. At the slow scan rate, the relative magnitudes of the peak currents are the same, suggesting that the geometric areas of both

Table 3.1. Electrochemical response of $Fe(CN)_6^{3-/4-}$ at TTF-TCNQ electrodes

electrode	ΔE_p[a], mV
unpolished	86
polished	69
pellet	69

[a] 1 mM $Fe(CN)_6^{3-/4-}$, 5 mV-s^{-1}, pH 7.0, 0.5 M phosphate buffer.

electrodes are the same, while at the higher scan rate, the magnitude of the peak current at the unpolished polymer paste electrode is smaller than that observed for the pellet electrode. This suggests that at the higher scan rate, the response of the unpolished polymer paste electrode reflects the active area, while the response of the pellet electrode still reflects the geometric area.

The response characteristics of polymer paste electrodes can be altered by polishing the surface. As described in section 3.2.1, polishing polymer paste electrodes results in compression of TTF-TCNQ crystals at the electrode surface and produces relatively smooth areas, more closely resembling the surface of the pellet electrode, thereby increasing the fraction of active area relative to the unpolished polymer paste electrode. Theory predicts that an increase in the fraction of active area will result in an increase in the apparent standard heterogeneous rate constant (i.e. decrease ΔE_p). This behavior is observed in Table 3.1 where the ΔE_p for $Fe(CN)_6^{3-/4-}$ at the polished polymer paste electrode approaches that observed for the pellet electrode (69 mV).

3.2.3 Determination of Microelectrode Array Dimensions

A CA response of 2 mM $Fe(CN)_6^{3-/4-}$ was used to determine the dimensions of the microelectrode array at an unpolished TTF-TCNQ/PVC polymer paste electrode by finding the best fit between experimental and simulated responses as described in section 2.4.1.

Figure 3.3a shows a plot of the inverse of the sum of the squared residuals ($(\Sigma e_i^2)^{-1}$), where the residuals (e_i) are the differences between corresponding experimental and simulated data points, determined for various microelectrode array unit cell dimensions (R_o and r). Each value of $(\Sigma e_i^2)^{-1}$ shown in the figure corresponds to the maximum $(\Sigma e_i^2)^{-1}$ for various values of r at a constant R_o value, as described in section 2.4.1. The dimensions of the

Figure 3.3 (a) Plot of $(\Sigma e_i^2)^{-1}$ versus R_o for unpolished 13:1 TTF-TCNQ/PVC polymer paste electrode after background subtraction, where CA was performed in 2 mM $Fe(CN)_6^{3-/4-}$/1 M KCl and potential was stepped from +0.400 to 0.000 V versus SCE with a pulse width of 1000 ms. (b) Experimental (O) and simulated (solid and dashed lines) chronoamperometric response based on microelectrode dimensions determined from the least-squares optimization program; first iteration r = 10, R_o = 12 μm (——); second iteration r = 119, R_o = 121 μm (- - -).

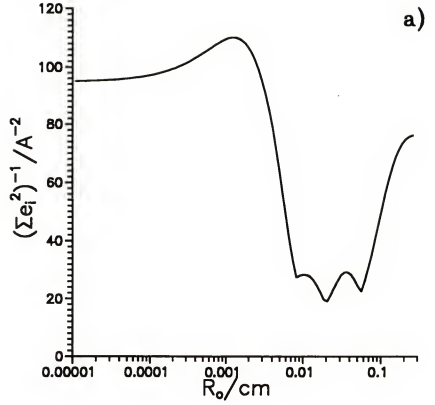
a)
120
100
80
60
40
20
0
$(\Sigma e_i^2)^{-1}/A^{-2}$
0.00001
0.0001
0.001
0.01
0.1
R_o/cm

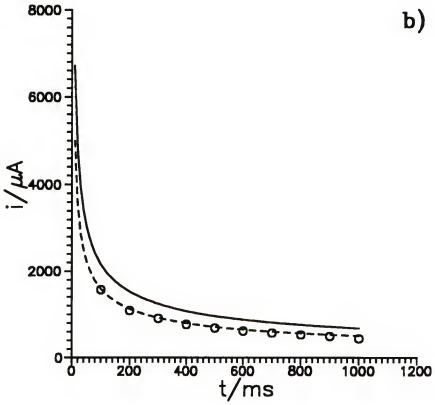
b)
8000
6000
4000
2000
0
i/μA
0
200
400
600
800
1000
1200
t/ms

average microelectrode unit cell, determined from the first iteration, are r = 10 μm and R_o = 12 μm which corresponds to $\theta_1 = 0.30$. The second iteration resulted in r = 119 μm and R_o = 121 μm ($\theta_2 = 0.03$) which corresponds to a total $\theta = 0.32$ (eq 2.17). Figure 3.3b shows the simulated response using the dimensions obtained from the first (solid line) and second (dashed line) iteration of the least-square optimization. The second iteration resulted in a good fit with experimental data (O) and suggests that the surface contains an nonuniform distribution of microelectrodes as shown schematically in Figure 2.5.

In order to verify the microelectrode array dimensions obtained using the best fit method just described, the expected response characteristics of an array with the dimensions determined above were calculated. As mentioned in section 1.2, a steady-state response is achieved when the steady-state diffusion layer thickness, δ_{ss} (eq 1.15), is smaller than the diffusion layer thickness, δ (eq 1.9). The ratio of $(\delta/\delta_{ss})^2$ can be used to determine which diffusional mode is expected to dominate the response, and is expressed as dimensionless time, τ (Sleszynski and Osteryoung, 1984),

$$\tau = \frac{16Dt}{\pi r^2} \tag{3.5}$$

If $\tau \gg 1$, a steady-state response will be obtained and if $\tau \ll 1$, a response characteristic of semi-infinite linear diffusion will be observed. When τ is ca. 1, a mixed response is obtained.

In order to obtain a purely steady-state response at an array of microelectrodes (assuming τ is large),

$$R_o \geq r + \delta_{ss} \tag{3.6}$$

It follows that the range of θ values ($1 > \theta \geq 0.7$) which can result in a purely steady-state response can be estimated by substituting equations 3.6 and 1.15 into equation 1.16. In other

words, a purely steady-state response will only be obtained when there is no significant diffusion layer overlap between adjacent microelectrodes.

On the other hand, in the same range of θ values ($1 > \theta \geq 0.7$), two conditions can exist which will lead to mixed behavior. First, mixed diffusional behavior will occur at short times (i.e., $\tau \approx 1$) where neither δ nor δ_{ss} will dominate the response. Second, at long times partial diffusion layer overlap from adjacent microelectrodes will occur which will also cause mixed behavior. At times in between, a steady-state response should be observed. Complete overlap, which will occur at sufficiently long times, will produce a response characteristic of semi-infinite linear diffusion. For an array with $\theta < 0.7$ there will be no purely steady-state response, but instead, mixed behavior will result from the two diffusional modes.

To verify the dimensions of the microelectrodes determined from the least-square optimization routine (Figure 3.3a), values of δ and τ were determined from equations 1.9 and 3.5, respectively, (Table 3.2). Times (t) were calculated as the time the potential would be maintained past the peak potential in a CV at a particular scan rate. As can be seen in Table 3.2, the values of τ for 10 μm microelectrodes at scan rates less than 500 mV-s^{-1} are much greater than 1 suggesting that steady-state behavior should be observed. Yet, based on values of δ (35-245 μm at scan rates less than 500 mV-s^{-1}) relative to the dimensions of 10 μm microelectrodes, the effects of radial diffusion are overridden by diffusion layer overlap between adjacent microelectrodes. At scan rates greater than 1000 mVs^{-1}, values of δ become small relative to the dimensions of the 10 μm microelectrodes and, therefore, allow the behavior of the individual microelectrodes to be observed. Because the values of τ for 10 μm microelectrodes, at scan rates greater than 1000 mV-s^{-1}, are close to 1, the response should demonstrate mixed behavior.

Table 3.2. Calculated values of diffusion layer thickness and dimensionless time for 10 and 119 μm microelectrodes

ν, mV-s^{-1}	t, s[a]	δ μm[b]	$\tau_{10\mu m}$[c]	$\tau_{119\mu m}$[c]
2	25	245	763	5
5	10	155	305	2
10	5	109	153	1
20	2.5	77	76	0.5
50	1	49	31	0.2
100	0.5	35	15	0.1
500	0.1	15	3	0.02
1000	0.05	11	2	0.01
2000	0.025	8	0.8	0.01
3000	0.017	6	0.5	0.004
5000	0.01	5	0.3	0.002
10000	0.005	3	0.2	0.001

[a] Calculated using t=50(mV)/ν(mV-s^{-1}).
[b] Calculated using equation 1.9.
[c] Calculated using equation 3.5.

The predicted mixed behavior at fast scan rates was confirmed by a plot of log peak current ($i_{p,c}$) versus log scan rate (ν) (Figure 3.4). Under semi-infinite linear diffusion conditions, peak current is proportional to the square root of scan rate, while under steady-state conditions, limiting current becomes independent of scan rate (Sleszynski and Osteryoung, 1984). As can be seen in Figure 3.4, at scan rates less than 500 mV-s^{-1} semi-infinite linear diffusion controls the response which results in a slope of 0.5. At scan rates above 1000 mV-s^{-1}, the peak current becomes less dependent on scan rate. The deviations from semi-infinite linear diffusion behavior, characteristic of mixed behavior, are observed as was predicted for the 10 μm microelectrodes. The good correlation of experimental results with the theoretical predictions for 10 μm microelectrodes indicates that in spite of the good fit (Figure 3.3b) 119 μm microelectrodes may not represent the true dimensions. Nonuniformity of the array may be the sole reason for the good fit obtained for the 119 μm rather than 10 μm microelectrodes.

CC was also used to confirm the results obtained by the least-square optimization routine (Figure 3.3a). As can be seen in Figure 3.5, a transition from semi-infinite linear diffusion to the active area, to the semi-infinite linear diffusion to the geometric area, occurs between approximately 1 and 100 ms. The larger slope at $t < 100$ ms is a result of efficient mass transport to the individual microelectrodes resulting from radial diffusion. These results suggest that diffusion layers from individual microelectrodes do not significantly overlap at times less than 100 ms. Therefore, at times less than 100 ms the behavior of the individual microelectrodes should be observable. This is consistent with the calculated δ values in Table 3.2 and the observed deviations in the log i_p versus log ν plots in Figure 3.4 at scan rates above 500 mV-s^{-1}.

Figure 3.4 Plot of log $i_{p,c}$ versus log ν for 2 mM $Fe(CN)_6^{3-/4-}$/1 M KCl at an unpolished TTF-TCNQ/PVC electrode. Slope of the solid line is 0.5.

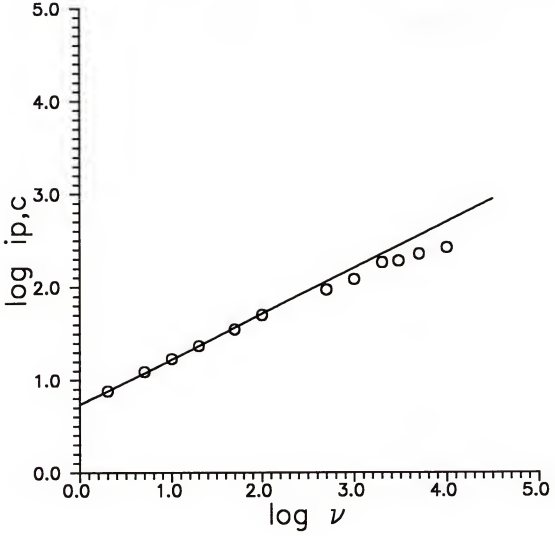
5.0
4.0
3.0
2.0
1.0
0.0
log ip,c
0.0
1.0
2.0
3.0
4.0
5.0
log ν

Figure 3.5 Plot of Q versus $t^{1/2}$ for 2 mM $Fe(CN)_6^{3-/4-}$/1 M KCl at an unpolished TTF-TCNQ/PVC electrode. Potential step +0.400 to 0.000 V versus SCE.

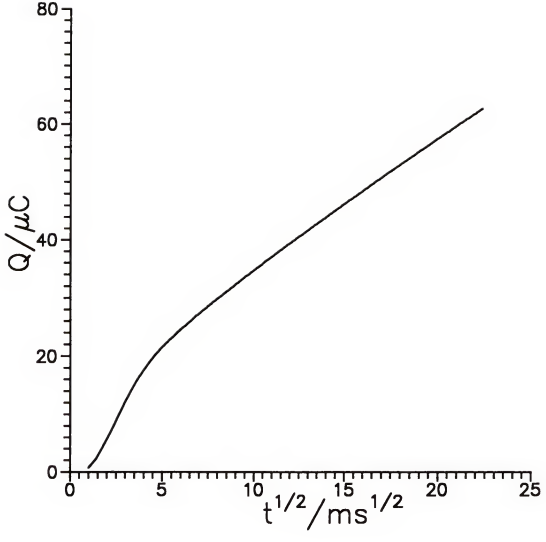
80
60
40
20
0
Q/μC
0
5
10
15
20
25
t^1/2 / ms^1/2

The least-squares optimization routine used to determine the best fit between experimental and simulation CA data, was also used to characterize polished TTF-TCNQ/PVC electrodes. A good fit between experimental and simulated data was obtained after the first iteration of the optimization program, suggesting that there was a fairly uniform distribution of active sites. The values of r and R_o of approximately 0.031 and 0.033 cm, respectively, were the same for the first and second iteration. This result suggests that the surface of polished TTF-TCNQ/PVC electrodes has a large active area separated by small inactive areas. The large r value is inconsistent with the TTF-TCNQ structure as seen in SEM images in section 3.2.4, and must represent dimensions of aggregates of smaller microelectrodes. The behavior of smaller microelectrodes could not be observed by either CA or CC, suggesting that because of the size and density of the small microelectrodes, diffusion layer overlap occurs almost instantaneously (i.e., less than 1 ms). As will be discussed in section 3.2.4, this is confirmed by SEM results.

3.2.4 Verification of Microelectrode Array Structure with Electrochemical Copper Deposition

SEM data obtained following electrochemical copper deposition (conditions described in section 2.3.2.4) were used to confirm the structure of unpolished and polished TTF-TCNQ/PVC polymer paste electrodes predicted by the least-square optimization routine in section 3.2.3. As can be seen from the copper deposition patterns in Figure 3.6a, a model consisting of a nonuniform distribution of microelectrodes, as predicted in section 3.2.3 and similar to that shown schematically in Figure 2.5a, seems reasonable for the TTF-TCNQ/PVC polymer paste electrode. Figure 3.6b shows the increase in density and a more even distribution of microelectrodes at polished TTF-TCNQ/PVC polymer paste electrodes, with small areas of little or no activity. The increase in density and more even distribution of microelectrodes corresponds to a increase in the fraction of active area. The increase in the

Figure 3.6 Scanning electron micrographs of TTF-TCNQ/PVC electrodes after copper deposition at -0.155 V versus SCE in 50 mM $CuSO_4$, 1000X magnification. (a) unpolished; (b) polished. Bar = 10 μm

a)

b)

fraction of active area, resulting from polishing, is as predicted based on SEM data described in section 3.2.2, and agrees with the observed change in reversibility shown in Table 3.1. The time scales used in the CA and CC experiments are too large to resolve the microelectrode response at polished TTF-TCNQ/PVC polymer paste electrodes. This is due to the fact that microelectrode separation, as seen in Figure 3.6b, is less than 1 μm which would result in diffusion layer overlap within tenths of milliseconds, well below the time limitations of instrumentation used in this work. As a result, the microelectrode array dimensions predicted from the best fit method using CA data in section 3.2.3 (r=0.031cm and R_o=0.033 cm), cannot reflect the true array dimensions.

Clearly, TTF-TCNQ electrode surfaces can be approximated by a random microelectrode array structure consisting of localized areas of electroactivity separated by areas of little or no activity. The method of electrode preparation including unpolished polymer paste, polished polymer paste, and high-pressure pellet electrodes, can be used to produce microelectrode arrays with average unit cell dimensions, R_o, ranging form 10 to 0.1 μm.

3.3 Microelectrode Array Structure at Graphite Electrodes

To date there have been many methods described to activate carbon electrodes, including electrochemical treatment, laser irradiation, rf plasma, and heat treatment (McCreery, 1991). These methods have been developed empirically and only now is the understanding of parameters controlling surface activity beginning to emerge (Bowling et al., 1989b; Chang and Bard, 1990). Activation, common to these procedures may be attributable to an increase in the exposed edge plane density which has been associated with faster kinetics (Bowling et al., 1989a; Bowling et al., 1989b). Copper deposition in conjunction with

scanning electron microscopy (SEM) has shown an increase in the density of active sites (Bodalbhai and Brajter-Toth, 1990) on active surfaces. Scanning tunneling microscopy (STM), phase detection microscopy and SEM have also been used to study the effects of electrochemical treatment of highly oriented pyrolytic graphite (HOPG) (Gewirth and Bard, 1988) and GC (Wang et al., 1990; Smyrl et al., 1989). These studies have suggested an increase in surface roughness consistent with an increase in the density of exposed edge planes.

The electrochemical oxidation of graphite has been studied extensively (Kinoshita, 1988). At low supporting electrolyte concentrations (less than 1 M) and low graphite crystallinity (as is the case with GC), intercalation efficiency is low (Beck et al., 1981; Maeda et al., 1985). As a result, side reactions including oxidation of water, production of surface oxides and corrosion of the surface become more dominant. Graphite oxide formation has been reported in neutral or acid supporting electrolytes with oxygen-containing anions (Cabaniss et al., 1985; Kepley et al., 1988; Kinoshita, 1988). In contrast, the formation of graphite oxide in supporting electrolytes containing chloride salts is reported to be much less efficient (Kinoshita, 1988). This is a result of the oxidation of chloride which occurs more readily than the oxidation of the electrode surface.

3.3.1 Evidence for Microelectrode Array Structure at Graphite Electrodes

Evidence that activation procedures increase the fraction of active area at graphite electrodes has been presented by Bodalbhai and Brajter-Toth (Bodalbhai and Brajter-Toth, 1990). Their results revealed an increase in the density of localized electroactive sites by decorating electroactive regions on electrode surfaces with electrochemically deposited copper. The fairly uniform distribution of spherical copper deposits (ca. 0.1 μm) was the first

evidence that graphite may have a surface structure which could be approximated by a microelectrode array model.

3.3.2 Electrochemical Characterization of Microelectrode Array Structure

In this work, the least-squares optimization routine described in section 2.4.1, using simulated and experimental CA data to determine the dimensions of a microelectrode array, was utilized to characterize the structure of graphite electrodes. As was the case in section 3.2.3, the best fit method determines the optimal dimensions of r and R_o (see Figure 1.3) for an average unit cell in a microelectrode array based on the best least-square fit between experimental and simulated CA data.

Figure 3.7 shows the results of the best fit method, a plot of $(\Sigma e_i^2)^{-1}$ versus R_o, for untreated GC (——) and ECGC (- - -). Neither untreated GC nor ECGC electrodes showed microelectrode array behavior (i.e. the best fit was obtained with values of R_o corresponding to the geometric area), suggesting that there is a uniform distribution of microelectrodes with dimensions too small to be resolved by the CA experiment. This is reasonable based on copper deposition data described in section 3.3.1 which reported distances between active sites of ca. 1μm (Bodalbhai and Brajter-Toth, 1990). A microelectrode array with these dimensions would result in diffusion layer overlap on a submillisecond time scale which is well below the accessible time scales of CA and CC experiments (100 and 1 ms, respectively) in this study.

3.3.3 Characterization of Graphite Surface Structure with Scanning Tunneling and Atomic Force Microscopy

In order to further investigate the sources of activity at graphite electrodes, STM and AFM were used to characterize graphite surfaces. STM and AFM are used as complimentary techniques to differentiate between electronic and topographical changes at the electrode surface. As discussed in section 3.3, the activity of graphite electrodes has been shown to

Figure 3.7 Plot of $(\Sigma e_i^2)^{-1}$ versus R_o for (——) untreated GC and (- - -) ECGC electrode after background subtraction. Experimental conditions are the same as those in Figure 3.3.

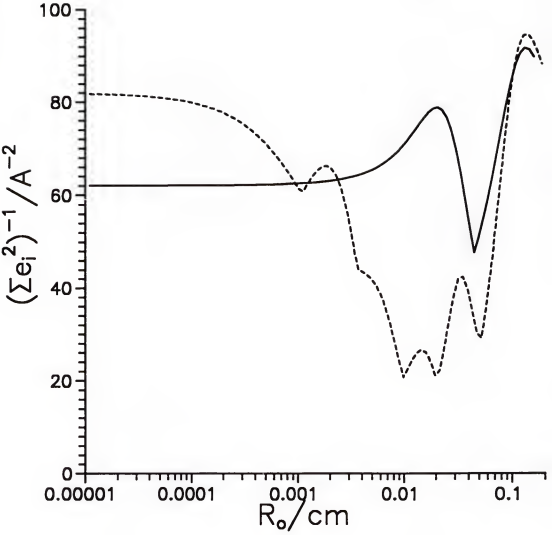
100
80
60
40
20
0
$(\Sigma e_i^2)^{-1}/A^{-2}$
0.00001
0.0001
0.001
0.01
0.1
R_o/cm

correlate with exposed edge plane (McCreery, 1991). In light of the increase in the density of localized areas of electroactivity at ECGC electrodes (Bodalbhai and Brajter-Toth, 1990), STM and AFM were expected to reveal localized structural changes consistent with copper deposition patterns.

In addition to increasing electroactivity as mentioned in section 3.3, electrochemical treatment of GC and HOPG results in the formation of an oxide layer (Cabaniss et al., 1985 Kepley et al., 1988; Gewirth and Bard, 1988). The amorphous nature of graphite oxide and its uneven distribution over the electrode surface (Gewirth and Bard, 1988) may result in an electronically inhomogeneous surface. In a case where a surface is electronically inhomogeneous, changes in tunneling current can be a result of changes in topography and/or in local electronic structure (Binnig and Rohrer, 1986). As a result STM images may provide misleading information about the topography.

AFM has been shown to be effective in studies of the topography of both conducting and insulating surfaces because it does not require the sample to be conducting (Binnig et al., 1986; Albrecht and Quate, 1987). As a result, AFM should not be affected by local changes in electronic structure. For this reason, AFM was used in conjunction with STM to study the effect of electrooxidative activation of GC.

Figure 3.8 shows representative STM and AFM images of an untreated GC electrode surface (polished with 5, 0.3 and finally 0.05 μm alumina as described in section 2.3.1.3) obtained in a constant current and constant displacement mode, respectively. In a constant signal mode the STM or AFM maintains a constant signal (either tunneling current or cantilever displacement, respectively) by moving a tip vertically with a calibrated piezoelectric element while rastering across the surface. This results in a topographical image based on the potential applied to the piezoelectric element in order to maintain a constant signal. Under

Figure 3.8 (a) Constant current STM image (tip bias +100 mV, tunneling current 2 nA) and (b) constant cantilever displacement AFM image (100 μm Si_3N_4 triangular cantilever, spring constant 0.58 N/m) of polished GC in air. XYZ axis in nm.

a)
b)
400
300
200
100
0
100
200
300
400
5.0
0

these conditions the observed topography obtained with STM and AFM is similar for the untreated GC surface. Large defects (ca. 2 μm diameter), which are a result of gas pockets formed during the fabrication process, were also observed (not shown), although their density is low (Bodalbhai and Brajter-Toth, 1990).

Supporting electrolytes consisting of 0.1 M KNO_3, NaH_2PO_4/Na_2HPO_4, H_2SO_4 and KCl were chosen to determine the effect of electrochemical treatment (treatment conditions described in section 2.3.1.3) on the surface structure of GC. Figure 3.9 shows the effect of electrochemical activation of GC in 0.1 M KNO_3, a common supporting electrolyte used for graphite activation (Engstrom and Strasser, 1984; Bowling et al., 1989b). As can be seen in the STM image (Figure 3.9a), there is a significant change in the apparent surface roughness as a result of electrochemical treatment compared to the polished electrode (Figure 3.8a). The surface roughness apparent in Figure 3.9a is attributed to the presence of graphite oxide resulting in topographical and electronic changes at the surface. The surface roughness shown in Figure 3.9a is not as pronounced as that reported elsewhere (Wang et al., 1990). This is most likely due to a lower anodic overpotential used during treatment.

In contrast to the surface roughness apparent in STM images (Figure 3.9a), AFM images (Figure 3.9b) reveal a relatively smooth surface with isolated defects with diameters on the order of 100 nm. Similar isolated defects, as shown in Figure 3.9b, were observed at different positions on the electrode surface. Usually, at least one defect was observed in any given 500 X 500 nm field. Figure 3.10 shows a typical defect at higher magnification. It should be noted that larger, irregular shaped defects, grooves and much larger gas pockets were also observed, however not nearly as often (Figure 3.11). Both the observation of small localized defects as well as irregular shaped defects and grooves are consistent with copper deposition patterns observed with SEM on electrochemically treated GC electrodes where

Figure 3.9 (a) Constant current STM image (tip bias +100 mV, tunneling current 2 nA) and (b) constant cantilever displacement AFM image (100 μm Si_3N_4 triangular cantilever, spring constant 0.58 N/m) of GC in air following electrochemical treatment in 0.1 M KNO_3. XYZ axis in nm.

a)
b)
400
300
200
100
0
100
200
300
400
5.0

Figure 3.10 Constant cantilever displacement AFM image (100 μm Si_3N_4 triangular cantilever, spring constant 0.58 N/m) of GC in air showing typical defect formed as a result of electrochemical treatment in 0.1 M KNO_3. XYZ axis in nm.

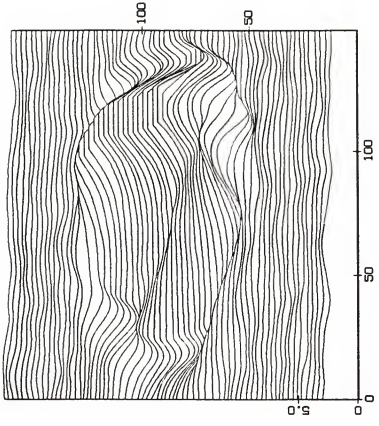
100
50
0
50
100
0
5.0

Figure 3.11 Constant cantilever displacement AFM image (100 μm Si_3N_4 triangular cantilever, spring constant 0.58 N/m) GC in air following electrochemical treatment in 0.1 M KNO_3, showing (a) grooves and (b) irregular shaped defects. XYZ axis in nm.

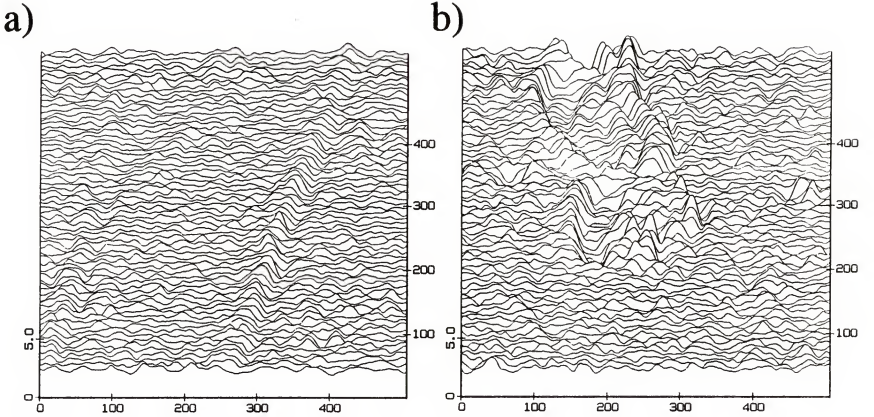
a)
b)
0
5.0
100
200
300
400

copper nuclei with diameters on the order of 100 nm were separated by distances between 100 and 1000 nm and where such grooves were also observed (Bodalbhai and Brajter-Toth, 1990). It has been suggested that a compacted microparticle layer is formed as a result of electrode polishing and that this layer is responsible for the less active nature of polished GC (Bodalbhai and Brajter-Toth, 1990; Kazee et al., 1985). It is, therefore, possible that defect formation occurs at pinholes present in the compacted layer.

Clearly, the topography of untreated GC determined by both STM and AFM is similar, as seen in Figure 3.8. At this point however it is not clear whether STM or AFM images represent true topography for ECGC. There are two possible explanations of the differences in surface roughness of ECGC determined by STM and AFM (see Figure 3.9). The first possibility is that the structure observed in AFM images (Figure 3.9b) lies beneath a nonuniform, porous, graphite oxide layer which is wiped away the first time the cantilever is rasterred across the surface in AFM measurements. The second possibility is that the roughness shown in STM images (Figure 3.9a) is associated with the contours of the conducting vitreous carbon surface below a nonuniform graphite oxide layer, and that the true topography of the electrode surface, as represented by AFM images, is smooth and contains surface defects exposing active graphite. In either case, the agreement between AFM images and copper deposits suggest that the localized defects represent active regions either at the electrode surface or just beneath a porous oxide layer.

Although it is not clear what mechanism controls the formation, size and distribution of the observed defects, these defects may ultimately control the electrode activity. Defects of similar diameter and shape have also been observed with STM on HOPG as a result of gasification reactions which result in the oxidation of graphite (Chang and Bard, 1990). The uniformity of the size and shape of the defects produced by gasification has been explained by

the presence of atomic defects (i.e. edge sites) at which the oxidation rate is significantly faster (Chang and Bard, 1990). Defects produced by different methods of oxidation (including gasification and electrooxidation) may form by the same mechanism.

Results similar to those at GC electrodes electrochemically treated in KNO_3 were obtained in phosphate buffer (pH 7) and H_2SO_4. In both cases, STM images showed an increase in apparent surface roughness as a result of treatment, while AFM images showed circular defects similar to those shown in Figure 3.9b and 3.10. Treatment in KCl did not increase apparent surface roughness as imaged by STM. This is consistent with the fact that the oxidation of chloride (Beck et al., 1981) is the dominant anodic reaction, thereby decreasing the amount of oxide formation during treatment. Although defects were observed after electrochemical treatment in KCl, they were not as prevalent as on surfaces treated in the other supporting electrolytes.

3.4 Conclusions

The results reported in this chapter demonstrate that both TTF-TCNQ and graphite electrode surface structures can be approximated by a random microelectrode array where localized areas of electroactivity are separated by relatively inactive regions. It is clear that for both TTF-TCNQ and graphite electrodes, the method of electrode preparation controls the dimensions of microelectrode arrays, where unit cell diameters can range from 10 to 0.1 μm. In addition, the activity of these electrodes correlates with the fraction of active area determined by the microelectrode array dimensions, as predicted by theory.

The case of TTF-TCNQ/PVC unpolished polymer paste electrodes demonstrates that transitions in CA response at microelectrode arrays from responses characteristic of the active area to responses characteristic of total geometric area, can be used to determine the

dimensions of the microelectrode array. By determining the best fit between experimental and simulated CA data, the dimension of the microelectrode array can be determined. The fitting of experimental and simulated CA data to determine the dimensions of microelectrode arrays is a fast nondestructive technique for the characterization of electrode surfaces.

Electrochemical treatment of GC in supporting electrolytes, with the exception of KCl, to form ECGC results in an inhomogeneous surface (compared to polished electrodes) which is apparent from the changes in the topography determined by both STM and AFM. However, significant differences in the observed topography by STM and AFM for ECGC suggest that the surface oxides produced during electrochemical activation, affect STM and AFM images differently. Although it is not clear which technique produces images representative of true topography, images obtained with AFM reflect a surface structure consistent with the structure observed when electroactive sites are imaged by electrochemically formed copper deposits. The identification of localized defects at the surface of ECGC, and the correlation of their size and density with the distribution of copper deposits, suggests that these defects may be a source of exposed edge plane, where electron transfer is several orders of magnitude faster than in other regions.

CHAPTER 4
ROLE OF SURFACE/SUBSTRATE INTERACTIONS IN THE RESPONSE OF ELECTRODES

4.1 Theory

As discussed in section 1.3, there are several factors which can affect redox reaction kinetics including electrocatalysis and adsorption. In many cases, redox reactions involve the transfer of multiple electrons and include chemical steps. Since the time scale of electron transfer ($\sim 10^{-16}$ s) is significantly faster than chemical ($\sim 10^{-14}$ s) and solvent ($\sim 10^{-12}$ s) reorganization, the probability of multiple electron transfer occurring in a single step is low (Weaver, 1987; Calvo, 1986). This is because it is easier to overcome two smaller activation barriers than a single large one. As a result, complex redox reactions occur through sequential or parallel pathways involving elementary electron transfer and chemical steps.

In order to understand the role of surface/substrate interactions in redox reactions, it is important to be able to determine the mechanism of electron transfer by breaking down complex electrode reactions into their elementary steps, to characterize each step, and to determine the rate-determining step (RDS). The ability to change the rate of a heterogeneous electron transfer reaction by changing the potential at the working electrode can be used to determine the mechanism of electron transfer by characterizing elementary electron transfer and chemical steps in a complex redox reaction. As discussed in section 1.1, transfer coefficient values, α, will be dependent on the reaction mechanism for multiple step processes (Bockris and Nagy, 1973), and values of α can be determined from the dependence of the

observed rate coefficient on potential (eqs 1.7 and 1.8). In the next two sections, the dependence of α on reaction mechanism will be discussed in detail for redox reactions involving multiple electron transfers and chemical steps and mediated electron transfer.

4.1.1 Multiple Step Electron Transfer Reactions

If one considers a sequential, two electron, redox reaction,

$$Ox + e^- \underset{k_{-1}}{\overset{k_1}{\rightleftharpoons}} I + e^- \underset{k_{-2}}{\overset{k_2}{\rightleftharpoons}} Red \tag{4.1}$$

where I is an electroactive intermediate, an overall kinetic equation for reaction 4.1 can be determined by the steady-state method (Conway, 1965). Under steady-state conditions the concentration of the intermediate remains constant, and therefore the change of the intermediate concentration with respect to time is zero,

$$\frac{dI}{dt} = k_1[Ox] - k_{-1}[I] - k_2[I] + k_{-2}[Red] = 0 \tag{4.2}$$

where rate coefficients for the elementary electron transfer reactions are described by

$$k_i = k_i^\circ \exp^{\frac{-\beta F}{RT}(E - E^{\circ\prime})} \tag{4.3}$$

and

$$k_{-i} = k_i^\circ \exp^{\frac{(1-\beta)F}{RT}(E - E^{\circ\prime})} \tag{4.4}$$

where β_i is the symmetry factor (assumed to be 0.5) and k_i° is the standard heterogeneous electron transfer rate constant for the elementary step. Equation 4.2 can in turn be used to express the intermediate concentration in terms of Ox and Red,

$$[I] = \frac{k_1[Ox] + k_{-2}[Red]}{k_{-1} + k_2} \tag{4.5}$$

The overall rate of reaction 4.1 can be expressed as

$$-\frac{d[Ox]}{dt} = k_1[Ox] - k_{-1}[I] \tag{4.6}$$

Substituting equation 4.5 into 4.6 yields

$$-\frac{d[Ox]}{dt} = \frac{k_1 k_2}{k_{-1} + k_2}[Ox] - \frac{k_{-1}k_{-2}}{K_{-1} + k_2}[Red] \tag{4.7}$$

where the apparent forward rate coefficient for reaction 4.1 is

$$k_f = \frac{k_1 k_2}{k_{-1} + k_2} \tag{4.8}$$

and the reverse apparent rate coefficient is

$$k_b = \frac{k_{-1}k_{-2}}{k_{-1} + k_2} \tag{4.9}$$

Under these conditions, a plot of ln k_f versus E (see eq 1.7) will result in a slope of $-\alpha nF/RT$ and a plot of ln k_b versus E (see eq 1.8) will result in a slope of $(1-\alpha)nF/RT$, where α and $(1-\alpha)$ are cathodic and anodic transfer coefficients, respectively. Values of αn and $(1-\alpha)n$ will depend on the relative magnitudes of the individual elementary rate coefficients (eqs 4.3 and 4.4) in k_f and k_b (eqs 4.8 and 4.9).

Assuming the intermediate is less stable than the reactant or the product (i.e. $k_1/k_{-1} < k_2/k_{-2}$), two limiting cases are possible (i.e. the first or second electron transfer can be rate determining).

When the first electron transfer step is rate determining (i.e. $k_2 \gg k_{-1}$), the dependance of k_f and k_b on potential can be expressed as

$$k_f = k_1 = k_1^\circ \exp^{\frac{-0.5F}{RT}(E-E^{\circ\prime})} \tag{4.10}$$

and

$$k_b = \frac{k_{-1}k_{-2}}{k_2} = \frac{k_{-1}^\circ k_{-2}^\circ}{k_2^\circ} \exp^{\frac{1.5F}{RT}(E-E^{\circ\prime})} \tag{4.11}$$

where k_i° is the standard heterogeneous rate constant for the elementary electron transfer steps as defined in equations 4.3 and 4.4. Based on equations 4.10 and 4.11, a plot of ln k_f versus E will result in an αn value of -0.5 and a plot of ln k_b versus E will result in a $(1-\alpha)n$ value of 1.5.

When the second electron transfer step is rate determining (i.e. $k_2 \ll k_{-1}$), the dependance of k_f and k_b on potential can be expressed as

$$k_f = \frac{k_1 k_2}{k_{-1}} = \frac{k_1^\circ k_2^\circ}{k_{-1}^\circ} \exp^{\frac{-1.5F}{RT}(E-E^{\circ\prime})} \tag{4.12}$$

and

$$k_b = k_{-2} = k_{-2}^\circ \exp^{\frac{0.5F}{RT}(E-E^{\circ\prime})} \tag{4.13}$$

A plot of ln k_f versus E will result in an αn value of -1.5 and a plot of ln k_b versus E will result in a $(1-\alpha)n$ value of 0.5.

Bockris and Nagy have published a simple equation for predicting the transfer coefficient for a consecutive multi-step electrode reaction containing a rate-determining step (Bockris and Nagy, 1973). The general form of the overall multi-step electrode reaction is given by

$$A + ne^- \rightleftharpoons Z \tag{4.14}$$

with a rate-determining step

$$O + re^- \rightleftharpoons P \tag{4.15}$$

involving r electrons (r=0 if rate-determining step is a chemical step, and r=1 if an electron transfer is the rate-determining step). If reaction 4.15 occurs v times, s is the number of electrons transferred before the rate-determining step, and s' is the number of electrons transferred after the rate-determining step, then n=s+rv+s'. The general expression for αn is given by

$$\alpha n = \frac{n-s}{v} - r\beta \tag{4.16}$$

where β is the symmetry factor (assumed to be 0.5), and the expression for $(1-\alpha)n$ is given by

$$(1-\alpha)n = \frac{s}{v} + r\beta \tag{4.17}$$

Table 4.1 shows expected transfer coefficients for a consecutive electrode reaction involving an electron transfer, a chemical step, another electron transfer, followed by a second chemical step (ECEC). Values of transfer coefficient determined when the first and second electron transfer are rate determining are in agreement with those derived for a consecutive two-electron transfer derived earlier in this section (eqs 4.10-4.13).

4.1.2 Mediated Electron Transfer Reactions

In a mediated electron transfer reaction (see Figures 1.6 and 1.7) as shown below

Table 4.1. Predicted transfer coefficients for a consecutive four step (ECEC) electrode reaction with different rate-determining steps.

reaction sequence	n	s	r	v	s'	αn	$(1-\alpha)n$
ECEC	2	0	1	1	1	1.5	0.5
E**C**EC	2	1	0	1	1	1	1
EC**E**C	2	1	1	1	0	0.5	1.5
ECE**C**	2	2	0	1	0	0	2

E - electron transfer step.
C - chemical step.
Bold type face represents RDS
n - total number of electrons transferred
s - number of electrons transferred before RDS
r - number of electrons transferred in RDS (r=0 for no electrons transferred in RDS)
v - number of times the RDS occurs in overall reaction
s'- number of electrons transferred after RDS

$$Ox + B \underset{k_{-1}}{\overset{k_1}{\rightleftharpoons}} A + Red \tag{4.18}$$

$$A + e^- \underset{k_{-2}}{\overset{k_2}{\rightleftharpoons}} B \tag{4.19}$$

where k_1 and k_{-1} are second order rate constants, and k_2 and k_{-2} are potential dependent heterogeneous electron transfer coefficients (eq 4.3 and 4.4), steady-state conditions require the concentration of the intermediate be constant, and therefore that the change of the intermediate concentration with respect to time be zero. For the mediated reduction of Ox to Red (Figure 1.7a), the intermediate will be A and therefore, steady-state conditions require

$$\frac{dA}{dt} = k_1[Ox][B] - k_{-1}[A][Red] - k_2[A] + k_{-2}[B] = 0 \tag{4.20}$$

The observed rate (or current, eq 1.6) will result from reaction 4.19,

$$\frac{i}{nFA} = v_{net} = k_2[A] - k_{-2}[B] \tag{4.21}$$

Based on the steady-state assumption (eq 4.20)

$$k_2[A] - k_{-2}[B] = k_1[Ox][B] - k_{-1}[A][Red] \tag{4.22}$$

equation 4.21 can in turn be expressed as

$$\frac{i}{nFA} = v_{net} = \sqrt{(k_2[A] - k_{-2}[B])(k_1[Ox][B] - k_{-1}[A][Red])} \tag{4.23}$$

Under conditions were reaction 4.18 lies far to the right ($k_1 \gg k_{-1}$), and when the applied potential is such that reaction 4.19 lies far to the right ($k_2 \gg k_{-2}$), equation 4.23 can be reduced to

$$\frac{i}{nFA} = \nu_{net} = \sqrt{k_1 k_2 [Ox][A][B]} \tag{4.24}$$

where the reaction will be 1/2 order with respect to the reactant (i.e. Ox) and the forward heterogeneous rate coefficient (i.e. the apparent heterogeneous rate coefficient for the reduction) can be expressed as

$$k_f = \sqrt{k_1 k_2} = \sqrt{k_1 k_2^\circ} \exp^{\frac{-0.25F}{RT}(E-E^{\circ\prime})} \tag{4.25}$$

where k_2° is the standard heterogeneous rate constant for the elementary electron transfer reaction (eq 4.19) defined by equation 4.3, and k_1 is the second order forward rate constant for reaction 4.18. A plot of ln k_f versus E at potentials sufficiently negative of $E^{\circ\prime}$ for the A/B redox couple (i.e. potentials where $k_2 \gg k_{-2}$) will result in an αn value of -0.25 as predicted by equation 4.25. The same approach can be used to derive an apparent rate coefficient for the reverse reaction ($k_1 \ll k_{-1}$ and $k_2 \ll k_{-2}$) (Figure 1.6b), which results in

$$k_b = \sqrt{k_{-1} k_{-2}} = \sqrt{k_{-1} k_{-2}^\circ} \exp^{\frac{0.25F}{RT}(E-E^{\circ\prime})} \tag{4.26}$$

and therefore a plot of ln k_b versus E, at potentials sufficiently positive of $E^{\circ\prime}$ for the A/B redox couple (i.e. potentials where $k_2 \ll k_{-2}$) will result in an $(1-\alpha)n$ value of 0.25.

4.1.3 Adsorption at Electrode Surfaces

Adsorption at electrodes can be divided into four limiting cases: (i) purely electrostatic adsorption, (ii) specific ionic adsorption, (iii) adsorption of uncharged species and (iv) chemisorption (Parsons, 1980). The first three cases can be considered as adsorption without the formation of a chemical bond (i.e. physisorption), whereas the fourth case, chemisorption, involves the formation of a chemical bond. Purely electrostatic adsorption is a result of ions attracted by the charge on the electrode surface. In this type of adsorption, there is no

intimate contact between the surface and the adsorbing ions, instead, the solvated ions are attracted to the electrode surface, forming a space charge layer. Specific ionic adsorption, on the other hand, is defined as adsorption of ions not accounted for by purely electrostatic adsorption. It includes short range forces and is confined to a monolayer in intimate contact with the electrode surface. Finally, adsorption of uncharged species involves the replacement of solvent at the electrode surface without the formation of a chemical bond, whereas chemisorption is the adsorption of species resulting in the formation of a chemical bond.

As discussed in section 1.3, adsorption can affect the observed electron transfer rate, or observed current. This results from changes in the free energy of activation for electron transfer, $\Delta G^{\ddagger}$ (see Figure 1.5) resulting form adsorption, which will in turn change the electron transfer rate coefficient (eq 1.3). In addition, under conditions where the surface concentration is a result of diffusing and adsorbed species, and where the thermodynamics of the electron transfer reaction, ΔG^{o} (see Figure 1.5) are not affected by adsorption, adsorption will result in an increased surface concentration (i.e. surface excess, Γ), thereby increasing the observed current or rate (eq 1.6).

4.2 Surface Chemistry of TTF-TCNQ Electrodes

Recent reports have shown that the quasi-one-dimensional organic metal tetrathiafulvalene-tetracyanoquinodimethane (TTF-TCNQ) can be used as an electrode material for the electrocatalytic oxidation of β-NADH (Albery and Bartlett, 1984) and flavoenzymes (McKenna and Brajter-Toth, 1987; Albery et al., 1985; Cenas and Kulys, 1981; Albery et al., 1986; Albery et al., 1987; Kulys et al., 1981; Hale and Wightman, 1988; Hill et al., 1988). Although the properties of this electrode material have been investigated actively, the mechanism of electrocatalysis is not understood (Albery et al., 1985; Albery et al., 1987;

Jaeger and Bard, 1979; McKenna et al., 1988). Mechanisms involving homogeneous mediation by small amounts of dissolved electrode material have been proposed, where TTF^+ or $TCNQ^-$ mediate electron transfer (Cenas and Kulys, 1981; Albery et al., 1987; Hale and Slotheim, 1989). A heterogeneous retro-charge-transfer mechanism, where electron transfer occurs via surface bound $TCNQ^o$ produced by dissociation of TTF-TCNQ on the electrode surface, has also been proposed (Albery et al., 1987). The actual mechanism of electron transfer is still the topic of debate.

The purpose of this work was to elucidate the mechanism of electrocatalysis at TTF-TCNQ electrodes. In order to determine the role of the electrode surface in the catalytic oxidation of small biological molecules, a QCM has been used to measure *in situ* mass changes occurring at the electrode/solution interface during electrochemical measurements.

In order to further investigate the mechanism of electron transfer, kinetic data has been obtained from RDE experiments. These experiments result in the heterogeneous rate coefficient as a function of potential (see section 2.3.2.2) from which the apparent transfer coefficient can be determined. As described in sections 4.1.1 and 4.1.2, the apparent transfer coefficient reflects the mechanism of electron transfer, and can therefore be used as a diagnostic tool.

The apparent transfer coefficient and the QCM results suggest that surface bound $TCNQ^o$ may be involved in the mediation. Chemical oxidation of several small biological molecules by $TCNQ^o$ also demonstrates that $TCNQ^o$ can act as an effective mediator. The consistently low values for anodic transfer coefficients (α) determined for small biological molecules from kinetic measurements, suggest that the mechanism involves heterogenous redox catalysis (Albery et al., 1987). A different mechanism from those proposed previously

(Albery et al., 1985; Albery et al., 1987) is proposed here which is consistent with the observed electrode kinetics and mass fluctuations.

4.2.1 Stability of TTF-TCNQ Electrodes Under Electrochemical Conditions

Previous reports have demonstrated that pressed TTF-TCNQ pellet electrodes are stable in H_2O between -0.2 and +0.6 V, the actual range depending upon the supporting electrolyte (Jaeger and Bard, 1979; Jaeger and Bard, 1980). For example, a TTF-TCNQ pressed pellet electrode oxidizes at about +0.65 V in 1 M potassium acetate, resulting in the formation of $TCNQ^o$ (s) and TTF^{2+}(aq) (Jaeger and Bard, 1979). Subsequent reduction at +0.04 V results in the formation of an insoluble KTCNQ salt on the electrode surface. Therefore, oxidation of TTF-TCNQ must result in a net mass loss and a $TCNQ^o$ rich surface. CV has been used to study redox behavior of KTCNQ formed at TTF-TCNQ electrodes in the presence of potassium acetate (Jaeger and Bard, 1979). Oxidation of KTCNQ,

$$KTCNQ(s) \rightarrow TCNQ^0(s) + K^+(aq) + e^- \tag{4.27}$$

has been shown to occur at +0.29 V, and the reduction,

$$TCNQ^0(s) + K^+(aq) + e^- \rightarrow KTCNQ(s) \tag{4.28}$$

at 0.04 V.

In order to determine the redox reactions of TTF-TCNQ in sodium phosphate buffer (pH 7), which have not been reported and which was used as electrolyte in these measurements as well as in the measurements reported previously for glucose oxidase (Albery et al., 1987), CV of each salt component was investigated individually. TTF^o and $TCNQ^o$ were sublimed onto gold electrodes on one side of a QCM at a pressure of 10^{-5} Torr until the film became visible and an observable frequency shift, corresponding to a mass gain due to the deposition of either TTF^0 or $TCNQ^0$, was measured. Each electrode was cycled in a CV

experiment at 20 $mV\text{-}s^{-1}$ between -0.05 and +0.40 V in 0.5 M phosphate buffer to determine the solubility of the individual salt components under typical electrochemical conditions. CV data demonstrated that TTF^0 was oxidized,

$$TTF^0(s) \rightarrow TTF^+(aq) + e^- \tag{4.29}$$

at +0.29 V and TTF^+ was reduced at +0.12 V. The anodic peak current, due to reaction 4.29, decreased by ca. 95% after ten scans due to the dissolution of TTF^+.

Under the same conditions, CV data showed the reduction of $TCNQ^0$,

$$TCNQ^0(s) + Na^+(aq) + e^- \rightarrow NaTCNQ(s) \tag{4.30}$$

at -0.02 V. Oxidation,

$$NaTCNQ(s) \rightarrow TCNQ^0(s) + Na^+(aq) + e^- \tag{4.31}$$

occurred at +0.27 V. The cathodic peak current associated with reaction 4.30 remained relatively stable for ten scans suggesting that both $TCNQ^0$ and NaTCNQ are insoluble. The behavior is similar to that described above for potassium acetate (Jaeger and Bard, 1979), and indicates that loss of TTF^+ from the surface will occur at potentials above +0.11 V in sodium phosphate buffer. In order to determine the magnitude of the mass changes associated with the redox processes for TTF-TCNQ/PVC composite electrodes, QCM measurements were carried out.

Poising a TTF-TCNQ/PVC spin coated electrode at a potential of +0.225 V in 0.5 M phosphate buffer resulted in a 180 Hz frequency increase (mass loss, see eq 2.10) over a period of 1000 seconds, which the above results strongly suggest is due to oxidation of TTF-TCNQ and loss of TTF^+,

$$TTF\text{-}TCNQ(s) \rightarrow TTF^{+}(aq) + TCNQ^{0}(s) + e^{-} \qquad (4.32)$$

This corresponds to a net mass loss of 540 ng or 9.5 X 10^{-9} mol/cm^2 of TTF using the piezoelectrically active area.

As shown in section 2.3.1.4, SEM micrographs of electrochemically deposited copper at spin coated TTF-TCNQ/PVC electrodes reveal a random microelectrode array. Based on an estimated site density of 10^5 sites/cm^2 (Figure 2.2), and an average projected area of the Cu^0 deposits of 1 X 10^{-6} cm^2 suggest that the fraction of electroactive area ($1\text{-}\theta$) is 0.1. From the estimated fraction of electroactive area ($1\text{-}\theta = 0.1$), this frequency shift corresponds to a thick TCNQ layer forming on the surface, approaching 1500 Å. Subsequent CV in 0.5 M phosphate buffer (pH 7) verified the presence of $TCNQ^0$ by the appearance of a reduction peak corresponding to reaction 4.30 (i_p approximately 75 nA).

Mass loss due to the dissolution of TTF^+ and the resulting accumulation of $TCNQ^0$ on the surface was corroborated by experiments in which individual TTF-TCNQ/PVC films spin coated on quartz crystals were exposed to different, constant, potentials over a period of several minutes. Figure 4.1 reveals that mass losses (frequency increases) are more significant at more anodic potentials where the oxidation of TTF-TCNQ (eq 4.32) occurs more rapidly. Mass gains (frequency decreases) observed at potentials $\leq$ -0.05 V are attributed to the reduction of TTF-TCNQ followed by the incorporation of Na^+,

$$TTF\text{-}TCNQ(s) + Na^{+}(aq) + e^{-} \rightarrow TTF^{0}(s) + NaTCNQ(s) \qquad (4.33)$$

in agreement with reaction 4.30. Figure 4.2 shows the resulting frequency changes during repetitive cycling between -0.05 and +0.40 V (0.00 to +0.45 V versus Ag/AgCl) at 5 and 20 mV-s^{-1} at a spin coated TTF-TCNQ/PVC electrode, where one complete cycle (versus Ag/AgCl) is indicated in the figure. Although CV did not show peaks that would be

Figure 4.1 Frequency change as a function of time of a TTF-TCNQ/PVC spin coated electrode in 0.5 M phosphate buffer, pH 7; (a) at open circuit; (b) +0.55; (c) +0.45; (d) +0.25; (e) -0.05; (f) -0.15 V versus Ag/AgCl. The Electrode was held initially at open circuit potential for 60 s to establish frequency stability. Reaction inlays account for observed mass changes.

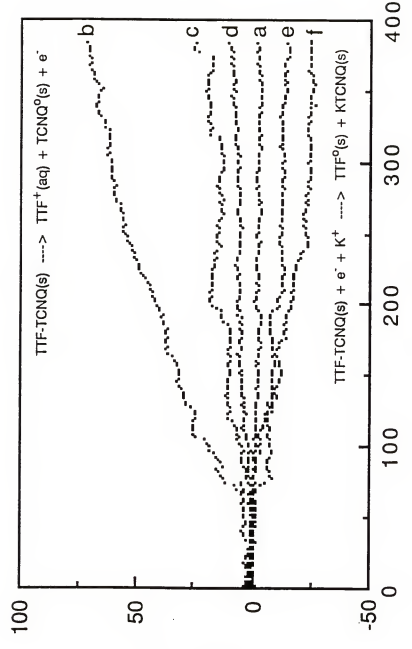
TTF-TCNQ(s) ----> TTF+(aq) + TCNQ0(s) + e-
TTF-TCNQ(s) + e- + K+ ----> TTF0(s) + KTCNQ(s)
b
c
d
a
e
f
100
50
0
-50
0
100
200
300
400
Δf / Hz
t / s

Figure 4.2 Frequency change as a function of time of a TTF-TCNQ/PVC spin coated electrode in 0.5 M phosphate buffer, pH 7; (a) 5 $mV\text{-}s^{-1}$; (b) 20 $mV\text{-}s^{-1}$. Bracket signifies one full cycle between 0.000 and +0.450 V (versus Ag/AgCl). The Electrode was held initially at open circuit potential for 60 s to establish frequency stability.

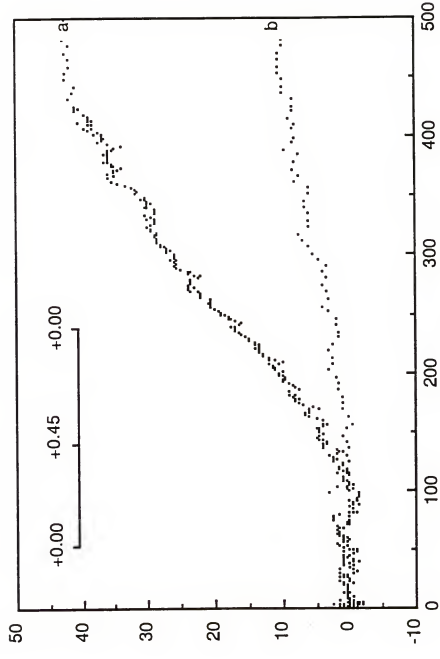
Δf (Hz)
50
40
30
20
10
0
-10
0
100
200
300
400
500
time (sec)
a
b
+0.00
+0.45
+0.00
+0.00

indicative of reactions 4.29 and 4.33, probably because of low sensitivity at this scan rate, the net mass decrease is observed by more sensitive QCM. It is evident from these results that oxidation of the TTF-TCNQ/PVC at anodic potentials results in TTF^+ loss and a $TCNQ^o$ rich surface (eq 4.32).

TTF-TCNQ/PVC electrodes used by McKenna and coworkers for electrocatalytic oxidation of biological molecules were treated by holding the electrode at a constant potential of +0.225 V until background currents decreased to an acceptable value (McKenna et al., 1988). The QCM results presented herein indicate that such treatment results in TTF-TCNQ oxidation (eq 4.32) with a loss of TTF^+ from the electrode, resulting in a $TCNQ^0$ rich surface.

4.2.2 Mechanism of Electron Transfer at TTF-TCNQ Electrodes

Electrochemical behavior of ferri/ferrocyanide couple at TTF-TCNQ/PVC polymer paste electrodes was investigated to characterize the electrode behavior for a simple one-electron transfer redox reaction. In this study, CV and RDE measurements were carried out to determine kinetic parameters associated with the one-electron reduction of $Fe(CN)_6^{3-/4-}$ at TTF-TCNQ electrodes. Typical current-potential curves from an RDE experiment at a TTF-TCNQ/PVC polymer paste electrode are shown in Figure 4.3 at several rotation rates. The resulting Levich plots (i versus $\omega^{1/2}$) are shown in Figure 4.4, and Koutecky-Levich plots of i^{-1} versus $\omega^{-1/2}$ (eq 2.3) are shown in Figure 4.5.

The data in Figure 4.5 were analyzed using the electrode area of 0.292 cm^2 determined by CC. From the slope of the Koutecky-Levich plot, the diffusion coefficient of ferricyanide was determined as $(5.4 \pm 0.9) \times 10^{-6}$ cm^2/s (eq 2.3) which is in reasonable agreement with the reported value of $(7.6 \pm 0.3) \times 10^{-6}$ cm^2/s (Gerhardt and Adams, 1982). The difference in the diffusion coefficients is attributed to the deviations in the Koutecky-

Figure 4.3 Current-potential curves for the reduction of 15 mM $Fe(CN)_6^{3-}$ in 1 M KNO_3, at a rotating disk TTF-TCNQ/PVC electrode as a function of electrode rotation rate. Electrode rotation rates, rpm: (a) 4000; (b) 3000; (c) 2000; (d) 1000; (e) 700; (f) 500; (g) 100. Scan rate 5 $mV\text{-}s^{-1}$.

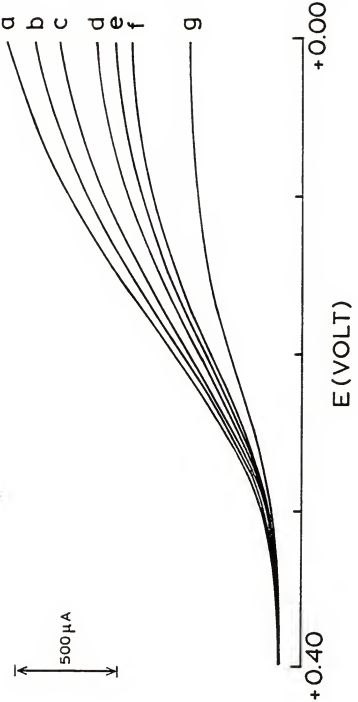
a
b
c
d
e
f
g
500μA
+0.40
+0.00
E (VOLT)

Figure 4.4 Levich plot for data presented in Figure 4.3 at various potentials. Potentials: (a) 0.08; (b) 0.10; (c) 0.12; (d) 0.15; (e) 0.18 V versus SCE.

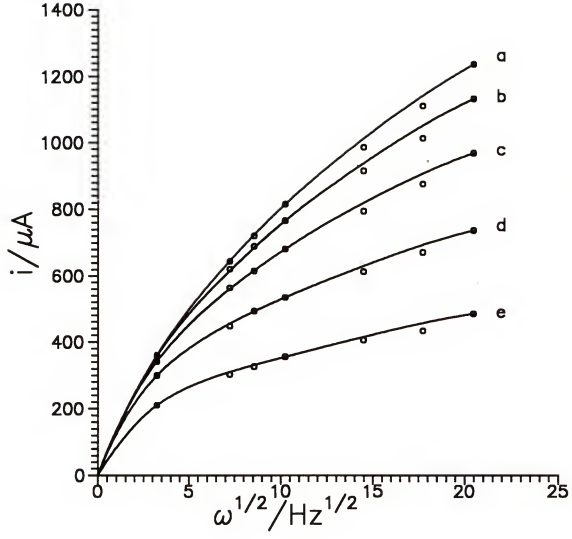
1400
1200
1000
800
600
400
200
0
i/μA
0
5
10
15
20
25
ω^1/2/Hz^1/2
a
b
c
d
e

Figure 4.5 Koutecky-Levich plot for data presented in Figure 4.3 at various potentials. Potentials: (a) 0.08; (b) 0.10; (c) 0.12; (d) 0.15; (e) 0.18 V versus SCE.

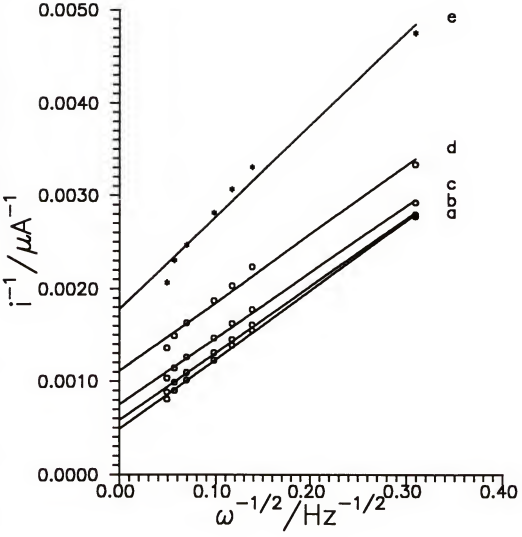
0.0050
0.0040
0.0030
0.0020
0.0010
0.0000
$i^{-1}/\mu A^{-1}$
0.00
0.10
0.20
0.30
0.40
$\omega^{-1/2}/Hz^{-1/2}$
e
d
a or c

Levich plot at high rotation rates. As can be seen in Figure 4.5, at high rotation rates (i.e. as $\omega^{-1/2} \rightarrow 0$), the data points begin to deviate from a straight line. The deviation corresponds to a gradual decrease in electrode area (eq 2.3) with increasing rotation rate. This result is reasonable based on the microelectrode array structure at the surface (as described in section 3.2), and the diffusion layer thickness in an RDE experiment, δ_o, which is a function of rotation rate,

$$\delta_o = 1.61 D^{1/3} \omega^{-1/2} \nu_w^{1/6} \tag{4.34}$$

where ν_w, the kinematic viscosity, is 0.01 cm^2/s for water (Bard and Faulkner, 1980). As described in section 3.1, the CV response at a microelectrode array will depend on the dimensions of the array and the time scale of the experiment, where diffusion layer thickness grows as a function of time (eq 1.9). In the case of an RDE experiment, the diffusion layer thickness is controlled by convection where the thickness can be expressed by equation 4.34. At sufficiently slow rotation rates, the diffusion layer thickness will be large relative to the microelectrode array dimensions, and therefore the response will be characteristic of the entire geometric area (analogous to slow scan rates in CV experiments). At sufficiently fast rotation rates, the diffusion layer thickness will approach the dimensions of the microelectrode array, eventually resulting in a response characteristic of the active area (analogous to CV at fast scan rates). For example, at a rotation rate of 400 Hz, the diffusion layer thickness is approximately 7 μm. This is similar to the dimensions of the microelectrode array observed at an unpolished TTF-TCNQ/PVC polymer paste electrode as described in sections 3.2.3 and 3.2.4.

The y-intercepts of the Koutecky-Levich plots represent the kinetic current i_k (eqs 2.2 and 2.4). Values of k_f were calculated from the intercepts in Figure 4.5 (eq 2.4). The k^o value was determined from ln k_f versus E plots (Figure 4.6). According to equation 1.7,

Figure 4.6 Plot of ln k_f versus E for the reduction of 15 mM $Fe(CN)_6^{3-}$ in 1 M phosphate buffer, pH 7.0, where values of k_f were determined from intercepts in Figure 4.5.

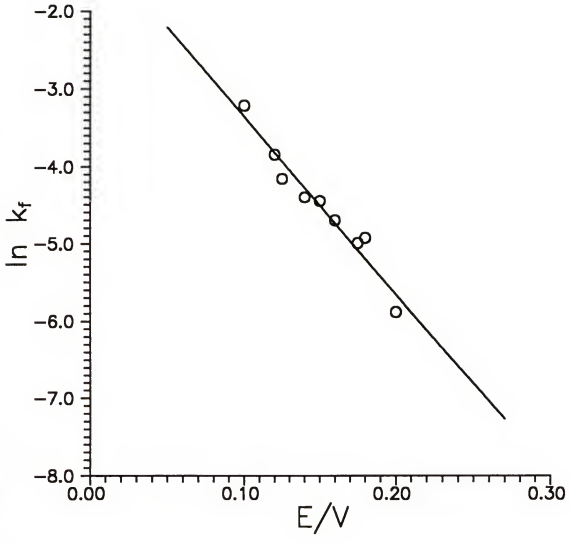
−2.0
−3.0
−4.0
−5.0
−6.0
−7.0
−8.0
ln k_f
0.00
0.10
0.20
0.30
E/V

$k^o = (1.44 \pm 0.13) \times 10^{-3}$ cm/s at the formal potential ($E^o = 0.200$ V). From the slope of the plot in Figure 4.6, a cathodic transfer coefficient, α, of 0.59 ± 0.05 was calculated using equation 1.7. The α value of ca. 0.5 suggests that ferricyanide undergoes a simple, quasi-reversible, outer-sphere, one-electron reduction at TTF-TCNQ electrodes.

A k^o value was also determined from the separation of the CV peaks using the method of Nicholson as described in section 2.3.2.1 (Nicholson, 1965). A diffusion coefficient of 7.63×10^{-6} cm^2/s was used in these calculations. Calculations using the method of Nicholson are not affected by surface roughness since the time scale of the CV experiment is such that the diffusion layer thickness is sufficiently larger than the dimension of the microelectrode array structure. The k^o value obtained by this method (1.09×10^{-3} $cm\text{-}s^{-1}$) was in good agreement with that determined by RDE.

Oxidation kinetics of many small biological molecules are known to be sensitive to the condition and type of the electrode surface (Freund and Brajter-Toth, 1989; Dong and Kuwana, 1984; Wightman et al., 1984; Poon and McCreery, 1986;Bodalbhai and Brajter-Toth, 1988). In addition to being catalytically oxidized on TTF-TCNQ electrodes (McKenna et al., 1988), ascorbic acid and catechols have been used as probes in the studies of activity of graphite electrodes because the rates of their kinetics are dramatically affected by the surface conditions (Dong and Kuwana, 1984; Wightman et al., 1984). The reactions of catechol and ascorbic acid redox couples both involve a two-electron two-proton oxidation where the RDS has been shown to be dependent on the electrode surface. Wightman and coworkers have demonstrated that at carbon paste electrodes, where the observed kinetics are relatively slow, the first electron transfer is rate determing, whereas at activated GC, where the kinetics are faster, the RDS changes from the second electron transfer to the first as the oxidation potential is increased (Wightman et al., 1984). Because of the sensitivity of the oxidation

reactions of catechol and ascorbic acid to the electrode surface, and the fact that their mechanisms have been well characterized, these compounds were chosen as probes to study the kinetics at TTF-TCNQ electrodes.

The values of rate coefficients obtained at TTF-TCNQ/PVC polymer paste electrodes for the oxidation of ascorbic acid and catechol were obtained from i_k values from the Koutecky-Levich plots as described above for ferricyanide. Plots of ln k_b versus E, where k_b is the apparent heterogenous rate coefficient for an oxidation (eq 1.8), yielded straight lines with correlation coefficients of 0.9922 and 0.9892 for ascorbic acid and catechol, respectively (Figure 4.7). Values of k^o were determined for both ascorbic acid and catechol from Figure 4.7 at their two-electron formal potentials, -0.062 V (Gehardt and Adams, 1982) and +0.155 V, respectively. For ascorbic acid k_b(-0.062 V) = (1.8 $\pm$ 0.2) X 10^{-4} cm-s^{-1} and for catechol, k_b(+0.155 V) = (2.4 $\pm$ 0.7) X 10^{-3} cm-s^{-1}. From the slopes of ln k_b versus E, anodic transfer coefficient values (1-α) of 0.23 $\pm$ 0.01 and 0.22 $\pm$ 0.02 were determined (eq 1.8) for ascorbic acid and catechol, respectively. These values of transfer coefficient are similar to a value of 0.3 reported from Tafel plots for the oxidation of the flavin site in glucose oxidase on a TTF-TCNQ/PVC polymer paste electrode (Albery et al., 1987), and are consistent with a mediated redox process as derived in section 4.1.2.

The observation that TCNQ° rich surfaces are present under conditions where electrochemical oxidation of biological molecules has been observed, and low 1-α values obtained from RDE experiments, strongly implicates TCNQ° in redox reactions at the TTF-TCNQ electrodes. There have been reports in the literature that TCNQ° can act as a mediator in oxidation reactions (Cenas and Kulys, 1981; Hendry and Turner, 1988). Indeed, sublimed TCNQ° films rapidly turned blue when exposed to ascorbate or catechol, indicating formation of NaTCNQ (Melby et al., 1962). Heterogeneous oxidation of ascorbate and catechol by

Figure 4.7 Plot of ln k_s versus E for the oxidation of 4 mM ascorbic acid (○) and 2 mM catechol (□) in 0.5 M phosphate buffer, pH 7.0.

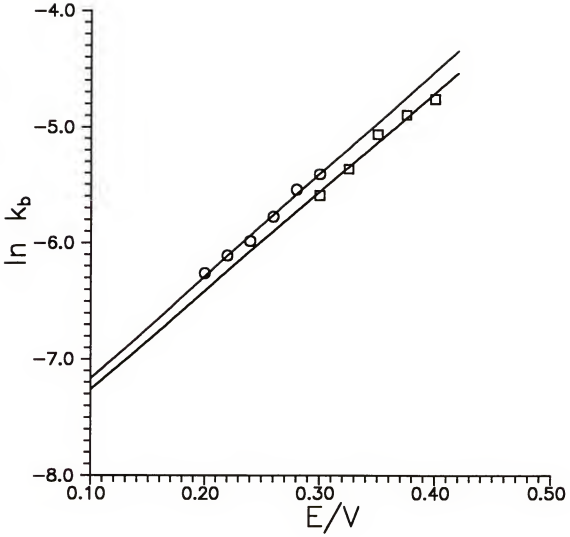
−4.0
−5.0
−6.0
−7.0
−8.0
ln k_b
0.10
0.20
0.30
0.40
0.50
E/V

$TCNQ^o$ was also confirmed by ultrasonication of $TCNQ^o$ crystals (orange) in the presence of 10 mM of ascorbic acid or catechol in 0.5 M sodium phosphate buffer (pH 7). This resulted in reduction of $TCNQ^o$ within seconds, as evidenced by formation of a fine suspension of blue-purple crystals of NaTCNQ (Melby et al., 1962). Sodium phosphate buffer alone had no effect on $TCNQ^o$. Oxidation of ascorbate and catechol by $TCNQ^0$ is expected based on the formal potential for the $TCNQ^{o/-}$ couple ($E^{o'} = +0.17$ V) (Ward, 1989), the two-electron formal potential of ascorbate ($E^{o'} = -0.062$ V) (Wightman et al., 1984) and catechol ($E^{o'} = +0.155$ V) (see Figure 1.7).

Albery and coworkers have proposed a mechanism to account for the low value of 1-α measured for glucose oxidase at TTF-TCNQ/PVC polymer paste electrodes. This mechanism is shown below (eqs 4.35-4.38) and involves mediation by surface adsorbed $TCNQ^o$ (Albery et al., 1987),

$$TTF\text{-}TCNQ(s) \xrightarrow{K_1} TTF^0(s) + TCNQ^0(s) \tag{4.35}$$

$$TTF^0(s) \underset{-e^-}{\overset{k_2}{\rightarrow}} TTF^+(s) \tag{4.36}$$

$$TCNQ^0(s) \xrightarrow{k_3[E]} TCNQ^-(s) \tag{4.37}$$

$$TTF^+(s) + TCNQ^-(s) \rightarrow TTF\text{-}TCNQ(s) \tag{4.38}$$

The proposed mechanism involves the dissociation (eq 4.35) of TTF-TCNQ to TTF^0 and $TCNQ^0$, on the electrode surface, at the applied potential of +0.050 V. This is followed by the faradaic oxidation of TTF^0 (eq 4.36) and the oxidation of the enzyme by $TCNQ^o$ (eq 4.37), which is reduced in the process. The fluxes of the oxidation and reduction reactions 4.36 and 4.37 are assumed to be equal. Oxidation is proposed to be followed by the

recombination of TTF^+ and $TCNQ^-$ to form the TTF-TCNQ complex (eq 4.38). The mechanism assumes that both neutral and charged TTF and TCNQ remain immobilized on the electrode surface. This mechanism accounts for the apparent α of approximately 0.25 which was measured from Tafel slopes (Albery et al., 1987).

Based on the observation that a $TCNQ^o$ rich surface is being produced throughout most of the potential window because of the removal of TTF^+, a mechanism involving adsorbed $TCNQ^o$ alone seems more appropriate. A mechanism involving heterogeneous redox catalysis, similar to the one proposed by Albery and coworkers (Albery et al., 1987) which can account for the low apparent α values of 0.23 determined here for ascorbate and catechol, and which involves adsorbed $TCNQ^o$ in the absence of TTF can be written as

$$\text{Red} + TCNQ^0(s) \xrightarrow{k_1} TCNQ^-(s) + \text{Ox} \qquad (4.39)$$

$$TCNQ^-(s) \xrightarrow{k_2} TCNQ^0(s) + e^- \qquad (4.40)$$

This mechanism is similar to that derived in section 4.1.2 for a mediated electron transfer reaction under steady-state conditions. Under steady-state conditions (i.e. the concentration of the intermediate, $TCNQ^-$, remains constant), the fluxes in reactions 4.39 and 4.40, where Red represents the reduced form of the analyte (i.e. ascorbate or catechol), are equal. Assuming that the value of 1- β (see eq 4.4) associated with the elementary one-electron oxidation reaction 4.40 is 0.5, the apparent anodic transfer coefficient (1-α) is expected to be 0.25 which is in agreement with the value of 0.23 determined in this study.

4.3 Characterization of Weak Surface/Substrate Interactions Which Result in Increased Surface Concentrations

Specific adsorption of redox active species results in the formation of a partial or complete layer on the electrode surface. The surface excess, Γ, can be described in terms of an isotherm (Laviron, 1982; Parsons, 1990). In the case of a stationary electrode, when a triangular potential function is applied, the total current is a function of the flux of species diffusing to, and the coverage by species adsorbed on, the electrode surface. The effects of adsorption of redox species at stationary electrodes are numerous and have been well characterized (Wopschall and Shain, 1967; Feldberg, 1972). In the case of voltammetry, the presence of species adsorbed on the electrode as well as in solution can result in prepeaks, postpeaks or enhanced peak currents (Wopschall and Shain, 1967; Feldberg, 1972). This complicates interpretation of voltammograms for the purpose of extracting thermodynamic information related to surface/substrate interactions. Systems involving weak adsorption, as described in section 1.3, are the most difficult to interpret with voltammetry since currents resulting from adsorbed material cannot be distinguished from those arising from diffusion to the surface (Wopschall and Shain, 1967). This is a result of the fact that the thermodynamics of the redox reaction are not significantly altered as a result of adsorption. Under these conditions, the diffusion-controlled and the adsorption-controlled responses occur at nearly the same potential, resulting in an enhanced response over that expected for diffusion alone.

Although methods have been introduced to identify the presence of weak adsorption (Wopschall and Shain, 1967; Feldberg, 1972) including semi-integral analysis (Bowling and McCreery, 1988), with the exception of involved digital simulation (Wopschall and Shain, 1967; Feldberg, 1972), no means for extracting thermodynamic information, in terms of surface excess, using voltammetry in the presence of weak adsorption has been demonstrated.

Since weak adsorption is common, it is critical that responses due to diffusion and adsorption be separated in order to characterize these systems.

It has been demonstrated by Bowling and McCreery (Bowling and McCreery, 1988) that semi-integration of voltammetric responses can be used as a fast, straightforward, means for the qualitative identification of weak adsorption where the adsorption-controlled and diffusion-controlled redox reactions occur reversibly at the same potential. To the best of the author's knowledge, there have been no reports of the use of semi-integral analysis for quantifying weak adsorption or determining surface concentration in the presence of weak adsorption.

It is the purpose of this work to demonstrate that semi-integration can be used to extract thermodynamic information, in terms of surface excess and surface concentration, in the presence of weak adsorption, thereby extending the utility of semi-integral analysis as a tool in electroanalysis. The reduction of p-benzoquinone at pyrolytic graphite is used to demonstrate the utility of this method, and results obtained for surface excess are confirmed using CC (Anson, 1966).

In addition, a thin-layer model, analogous to the weak adsorption case, is introduced. The thin-layer model consists of a porous thin-layer at an electrode surface into which species can partition and diffuse. Simulations of the thin-film model described herein are used to demonstrate that semi-integral analysis may be used to determine concentration within the film ($C(0,t)$) and partitioning coefficients of species between the bulk and the thin film. This model is used to demonstrate the properties of a general electrode surface structure which may be used for the study of thin porous films. The success of this model also suggests that semi-integration analysis may be used as a powerful tool to determine surface concentration of

electroactive species at electrode surfaces in the presence of other fast surface phenomena which affect surface concentration.

4.3.1 Identification and Quantitation of Weak Adsorption with Semi-integral Analysis

In a case where redox species are adsorbed on an electrode surface, and are also present in solution, when a triangular potential function is applied to an electrode, the total measured current is determined by the diffusion and adsorption of the redox species. When adsorption and diffusion occur, the total current (i) can be expressed as (Bard and Faulkner, 1980)

$$\frac{i}{nFA}=D_{Ox}[\frac{\partial C_{Ox}(x,t)}{\partial x}]_{x=0}-\frac{\partial \Gamma_{Ox}}{\partial t}=-[D_{Red}(\frac{\partial C_{Red}(x,t)}{\partial t})_{x=0}-\frac{\partial \Gamma_{Red}(t)}{\partial t}] \qquad (4.41)$$

where $(\partial C(x,t)/\partial x)_{x=0}$ is the diffusional flux at the electrode surface of Ox or Red, and $\partial\Gamma/\partial t$ is the change in surface excess of Ox or Red with time due to the presence of adsorbed material at the electrode surface.

If the electrode reaction is reversible, the flux due to diffusion of reactant (either Ox or Red) can be expressed as (Nicholson and Shain, 1964)

$$D[\frac{\partial C(x,t)}{\partial x}]_{x=0}=C^{*}\sqrt{D a}\ \sqrt{\pi}\chi(at) \qquad (4.42)$$

where

$$a=\frac{nF\nu}{RT} \qquad (4.43)$$

$$at=\frac{nF\nu t}{RT}=(\frac{nF}{RT})(E_{1/2}-E) \qquad (4.44)$$

and $\chi(at)$ is a function, with the shape of a reversible voltammetric response (equation (2.17)) (Nicholson and Shain, 1964; Oldham, 1979).

In cases where the rate of adsorption is fast, the contribution of reactant adsorption to the overall response in equation 4.41 is determined by the isotherm describing surface excess as a function of adsorbate concentration,

$$G(\Gamma(t)) = \ln C(0,t) - \frac{\Delta G_a}{RT} \tag{4.45}$$

where ΔG_a is the free energy of adsorption, C(0,t) is the surface concentration of the adsorbing species at any time, t, and $G(\Gamma(t))$ is a function of surface excess at any time, t, whose form depends on the isotherm chosen (Parsons, 1961). A general characteristic of isotherms (with some exceptions, the Freundlich isotherm for example) is that as the concentration of the adsorbing species decreases and/or adsorption becomes weaker, their form approaches Henry's law (Parsons, 1961),

$$\Gamma(t) = \Gamma_s \beta C(0,t) = bC(0,t) \tag{4.46}$$

where Γ_s is the saturation coverage and b is the strength of adsorption,

$$\beta = \exp^{-\frac{\Delta G_a}{RT}} \tag{4.47}$$

Under conditions of low concentration and weak adsorption (i.e. $\beta C \ll 1$), and where Ox and Red are adsorbed to equal degrees ($b_{Ox} \approx b_{Red}$) the total surface excess will remain constant as a function of time or potential, and as a result, diffusion and adsorption can be decoupled. When electron transfer is nernstian, the adsorption component of equation 4.41 can be expressed as

$$-\frac{\partial \Gamma}{\partial t} = a\Gamma^* \frac{\exp(-at)}{\{1+\exp(-at)\}^2} \tag{4.48}$$

which is (Oldham and Zoski, 1980)

$$-\frac{\partial\Gamma}{\partial t}=a\Gamma^{*}\ \frac{1}{4}\mathrm{sech}^{2}(\frac{at}{2}) \tag{4.49}$$

Considering equations 4.42 and 4.49, equation 4.41 can be rewritten as

$$\begin{aligned}\frac{i}{nFA}&=C_{Ox}^{*}\sqrt{D_{Ox}a}\ \sqrt{\pi}\chi(at)+a\Gamma_{Ox}^{*}\ \frac{1}{4}\mathrm{sech}^{2}(\frac{at}{2})\\&=-[C_{Red}^{*}\sqrt{D_{Red}a}\ \sqrt{\pi}\chi(at)+a\Gamma_{Red}^{*}\ \frac{1}{4}\mathrm{sech}^{2}(\frac{at}{2})]\end{aligned} \tag{4.50}$$

The semi-integration ($d^{-1/2}/dt^{-1/2}$) of the sum of two functions is equal to the sum of the individual semi-integrated functions (Oldham and Spanier, 1974),

$$\frac{d^{-1/2}}{dx^{-1/2}}\{f(x)+g(x)\}=\frac{d^{-1/2}}{dx^{-1/2}}f(x)+\frac{d^{-1/2}}{dx^{-1/2}}g(x) \tag{4.51}$$

Therefore, the total semi-integrated current (I) is proportional to the sum of the individual semi-integrated functions in equation 4.50,

$$\begin{aligned}\frac{I}{nFA}&=C_{Ox}^{*}\sqrt{D_{Ox}a}\,\frac{d^{-1/2}}{dt^{-1/2}}\sqrt{\pi}\chi(at)+a\Gamma_{Ox}^{*}\,\frac{d^{-1/2}}{dt^{-1/2}}\,\frac{1}{4}\mathrm{sech}^{2}(\frac{at}{2})\\&=-[C_{Red}^{*}\sqrt{D_{Red}a}\ \frac{d^{-1/2}}{dt^{-1/2}}\sqrt{\pi}\chi(at)+a\Gamma_{Red}^{*}\frac{d^{1/2}}{dt^{1/2}}\ \frac{1}{4}\mathrm{sech}^{2}(\frac{at}{2})]\end{aligned} \tag{4.52}$$

where (Goto and Ishii, 1975)

$$\frac{d^{-1/2}}{dt^{-1/2}}\sqrt{\pi}\chi(at)=\frac{1}{\sqrt{a}}[\frac{1}{2}+\frac{1}{2}\tanh(\frac{at}{2})] \tag{4.53}$$

and (Dalrymple-Alford et al., 1977)

$$\frac{d^{-1/2}}{dt^{-1/2}}\frac{1}{4}\mathrm{sech}^{2}(\frac{at}{4})=\frac{1}{\sqrt{a}}\ \sqrt{\pi}\chi(at) \tag{4.54}$$

Therefore equation 4.52 can be rewritten as

$$\frac{I}{nFA}=C^*_{Ox}\sqrt{D_{Ox}}\,[\frac{1}{2}+\frac{1}{2}\tanh(\frac{at}{2})]+\sqrt{a}\;\Gamma^*_{Ox}\sqrt{\pi}\,\chi(at)$$
$$=-[C^*_{Red}\sqrt{D_{Red}}\,[\frac{1}{2}+\frac{1}{2}\tanh(\frac{at}{2})]+\sqrt{a}\;\Gamma^*_{Red}\sqrt{\pi}\,\chi(at)] \qquad (4.55)$$

It in turn becomes apparent that when at becomes large,

$$\lim_{at\to\infty}\;[\frac{1}{2}+\frac{1}{2}\tanh(\frac{at}{2})]=1 \qquad (4.56)$$

and (Oldham, 1979)

$$\lim_{at\to\infty}\;\sqrt{\pi}\,\chi(at)=(\pi at)^{-1/2} \qquad (4.57)$$

equation 4.55 in turn becomes

$$\frac{I}{nFA}=C^*_{Ox}\sqrt{D_{Ox}}+\frac{\sqrt{a}\;\Gamma^*_{Ox}}{\sqrt{\pi at}}=-[C^*_{Red}\sqrt{D_{Red}}+\frac{\sqrt{a}\;\Gamma^*_{Red}}{\sqrt{\pi at}}] \qquad (4.58)$$

As at becomes large equation 4.58 predicts that a plot of semi-integrated current versus the inverse square root of time, I versus $(\pi at)^{-1/2}$, where $at\to\infty$, will result in a straight line with a slope of $nFAa^{1/2}\Gamma_{Ox}^*$ and an intercept, at $(\pi at)^{-1/2}=0$, of $nFAC^*_{Ox}D_{Ox}^{1/2}$, allowing simple determination of Γ^*_{Ox} and C^*_{Ox}.

The behavior of the functions in equation 4.50, f(at): $\sqrt{\pi}\;\chi(at)$, (1/4)sech^2(at/2) and the sum of the two, is shown as a function of at in Figure 4.8a. The semi-integrated forms of these functions (eq 4.58), $d^{-1/2}f(at)/dt^{-1/2}$: (1/2) + (1/2)tanh(at/2), $\sqrt{\pi}\;\chi(at)$ and the sum of the two, are shown as a function of at in Figure 4.8b. Figure 4.9 shows the behavior of the semi-integrated functions, $d^{-1/2}f(at)/dt^{-1/2}$, as a function of $(\pi at)^{-1/2}$. As can be seen in Figure 4.9, as at becomes large, the function (1/2) + (1/2)tanh(at/2) approaches 1 (short dashed line) and becomes independent of at while the function $\chi(at)$ becomes linear with a slope of $(\pi at)^{-1/2}$

Figure 4.8 (a) Plot of (————) (1/4)sech^2(at/2), (---------) χ(at), and (— — —) (1/4)sech^2(at/2) + χ(at) versus at; (b) plot of (————) χ(at), (---------) (1/2) + (1/2)tanh(at/2), and (— — —) χ(at) + (1/2) + (1/2)tanh(at/2) versus at.

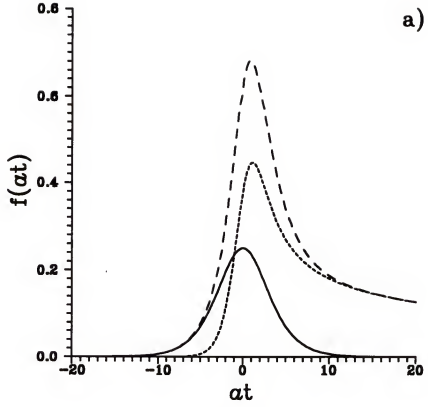
a)
f(at)
0.8
0.6
0.4
0.2
0.0
-20
-10
0
10
20
at

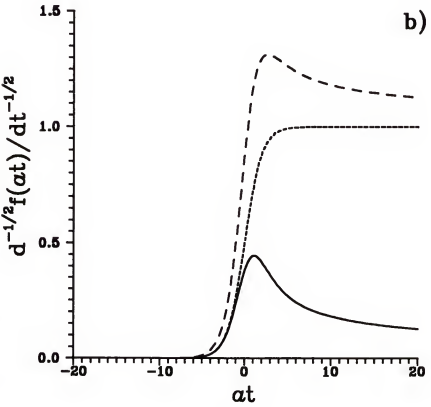
b)
$d^{-1/2}f(at)/dt^{-1/2}$
1.5
1.0
0.5
0.0
-20
-10
0
10
20
at

Figure 4.9 Plot of (————) $\chi(at)$, (---------) $(1/2) + (1/2)\tanh(at/2)$, and (— — —) $\chi(at) + (1/2) + (1/2)\tanh(at/2)$ versus $(\pi at)^{-1/2}$.

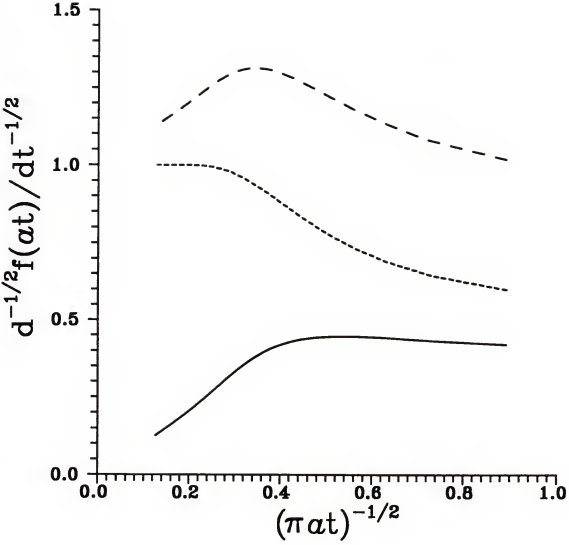
1.5
1.0
0.5
0.0
0.0
0.2
0.4
0.6
0.8
1.0
$d^{-1/2}f(\alpha t)/dt^{-1/2}$
$(\pi \alpha t)^{-1/2}$

(solid line). The sum of these two functions in turn also becomes a straight line as at becomes large, and can be described based on equations 4.56 and 4.57 by the equation $d^{-1/2}f(at)/dt^{-1/2} = (\pi at)^{-1/2} + 1$.

4.3.2 Weak Adsorption of p-Benzoquinone on Graphite Electrodes

In order to demonstrate the utility of the semi-integral analysis method for the identification and quantitation of weak adsorption, the reduction of p-benzoquinone on RPG was studied. Figure 4.10 demonstrates the complex nature of the interactions between p-benzoquinone and RPG. Adsorption of p-benzoquinone on RPG was demonstrated from a plot of log $i_{p,c}$ versus log ν which resulted in a slope of 0.64, and as discussed in section 2.3.2.1 is characteristic of weak adsorption. By comparing CVs in phosphate buffer before (large dash) and after (short dash) the faradaic response (solid line), the presence of two small cathodic and anodic peaks is clear. These peaks (short dash) remained after repeated washing of the electrode with deionized/distilled water and were unaffected by repeated cycling in phosphate buffer. This suggests that the peaks may be due to irreversibly adsorbed p-benzoquinone. For clarity, faradaic responses resulting from this phenomena will be designated by the subscript irr (i.e. $i_{c,irr}$ for the cathodic current due to irreversible adsorption) whereas faradaic responses resulting form weakly adsorbed p-benzoquinone will be designated by the subscript w (i.e. $i_{c,w}$ for the cathodic current due to weak adsorption). The total p-benzoquinone response (solid line) is $i_T = i_{irr} + i_w + i_{dl}$ where i_{dl} is the current resulting from double layer charging.

Clearly weak adsorption disappears after the electrode is transferred to blank solution. In order to obtain the response due to weak adsorption (i_w) only, $i_{irr} + i_{dl}$ (short dashed line, Figure 4.10) was subtracted from i_T (solid line, Figure 4.10), and the result is shown in

Figure 4.10 Cyclic voltammetry of RPG in blank 1 M phosphate buffer solution, pH 7, (— — —) before, and (----------) after cyclic voltammetry of (————) 1 mM p-benzoquinone/1 M phosphate buffer, pH 7, at a scan rate of 1 $V \cdot s^{-1}$.

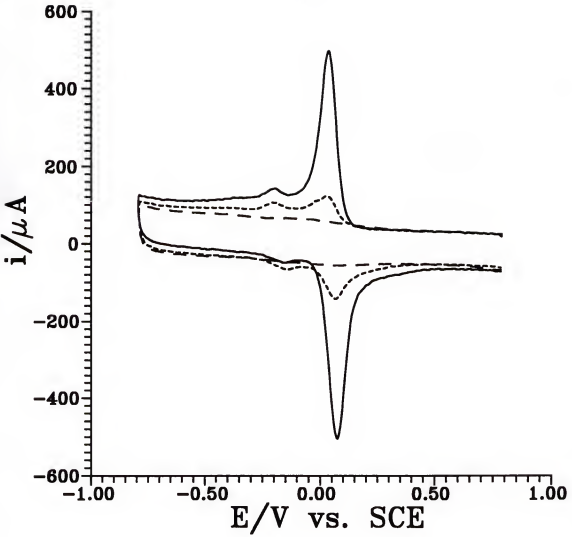
600
400
200
0
−200
−400
−600
i/μA
−1.00
−0.50
0.00
0.50
1.00
E/V vs. SCE

Figure 4.11a. The semi-integration of the response in Figure 4.11a is shown in Figure 4.11b. The peaked semi-integrated response demonstrates the presence of weak adsorption as described in section 4.3.1.

The initial surface excess ($\Gamma^*_{Ox,w}$) was determined from the slope of the plot of I versus $(\pi at)^{-1/2}$. For a reduction as $at \rightarrow \infty$ or $(\pi at)^{-1/2} \rightarrow 0$, equation 4.58 becomes

$$I = nFAC^*_{Ox}\sqrt{D_{Ox}} + \frac{\sqrt{a}\ \Gamma^*_{Ox}}{\sqrt{\pi t}} \tag{4.59}$$

and therefore a plot of I versus $(\pi at)^{-1/2}$ becomes linear with a positive slope (see Figure 4.12). The linear portion of the data in Figure 4.12 (solid line) was used to determine Γ^*_{Ox}. As mentioned in the experimental section, a value of $E_{1/2}$ was chosen such that the intercept of I versus $(\pi at)^{-1/2}$ yielded $nFAC_{Ox}{}^{1/2}D_{Ox}{}^{1/2}$. This value corresponded to $E_{1/2} = 0.040$ V which was similar to $E^{o'}$ (0.047 V) determined from the average of the anodic and cathodic peak potential, which is taken as an approximation of $E_{1/2}$. The results are shown in Table 4.2 and are compared to results obtained with CC.

In CC, surface excess ($\Gamma^*_{Ox,w}$ and $\Gamma^*_{Ox,irr}$) was determined from the intercepts of plots of Q versus $t^{1/2}$ as described in section 2.3.2.3. Values of Q_{dl}, $Q_{ads,irr}$, and $Q_{ads,w}$ were determined from CC at RPG. Q was measured in A) phosphate buffer prior to exposure to p -benzoquinone; B) 1 mM p-benzoquinone; and C) phosphate buffer following B. The intercepts of plots of Q versus $t^{1/2}$ resulted in Q_{dl}, $Q_{dl}+Q_{ads,irr}+Q_{ads,w}$, and $Q_{dl}+Q_{ads,irr}$ for A, B, and C, respectively. These results are summarized in Table 4.2.

4.3.3 Thin-layer Model of Weak Adsorption

One effect of weak adsorption is to increase surface concentration. Another condition which can produce the same effect is the presence of a thin porous film (or thin-layer) at the

Figure 4.11 (a) Linear sweep voltammogram and (b) semi-integrated linear sweep voltammogram of 1 mM p-benzoquinone/1 M phosphate buffer, pH 7, on RPG following background subtraction, scan rate of 1 $V \cdot s^{-1}$.

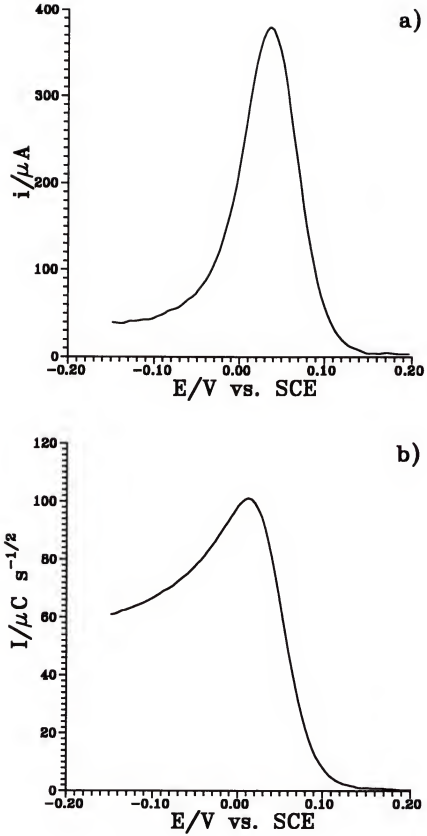
a)
400
300
200
100
0
i/μA
-0.20
-0.10
0.00
0.10
0.20
E/V vs. SCE
b)
120
100
80
60
40
20
0
I/μC s^-1/2
-0.20
-0.10
0.00
0.10
0.20
E/V vs. SCE

Figure 4.12 Plot of semi-integrated current from Figure 4.11b versus $(\pi at)^{-1/2}$, where values of at were determined as described in text (eq 4.44).

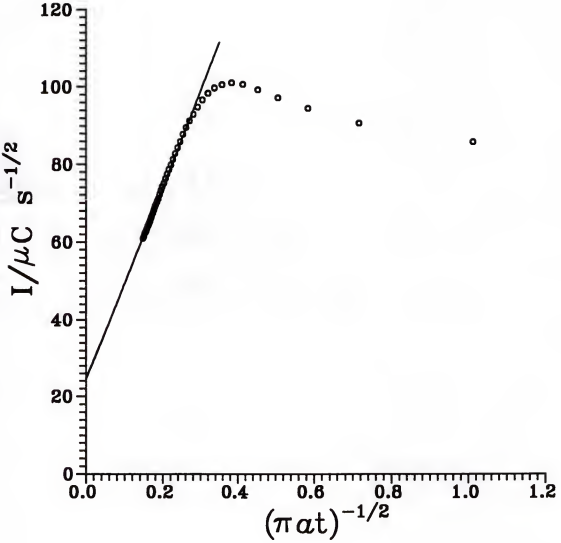
120
100
80
60
40
20
0
0.0
0.2
0.4
0.6
0.8
1.0
1.2
I/μC s^-1/2
(πat)^-1/2

Table 4.2. Charge and calculated surface excess of both strong and weakly adsorbed p-benzoquinone on RPG; n=2 and A=0.047±0.005 cm².

Q_{dl}[a] μC	$Q_{ads,irr}$[a] μC	$Q_{ads,w}$[a] μC	$\Gamma^*_{ox,irr}$[a] nmol/cm²	$\Gamma^*_{ox,w}$[a] nmol/cm²	$\Gamma^*_{ox,w}$[b] nmol/cm²
25.5 ± 0.3	12.7 ± 0.4	25.8 ± 0.3	1.4 ± 0.2	2.8 ± 0.3	3.1 ± 0.4

[a] determined using chronocoulometry.
[b] determined using semi-integral analysis.

electrode surface into which reactant from solution bulk can diffuse and partition. When mass transfer within the film is negligible on the time scale of a voltammetric experiment (i.e. thickness $<<(2Dt)^{1/2}$) the response is similar to that observed for adsorption. The magnitude of the faradaic current, i, will be proportional to the apparent initial surface excess, Γ_{app}^{*} (mol/cm^2), within the film (i.e. the product of the initial concentration in the film, $C^{*}(t)_{t=0}$ (mol/cm^3) and its thickness, ℓ, (cm)): $\Gamma_{app}^{*}=C^{*}(0)\cdot\ell$.

A model which is consistent with the situation described above is shown in Figure 4.13. In this model a thin surface layer or film (i.e. thin-layer of thickness ℓ, in Figure 4.13) containing higher concentrations of the reactant ($C^{*}(t)$, mol/cm^3) exists between the electrode surface and the bulk solution ($C(\ell,t)$), where the concentration $C^{*}(t)$ is determined by an equilibrium constant (or partition coefficient),

$$K_{eq}=\frac{C^{*}(t)}{C(\ell,t)} \tag{4.60}$$

where $K_{eq} > 1$ for adsorption. The thickness, ℓ, as is the case in a thin-layer cell (Bard and Faulkner, 1980), should be sufficiently small, that mass transfer in ℓ is not significant (i.e. $\ell << (2Dt)^{1/2}$). For example, for ℓ to be one order of magnitude less than $(2Dt)^{1/2}$ for a 0.1μm thick film in which the diffusion coefficient of the probe is 10^{-8} cm^2/s, the time scale of the experiment should be not shorter than 0.5 seconds.

Assuming that equilibrium between the surface layer and the adjacent solution is fast, the overall response will remain diffusion controlled. Therefore, the solution to the diffusion equation problem for semi-infinite linear diffusion conditions should remain unchanged (Bard and Faulkner, 1980). For a reduction,

Figure 4.13 Thin-layer model illustrated in a plot of concentration, C, versus distance, x, from the electrode surface, where $x=0$ represents the electrode surface/thin-layer interface and $x=\ell$ represents the thin-layer/solution interface. C^* and C^* are the concentrations of the reacting species at $t=0$ in bulk solution and within the thin-layer, respectively. $C^*(t)$ and $C(\ell,t)$ are the concentrations of the reacting species within the thin-layer and in solution at the surface of thin-layer, respectively, at $t>0$, where $C^*(t)$ and $C(\ell,t)$ are in equilibrium described by K_{eq}.

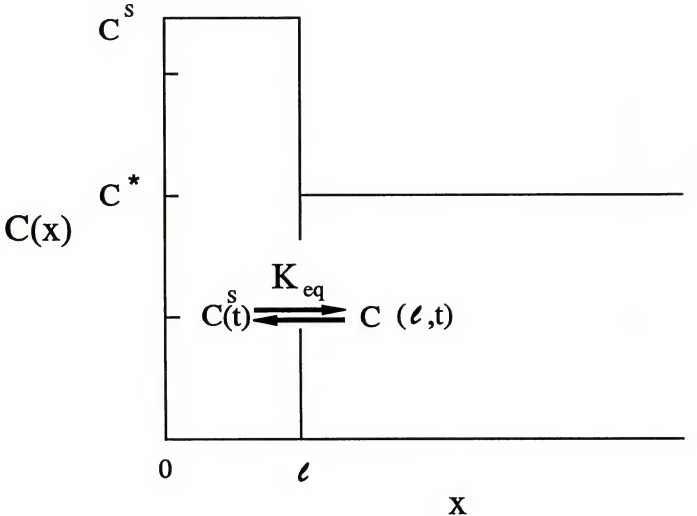
C^s
C*
C(x)
K_eq
C^s(t)
C (ℓ,t)
0
ℓ
x

$$C_{Red}(0,t) = \frac{I(t)}{nFAD_{Red}^{1/2}} \qquad (4.61)$$

where $C_{Red}(0,t)$ is the surface concentration of Red (i.e. the product) and should therefore be the concentration of Red within the film $C_{Red}^{*}(t)$. Although a rigorous derivation of equation 4.61 for the condition of the thin-layer model is not presented here, good agreement between surface concentration determined in the simulation and via semi-integration of the simulated current and equation 4.61 is obtained, as will be shown in section 4.3.4.

4.3.4 Semi-integral Analysis in the Presence of Thin-layer Behavior and Diffusion

In order to demonstrate that semi-integration of a voltammetric response produced by the thin-layer model described above can be used to determine surface concentration (C(0,t)) within the thin-layer, a response for a simple case was digitally simulated. Figure 4.14 shows the simulated normalized CV current for a simple one-electron, reversible reduction reaction where only Ox (or the reactant) is partitioned into the film ($K_{eq,Ox}$=4). The value of $K_{eq,Ox}$ was chosen because it resulted in reasonable values of surface excesses (see below). Under these conditions the surface concentration of Ox, $C_{Ox}(0,t)$, is determined by electrode potential, diffusion of Ox from bulk solution, and K_{eq} (eq 4.61), whereas the surface concentration of Red, $C_{Red}(0,t)$, is only a function of electrode potential and Red diffusion. Equation 4.61 can be used to determine $C_{Red}(0,t)$ (or the concentration of the reaction product) directly from the semi-integrated voltammetric current. Figure 4.15 shows the surface concentration of Red normalized for the initial bulk concentration of Ox ($C_{Red}(0,t)/C_{Ox}^{*}$) determined in the simulation and from the semi-integrated simulated current. The solid line shows $C_{Red}(0,t)/C_{Ox}^{*}$ based on the concentration of Red in the first volume element (i.e. within the thin-layer) in the simulation for the forward and reverse scan. The circles show values of

Figure 4.14 Simulated cyclic voltammogram in the presence of the thin-layer model, where Ox is weakly adsorbed ($K_{eq,Ox}=4$) while Red is not adsorbed.

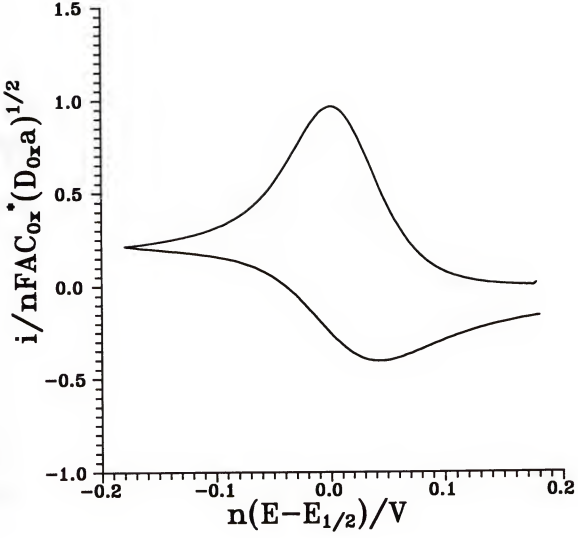
1.5
1.0
0.5
0.0
−0.5
−1.0
−0.2
−0.1
0.0
0.1
0.2
$i/nFAC_{Ox}^{*}(D_{Ox}a)^{1/2}$
$n(E-E_{1/2})/V$

Figure 4.15 Plot of surface concentrations of (— — —) Ox and (————) Red determined in the first volume element (i.e. within the thin-layer) in the simulation and $C_{Ox}(0,t)$ (Δ) and $C_{Red}(0,t)$ (O) from semi-integrated simulated current, equation 4.61, and equation 4.63. $K_{eq,Ox}=4$ and Red not adsorbed.

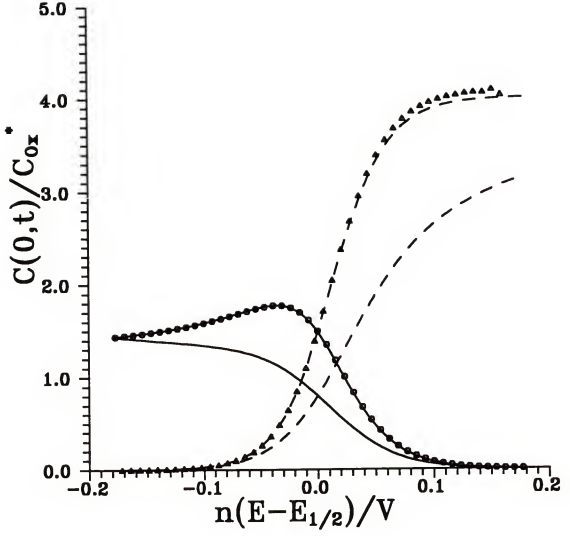
5.0
4.0
3.0
2.0
1.0
0.0
C(0,t)/C*ox
−0.2
−0.1
0.0
0.1
0.2
n(E−E1/2)/V

$C_{Red}(0,t)/C_{Ox}^*$ for the forward scan, determined from the semi-integration of the simulated current and equation 4.61. The close agreement between the surface concentrations determined in the first volume element in the simulation and by semi-integration of currents produced by the simulation demonstrates that semi-integration of current due to preconcentration within a thin-layer or due to weak adsorption results in $C_{Red}(0,t)$ and can, therefore, be used to monitor surface concentration as a function of time or potential. In the case of nernstian behavior,

$$E=E_{1/2}+\frac{RT}{nF}\ln\frac{C_{Ox}(0,t)D_{Ox}^{1/2}}{C_{Red}(0,t)D_{Red}^{1/2}} \tag{4.62}$$

Therefore, if the redox reaction described in the above model is reversible, the surface concentration of Ox, $C_{Ox}(0,t)$, can be determined by substituting equation 4.61 into 4.62,

$$C_{Ox}(0,t)=\frac{I(t)}{nFAD_{Ox}^{1/2}}\exp(\frac{nF}{RT}(E-E_{1/2})) \tag{4.63}$$

Figure 4.15 also shows surface concentrations of Ox as a function of potential where the dashed line represents normalized concentration ($C_{Ox}(0,t)/C_{Ox}^*$) in the first volume element in the simulation while the triangles represent $C_{Ox}(0,t)/C_{Ox}^*$ determined from the semi-integration of the simulated current using equation 4.63.

In order to express $C_{Ox}(0,0)$ or $C_{Ox}^*(0)$ in terms of initial surface excess, Γ^*_{Ox}, which is commonly used to quantitate adsorption, the initial excess surface concentration in the first volume element ($(K_{eq,Ox}-1)C^*_{Ox}$) and the thickness of the volume element, Δx, must be considered,

$$\Gamma^*_{Ox}=(K_{eq,Ox}-1)C^*_{Ox}\,\Delta x \tag{4.64}$$

where

$$\Delta x = \left(\frac{Dt}{D_m j}\right)^{1/2} \qquad (4.65)$$

D is the diffusion coefficient (cm^2/s), t is the time period of the experiment (s), D_m is the dimensionless diffusion coefficient used in the simulation ($D_m = 0.45$) (Bard and Faulkner, 1980; Feldberg, 1972), and j is the number of iterations in the simulation. The values of Γ^*_{Ox} determined using equation 4.64 and the slope obtained from a plot of I versus $(\pi\alpha t)^{-1/2}$, using the method described earlier (eq 4.59), both yielded a value of $7X10^{-10}$ mol/cm^2 using the constants for a typical electrochemical experiment (i.e. n=1 eq; A=0.01 cm^2; ν=1 $V\text{-}s^{-1}$; C^*_{Ox}=$1X10^{-6}$ mol-cm^{-3}; $D_{Ox}=D_{Red}=1X10^{-5}$ $cm^2\text{-}s^{-1}$) and the value for $K_{eq,Ox}$ of 4.

4.4 Conclusions

In this chapter, kinetic data obtained from RDE and CV of small biological molecules (i.e. ascorbic acid and catechol), and QCM measurements have been used to determine the mechanism of electron transfer at TTF-TCNQ electrodes. The data suggest that surface bound $TCNQ^o$ mediates electron transfer, through the chemical oxidation of the biological molecules by $TCNQ^o$, followed by the subsequent electrochemical oxidation of the $TCNQ^-$ produced in the mediation reaction. This mechanism is supported by *in situ* QCM measurements which show that TTF-TCNQ/PVC electrodes experience mass fluctuations due to the loss of TTF^+ at positive potentials and accumulation of $TCNQ^0$ on the surface in the process, and by the observation that $TCNQ^0$ can directly oxidize several biological molecules including ascorbic acid and catechol. A different, direct electron transfer mechanism, was determined for ferricyanide.

This study has also shown the ability of semi-integral analysis to differentiate between the contributions of diffusion and adsorption to voltammetric response, which makes it a powerful tool in the study of redox couples weakly adsorbed on electrode surfaces. One of

the most attractive aspects of the semi-integral analysis method is that identification and quantitation of adsorption (i.e. determination of Γ^* and C^*) can be achieved numerically, from a single voltammetric measurement. Under weak adsorption conditions the contribution of double layer charging may be removed via background subtraction where the background is estimated from the same voltammetric response prior to the onset of the faradaic current. This eliminates the need for additional experiments to determine the contribution of double-layer capacitance.

Furthermore, the capabilities of semi-integral analysis to determine surface concentration in the presence of fast surface phenomena, such as weak adsorption, is illustrated with a thin-layer model. This model follows a model for weak adsorption and has a similar effect on the surface concentration of redox species. In addition to demonstrating the utility of semi-integration for the study of thin porous films, the thin-layer model is a useful tool for predicting the voltammetric behavior of thin films at electrode surfaces, which can be used in the analysis of new, analytically useful, electrode surface structures.

CHAPTER 5
SUMMARY AND FUTURE WORK

The objective of this research was to determine the effect of surface microstructure on the electrochemical response characteristics of tetrathiafulvalene-tetracyanoquinodimethane (TTF-TCNQ) and graphite electrodes, and to illustrate how parameters such as microelectrode array dimensions and surface/substrate interactions govern electrode response.

In Chapter 1, fundamental theory of heterogeneous electron transfer and its relationship to homogeneous electron transfer was discussed. Next, some important aspects of mass transport to surfaces were discussed, emphasizing two important diffusional modes (i.e. semi-infinite linear and radial diffusion). The transition from semi-infinite linear to radial diffusion as a function of time, and the resulting effect on the observed redox reaction rate (or observed current) was described. Based on this discussion, an electrode array model was introduced, and the additional transition from radial diffusion to semi-infinite linear diffusion as a result of diffusion layer overlap between adjacent electrodes in the array was illustrated. This was followed by a discussion of mediation and adsorption, and their affect on electron transfer. Finally, the structural and chemical properties of TTF-TCNQ and graphite were described.

Chapter 2 focused exclusively on experimental approaches used throughout this work. The materials and apparatus used were described in detail. This was followed by a description of experimental techniques and procedures. Electrode preparation procedures for platinum, graphite, and TTF-TCNQ electrodes were described. Electrochemical techniques

including cyclic voltammetry (CV), rotating disk electrode (RDE), chronocoulometry (CC), chronoamperometry (CA), and surface imaging based on surface distribution of copper deposits formed by electrochemical copper deposition were described. Next, surface characterization techniques including quartz crystal microbalance (QCM), scanning tunneling microscopy (STM), and atomic force microscopy (AFM) were covered. Finally, numerical techniques including simulation and numerical semi-integration were described.

Results related to the role of surface microstructure on mass transport at TTF-TCNQ and graphite electrodes were discussed in Chapter 3. In the case of TTF-TCNQ electrodes, qualitative identification of a surface structure, which could be approximated as a random microelectrode array, was achieved by varying the time scale of CV experiments at TTF-TCNQ/PVC polymer paste and pellet electrodes. On sufficiently short time scales (i.e. fast scan rates), the response at the polymer paste electrode approached a steady-state response (characteristic of nonlinear or radial diffusion) revealing microelectrode array behavior. The pellet electrode, on the other hand, did not produce responses characteristic of array behavior, suggesting that the dimensions of the array were significantly smaller than those of the polymer paste electrode.

Quantitative determination of the microelectrode array structure at the unpolished TTF-TCNQ/PVC polymer paste electrode was achieved electrochemically by determining the best fit between experimental and simulated CA responses for arrays with different dimensions. This resulted in a diameter of an average unit cell in an array at unpolished TTF-TCNQ/PVC polymer paste electrodes on the order of ca. 10 μm . The microelectrode array structure was further verified by observing electrochemically deposited copper which was used to decorate regions of electrochemical activity. The distribution of deposits at polished TTF-TCNQ/PVC polymer paste electrodes, which yielded similar responses to those

observed with the TTF-TCNQ pellet electrode, suggested that the surface did have a microelectrode array structure, although radial diffusion to individual electrodes in the array could not be observed electrochemically on the reasonably long time scales (> 1 ms) in this study. The diameters of individual microelectrodes in the array, based on the dimensions of copper deposits, were ca. 1 μm. These results demonstrated the ability to produce and image microelectrode arrays whose dimensions could be easily altered over an order of magnitude from 1 to 10 μm.

Previous results from this group using copper decoration suggested that the surface structure of graphite may also be described by a microelectrode array model. At electrochemically treated glassy carbon electrodes (ECGC), copper deposits were separated by distances less than 1 μm. If copper deposits image the microelectrodes, the presence of such dense arrays could not be detected electrochemically on the relatively long time scales available in this study. Because of the time resolution limitations of the electrochemical techniques in this study (> 1 ms) which determined the dimensional resolution that could be determined, STM and AFM were used to determine the surface dimensions responsible for localized activity at ECGC electrodes.

Since electrochemical treatment (i.e. lattice oxidation) results in the formation of surface oxides, STM showed surface topography complicated by electronic inhomogeneities. AFM images, on the other hand, were not affected by the electronic inhomogeneities, and as a result, significantly different topographies were observed than by STM. AFM images of ECGC electrodes showed small (ca. 0.1 μm) localized defects distributed across a relatively smooth surface, in excellent agreement with previous images of electrochemically deposited copper. These results suggest that graphite electrodes may be described by a microelectrode

array model, and that the increase in activity associated with different treatment procedures may have a common source (i.e. increase in the fraction of active area).

The current state of the art electrochemical instrumentation allows electrochemical measurements to be made on a microsecond time scale. Future studies should allow microelectrode array dimensions on the order of 1 μm and less to be determined using the method presented in this work with copper deposition and AFM. It should be noted that as instrumentation allows faster measurements, the kinetics of the redox couple and electrode charging current associated with the electrode may ultimately limit the utility of this approach.

Throughout Chapter 3, a microelectrode array model has been used to describe observed response. Clearly the goal of future research will be to have complete control over electrode surface structure. To a limited extent, the control of surface structure has been demonstrated here, although a degree of randomness in the array structure has been tolerated in exchange for ease of electrode preparation. With the advancements of lithography techniques, future work should provide a high degree of control over the dimensions of well ordered arrays, cheaply and reproducibly. Another direction of future work will utilize the example of biological membranes (i.e. lipid layers) containing ion channels of molecular dimensions. Self assembling monolayer technology shows considerable promise for producing microelectrode arrays of similar dimensions, although this could result in a random distribution of microelectrodes. An additional advantage of the self assembling monolayer technology is the ability to produce very smooth surfaces, and the ability to easily alter the chemical characteristics of the monolayer.

Chapter 4 focused on the role of surface/substrate interactions in the response of TTF-TCNQ and graphite electrodes. Previous research has shown that TTF-TCNQ catalytically oxidizes certain small biological molecules, although the source of the catalysis has been a

topic of debate. In order to determine the role of the electrode surface in catalysis, if any, *in situ* QCM measurements were made under electrochemical conditions. Observed mass losses suggested that TTF^+ was being lost from the surface, resulting in a $TCNQ^0$ rich surface. RDE experiments were used to determine apparent heterogeneous rate coefficients of ascorbic acid and catechol as a function of potential at $TCNQ^0$ rich surfaces. The potential dependence of the apparent heterogeneous rate coefficient was consistent with a mediated oxidation, suggesting that $TCNQ^0$ is involved in heterogeneous mediation and, therefore that surface chemistry is responsible for the observed catalysis.

One of the most attractive features of molecular solids such as TTF-TCNQ has been the ability to alter their electronic properties through rational modification of their molecular components. Based on the work presented here, modification of molecular components should also be a valid approach for the rational design of the chemical properties of electrode surfaces for specific analytical tasks. It is clear, however, that in future work electronic and chemical repercussions of any modification will have to be considered. For example, altering the formal potential of one component in the molecular solid can alter the extent of charge transfer and in turn the conductivity of the material.

Weak adsorption at electrode surfaces was also a topic discussed in Chapter 4. Rough pyrolytic graphite (RPG) is known to exhibit enhanced peak currents associated with weak adsorption. In this work, a numerical technique (numerical semi-integration) was introduced as a method for the identification and quantitation of weak adsorption in the presence of normal diffusional responses. The semi-integral analysis method allowed the response associated with adsorbed species to be distinguished from the diffusional response, thereby allowing identification and quantitation from a single voltammetric response. In addition, since attractive or repulsive interactions between adsorbing species can affect the voltammetric

response of adsorbed species, deviations of experimentally determined semi-integrated current from the shape of the semi-integrated response derived for a langmuir isotherm (no interaction between adsorbed species) should give at least qualitative information about interactions between adsorbed species.

Because of the similarities between adsorption responses and responses obtained for species trapped in a thin-layer at an electrode surface, the semi-integral analysis method introduced here should be capable of identifying preconcentration of redox active species within thin, permeable films. As a result, partitioning coefficients for electroactive species into thin films may be determined.

APPENDIX A
ACQUISITION, MANIPULATION, AND SEMI-INTEGRAL ANALYSIS
PROGRAM SOURCE CODE

```
'*************************************************************************
' Variables, important throughout the program include:
'     dt! - Time between data points in sec
'     ndps - Number of data points in the pot!()/curr!()/sem!() arrays
'     getcall - Keeps track of stages of data aquisition
'     minx! - minimum value of x (usually pot!())
'     maxx! - maximum value of x (usually pot!())
'     epa and epc - anodic and cathodic peak potentials
'     path$ - Current path from which and to which files are read
'     filename$ - Current filename from which and to which files are read
'     comment$ - Current comment describing conditions to be displayed
'           on screen
'*************************************************************************
'*************************************************************************
' Arrays to be used throughout the program
'     curr!() - Current in uAmps
'     pot!() - Potential in Volts
'     sem!() - Semi-integrated current in uC s^-1/2
'     gma(?) - Gama function values for values of ?
'     colorold%() - contains screen colors which will be over drawn
'*************************************************************************
DECLARE SUB restorel (x1!, y1!, x2!, y2!, slope!, intercept!)
DECLARE SUB slopeintercept (x1!, y1!, x2!, y2!, slope!, intercept!)
DECLARE SUB drawline2 (x1!, y1!, x2!, y2!, slope!, intercept!)
DECLARE SUB movesquare (xcorr!, ycorr!, dx!, dy!, ste!)
DECLARE SUB cback (minx!, maxx!, slope!, intercept!)
DECLARE SUB ircomp (warningbeep%)
DECLARE SUB readbasdata (warningbeep%)
DECLARE SUB basin (warningbeep%)
DECLARE SUB drawline (colorold%(), intercept!, slope!)
DECLARE SUB ratecon ()
DECLARE SUB semi (warningbeep%)
DECLARE SUB info (warningbeep%)
DECLARE SUB bsub (warningbeep%)
DECLARE SUB readdata (warningbeep%)
DECLARE SUB dirwindow (warningbeep%)
DECLARE SUB aqdata (warningbeep%)
```

```
DECLARE SUB mainmenu (warningbeep%)
DECLARE SUB ScopeControlMenu ()
DECLARE SUB commandtoscope (CommandString$)
DECLARE SUB linleastsq (x!(), y!(), ndps!, slope!, intercept!, corr!)
DECLARE SUB dataaq (warningbeep%)
DECLARE SUB dataman (warningbeep%)
DECLARE SUB writefile (warningbeep%)
DECLARE SUB locandpr (lin!, column!, word$, Number!, Fore!, back!)
DECLARE SUB waiting (time!)
DECLARE SUB comminput (lin!, column!, Spaces!, stg$, Number!)
DECLARE SUB graph (x!(), y!(), ndpts!, xlabel$, ylabel$)
DECLARE SUB minmax (x!(),y !(),ndpts!,minx!,maxx!,miny!,maxy!,xminc!,xmaxc!)
DECLARE SUB average (Avg!(), ndps!, Av!)
DECLARE SUB arraycalc (a(), b(), VG(), n)
DECLARE SUB prcomm (comm$)
DECLARE SUB normalize (z(), ndps, norm)
DECLARE SUB clean ()
DECLARE SUB setuptables (VG(), TD())
DECLARE SUB initializescope ()
DECLARE SUB getdataarray (c$, ndps, xr())
DECLARE SUB smooth (warningbeep%)
DECLARE SUB graphback (minx!, maxx!, slope!, intercept!, ccc!)
DECLARE SUB gamma ()

DIM curr!(2000), pot!(2000), sem!(2000), gma(1000), colorold%(1000)

'************************************************************************
'  Make variables available throughout the program
'************************************************************************
COMMON SHARED curr!(), pot!(), sem!(), dt!, ndps, getcall, path$, filename$
COMMON SHARED minx!, maxx!, gma!(), epa, epc, comment$, colorold%()
'************************************************************************
'  Provide enough stack space for multiple calls
'************************************************************************
CLEAR , , 4000
'************************************************************************
'  Sets up screen type (VGA in this case)
'************************************************************************
SCREEN 9
'************************************************************************
'  List of default parameters
'************************************************************************
path$ = "c:\data"
filename$ = "gcq1"
comment$ = "Headerline to annotate data file.."
'************************************************************************
'  Goto the main menu
'************************************************************************
```

```
111     CALL mainmenu(warningbeep%)
'*************************************************************************
'  Exit the program
'*************************************************************************
GOSUB exit.program
'*************************************************************************
'  Displays the error which has occured to the screen and resumes
'  at the main program
'*************************************************************************
Error.Report:
    CALL prcomm("Error # " + LTRIM$(STR$(ERR)) + " Occurred")
    HAVEdata$ = "no"
    CALL waiting(3)
    CLOSE
    RESUME 111 'resume 80 return to main program
'*************************************************************************
'  Determines if Scope is not responding
'*************************************************************************
TimeOut:
     CALL prcomm("Time out occurred....")
     TimeOutCount = TimeOutCount + 1
     IF TimeOutCount = 5 THEN
      TimeOutCount = 0
      CALL prcomm("5 Time Outs.. ReInitialize Scope and Try Again")
      CALL aqdata(warningbeep%) 'GOTO 80
     END IF
RETURN
'*************************************************************************
'  End of the main program
'*************************************************************************
exit.program:
    CLOSE
    END
'*************************************************************************
'*************************************************************************


'=======================================
'  This subroutine is designed to aquire data from the LeCroy.
'  It is essentially the same as that in the main of the TA program.
'  This is still incomplete
'=======================================
'  Arrays defined are as follows:
'    VG()       : vertical gain conversion factors
'    TD()       : time/point conversion factors
'    x()        : temporary data array
'    CHAN1()    : averaged, data in volts after conversion from
'                 channel 1 (current)
'    C1DESC()   : channel 1 waveform descriptors
```

```
'    CHAN2()    : array containing channel 2 data (potential)
'    C2DESC()   : channel 2 waveform descriptors
'    t()        : array containing times for each data point for graph
'=========================================
SUB aqdata (warningbeep%)
DIM VG!(100), TD!(100), x!(2000), CHAN1!(2000), C1DESC!(200)
DIM C2DESC!(200), CHAN2!(2000), T!(2000)
IF getcall > 0 THEN
   IF getcall = 1 THEN GOTO getcall1:
   IF getcall = 2 THEN GOTO getcall2:
   IF getcall = 3 THEN GOTO getcall3:
   IF getcall = 4 THEN GOTO getcall4:
END IF
' Declare % as the trailer character (end scope transmit)
CPRM$ = "%"
   OPEN "COM1:9600,N,8,1" FOR RANDOM AS #1 LEN = 4096
   CALL initializescope
   CALL initializescope
' Set up arrays for conversion of vertical gain and time/point
  CALL setuptables(VG(), TD())
' initialize array
FOR i = 1 TO C1NDPS
  CHAN1(i) = CHAN2(i) = 0
NEXT i
'  Get channel 1 waveform descriptor and store in array C1DESC()
  getcall = 2
  read$ = "READ,C1.DE"
'  Point of return from TimeOut call
getcall2:
   CALL prcomm("Reading C1 Waveform Desc..")
   CALL getdataarray(read$, Trash, C1DESC())
' Determine # of data points  TNDP = C1DESC(23) * 10
' and interval required for approx 700 data pts for ouput
' to graphics screen (ndpg)
       ndpg = 70
       intvl = (C1DESC(23) / ndpg)
       intvl = FIX(intvl)
       IF intvl < 1 THEN intvl = 1
       intvl$ = LTRIM$(STR$(intvl))
'Go get sequence data
getcall = 1
SequenceCount = 0
  WHILE SequenceCount < NumAvg
   read$ = "READ,C1.DA,"+intvl$+",,,"+LTRIM$(STR$(SequenceCount+1))
' point of return from TimeOut call
getcall1:
   CALL prcomm("Reading C1")
   CALL getdataarray(read$, C1NDPS, x())
```

```
' Add each sequence array to an average array
    FOR j = 1 TO C1NDPS
      CHAN1(j) = CHAN1(j) + x(j)
    NEXT j
  SequenceCount = SequenceCount + 1
  WEND
'  Get channel 2 waveform descriptor and store in array C2DESC()
  getcall = 4
  read$ = "READ,C2.DE"
' Point of return from TimeOut call
getcall4:
   CALL prcomm("Reading C2 Waveform Desc..")
   CALL getdataarray(read$, Trash, C2DESC())
'  Get Data from Channel 2
   getcall = 3
   SequenceCount = 0
   WHILE SequenceCount < NumAvg
    read$ = "READ,C2.DA,"+intvl$+",,,"+LTRIM$(STR$(SequenceCount+1))
' Point of return from time out
getcall3:
    CALL prcomm("Reading C2")
    CALL getdataarray(read$, C2NDPS, x())
    FOR i = 1 TO C2NDPS
      CHAN2(i) = CHAN2(i) + x(i)
    NEXT i
  SequenceCount = SequenceCount + 1
   WEND
getcall = 0  'msf finished
CLOSE #1
normalize:
'  Normalize the averaged arrays and convert to volts
    CALL prcomm("Normalizing, and converting arrays.")
    CALL normalize(CHAN1(), C1NDPS, NumAvg)
    CALL normalize(CHAN2(), C2NDPS, NumAvg)
    CALL arraycalc(CHAN1(), C1DESC(), VG(), C1NDPS)
    CALL arraycalc(CHAN2(), C2DESC(), VG(), C2NDPS)
end.data.acquire:
' calculate time array from time/point data
' loop returns a time array calibratedin microseconds
Calibration = TD(C1DESC(10)) ' 10 is location of time/point in C1DESC()
HAVEdata$ = "yes"
'=========================================
END SUB
'=========================================
'  This subroutine to convert array values to absolute terms
'    A() : contains input and output data
'    B() : contains parameters from scope
'    C() : table that contains conversion for vgain
```

```
'     N  : is the number of data points'
'     VGAIN  : is the vertical gain
'     VVGAIN : is the variable vertical gain
'     VOFF   : is the vertical offset
'     Equation used for calculation comes from LeCroy DSO manual p. 7-49'
'     V = VGAIN*((data - 128)/32 - (VOFF - 200)/25)*200/(VVGAIN + 80)
'=========================================
SUB arraycalc (a(), b(), c(), n)
    qq = b(0)
    vgain = c(qq)
    vvgain = b(1)
    voff = b(5)
    LOCATE 21, 12
    FOR k = 1 TO n
    a(k) = vgain*((a(k)-128)/32-(voff-200)/25)*200/(vvgain + 80)
    NEXT k
'=========================================
END SUB
'=========================================
'  This subroutine is designed to calculate average of an array
'=========================================
SUB average (Avg(), ndps, Av)
 FOR i = 1 TO ndps
   total = Avg(i) + total
 NEXT i
Av = total / ndps
'=========================================
END SUB
'=========================================
'  This subroutine is a submenu of the main menu designed to allow
'  one to read data which was obtained from the BAS-100, perform IR
'  compensation and to save the data in the program's normal format.
'  Other options include changing the path, changing the filename,
'  listing the contents (*.DAT) of the directory specified by the
'  path, displaying comments associated with the current data,
'  moving to the data manipulation submenu or moving back to the
'  main menu
'=========================================
SUB basin (warningbeep%)
CLS
'  Set up command menu in cyan
16 '12
key1$ = "Path": KEY 1, key1$ + CHR$(13)
key2$ = "FileN": KEY 2, key2$ + CHR$(13)
key3$ = "Dir": KEY 3, key3$ + CHR$(13)
key4$ = "Read": KEY 4, key4$ + CHR$(13)
key5$ = "Write": KEY 5, key5$ + CHR$(13)
key6$ = "IR": KEY 6, key6$ + CHR$(13)
```

```
key7$ = "": KEY 7, key7$ + CHR$(13)
key8$ = "Comm": KEY 8, key8$ + CHR$(13)
key9$ = "Manip": KEY 9, key9$ + CHR$(13)
key10$ = "Back": KEY 10, key10$ + CHR$(13)
COLOR 11, 0: KEY ON: COLOR 15, 0
' Print Headerline
CALL locandpr(1, 20, "FCV Program version 1.2. June 1991", 0, 15, 0)
CALL locandpr(2, 31, "BAS Data Input", 0, 15, 0)
'  Print Statements
CALL locandpr(19, 1, "Path: ", 0, 14, 0)
CALL locandpr(19, 25, "Filename: ", 0, 14, 0)
CALL locandpr(21, 1, "Comment: ", 0, 14, 0)
CALL locandpr(23, 1, "Program Status: ", 0, 14, 0)
' Print Values of Program Parameters
CALL locandpr(19, 7, path$, 0, 15, 0)
CALL locandpr(19, 35, filename$, 0, 15, 0)
CALL locandpr(21, 10, comment$, 0, 15, 0)
CALL info(warningbeep%)
17 CALL prcomm("Hit a function key....")
  INPUT ; "", comm$: CALL prcomm("")
    SELECT CASE comm$
      CASE key1$
        CALL comminput(19, 7, 11, path$, 0)
        CHAN1$ = ""
        GOTO 17
      CASE key2$
        CALL comminput(19, 35, 12, filename$, 0)
        GOTO 17
      CASE key3$
         CALL dirwindow(warningbeep%)
         GOTO 17
      CASE key4$
        CALL prcomm("Scan Rate in V-s-1"): INPUT scanr
        KEY OFF
        CLS 0
        CALL readbasdata(warningbeep%)
        dt = ABS(pot(1) - pot(2)) / scanr
        GOTO 16
      CASE key5$
        CALL writefile(warningbeep%)
        GOTO 17
      CASE key6$
        CALL ircomp(warningbeep%)
        GOTO 17
      CASE key7$
        GOTO 17
      CASE key8$
        CALL comminput(21, 10, 40, comment$, 0)
```

```
      GOTO 17
    CASE key9$
      KEY OFF
      CALL dataman(warningbeep%)
      GOTO 16
    CASE key10$
      KEY OFF
      CLS 0
      GOTO qt.subr:
  CASE ELSE
   CHAN1$ = ""
   BEEP
   CALL prcomm("Wrong key...")
   CALL waiting(1)
  END SELECT
  GOTO 16
qt.subr:
'=========================================
END SUB
'=========================================
'  This subroutine is designed to allow the user to approximate the
'  the background of a CV by moving markers associated with the
'  forward and reverse scans. The user is then given the option to
'  perform a background subtraction based on the approximation
'=========================================
SUB bsub (warningbeep%)
'  A 2x2 matrix which describes the position of the 4 markers. The
'  first term in the parenteses represents the scan (ie forward or
'  reverse, the second term describes the side on which the marker
'  will be placed
DIM squar(2, 2)'  Determine max and mins associated with the data
CALL minmax(pot(), curr(), ndps, minx, maxx, miny, maxy, xminc, xmaxc)
'Determine initial direction of potential scan
 IF pot(10) - pot(5) > 0 THEN
    eswitchc = xmaxc   'if initial scan is positive
 ELSE                  ' swithing potential will be largest potential
    eswitchc = xminc
 END IF'  Divisions to be used for drawing and moving squares
   dy = ABS(maxy - miny) / 100
   dx = ABS(maxx - minx) / 200
'  Initial step size for moving markers and the initial scan to move
ste = 5
scan = 1
'  Define the horizontal positioning of the markers on either side of
'  the data
xposr = maxx + 10 * dx
xposl = minx - 10 * dx
```

```
' Define the matrix value to signify right and left marker of current
' scan
lrr = 2
lrl = 1
' Define initial vertical positions of the markers where the first
squar(1, lrl) = curr(ndps / 2 - 4)
squar(1, lrr) = curr(4)
squar(2, lrl) = curr(ndps / 2 + 4)
squar(2, lrr) = curr(ndps - 4)
' Display all 4 markers and make scan 1 current
xpos = xposl
CALL movesquare(xpos, squar(1, 1), dx, dy, ste)
lsqold = squar(1, lrl)
CALL movesquare(xpos, squar(2, 1), dx, dy, ste)
 xpos = xposr
CALL movesquare(xpos, squar(1, 2), dx, dy, ste)
 rsqold = squar(1, lrr)
CALL movesquare(xpos, squar(2, 2), dx, dy, ste)
' Determine slope and intercept of the line which passes through
' the left and right markers associated with current scan
  CALL slopeintercept(xposl, lsqold, xposr, rsqold, slope, intercept)
' Save the screen colors which will be covered when the line between
' the two markers is drawn, then procede to draw the line
  CALL drawline2(xposl, lsqold, xposr, rsqold, slope, intercept)
' Enter loop which allows the user to move the right and left marker
' up and down (right (U/D), left (ALT-U/ALT-D), change the speed with
' which the markers are moved (0-9), toggle between the current scan
' (T), perform the background subtraction (S), or escape without
' changes (ESC)
DO
 k$ = INKEY$
'current right up "U"
 IF UCASE$(k$) = CHR$(85) THEN
   sted = ste
'restore old colors
'move square
   CALL restorel(xposl, lsqold, xposr, rsqold, slope, intercept)
   CALL movesquare(xposr, squar(scan, lrr), dx, dy, sted)
   rsqold = squar(scan, lrr)
'determine new slope and intercept
   CALL slopeintercept(xposl, lsqold, xposr, rsqold, slope, intercept)
'save colors to be covered
'draw line with lsqold and rsqold
   CALL drawline2(xposl, lsqold, xposr, rsqold, slope, intercept)
 END IF
'current right down "D"
 IF UCASE$(k$) = CHR$(68) THEN
   sted = -ste
```

```
'restore old colors
'move square
   CALL restorel(xposl, lsqold, xposr, rsqold, slope, intercept)
   CALL movesquare(xposr, squar(scan, lrr), dx, dy, sted)
   rsqold = squar(scan, lrr)
'determine new slope and intercept
   CALL slopeintercept(xposl, lsqold, xposr, rsqold, slope, intercept)
'save colors to be covered
'draw line with lsqold and rsqold
   CALL drawline2(xposl, lsqold, xposr, rsqold, slope, intercept)
 END IF
 'current left up "ALT-U"
 IF k$ = CHR$(0) + CHR$(22) THEN
   sted = ste
'restore old colors
'move square
   CALL restorel(xposl, lsqold, xposr, rsqold, slope, intercept)
   CALL movesquare(xposl, squar(scan, lrl), dx, dy, sted)
   lsqold = squar(scan, lrl)
'determine new slope and intercept
   CALL slopeintercept(xposl, lsqold, xposr, rsqold, slope, intercept)
'save colors to be covered
'draw line with lsqold and rsqold
   CALL drawline2(xposl, lsqold, xposr, rsqold, slope, intercept)
 END IF
'current left down "ALT-D"
 IF k$ = CHR$(0) + CHR$(32) THEN
   sted = -ste
'restore old colors
'move square
   CALL restorel(xposl, lsqold, xposr, rsqold, slope, intercept)
   CALL movesquare(xposl, squar(scan, lrl), dx, dy, sted)
   lsqold = squar(scan, lrl)
'determine new slope and intercept
   CALL slopeintercept(xposl, lsqold, xposr, rsqold, slope, intercept)
'save colors to be covered
'draw line with lsqold and rsqold
   CALL drawline2(xposl, lsqold, xposr, rsqold, slope, intercept)
 END IF
'if T then toggel between forward and reverse scan
 IF UCASE$(k$) = CHR$(84) THEN
   IF scan = 1 THEN scan = 2 ELSE scan = 1
   rsqold = squar(scan, lrr)
   lsqold = squar(scan, lrl)
'save colors to be covered
'draw line with lsqold and rsqold
   CALL drawline2(xposl, lsqold, xposr, rsqold, slope, intercept)
 END IF
```

```
'if 0 through 9 are pressed adjust ste
  IF "/" < k$ AND k$ < ":" THEN
    ste = ASC(k$) - 48
    LOCATE 24, 30: PRINT "Step speed: ";
    PRINT ste;
  END IF
'if ESC is pressed then redraw and exit
  IF char$ = CHR$(27) THEN
    LOCATE 24, 30: PRINT "                ";
    CALL graph(pot(), curr(), ndps, "E/V", "i/uA")
    CALL info(warningbeep%)
    EXIT DO
  END IF
'if s is pressed, subtract background
  IF char$ = CHR$(115) THEN
   LOCATE 24, 30: PRINT "                ";
   FOR i = 1 TO eswitchc
     curr(i) = curr(i) - (pot(i) * slope + intercept)
   NEXT i
   FOR i = eswitchc TO ndps
     curr(i) = curr(i) - (pot(i) * slope + intercept)
  NEXT i        'redraw graph after background subtraction and exit
    CALL graph(pot(), curr(), ndps, "E/V", "i/uA")
    CALL info(warningbeep%)
    EXIT DO
  END IF
LOOP
LOCATE 23, 17: PRINT SPACE$(40): LOCATE 24, 17: PRINT SPACE$(40);
'=========================================
END SUB
'=========================================
'   This subroutine is used in the background subtraction to erase
'  a line which has been drawn before the screen colors are restored
'=========================================
SUB cback (minx, maxx, slope, intercept)
  'clear previous background
    PSET (minx, minx * slope + intercept)
    LINE -(maxx, maxx * slope + intercept), 0
'=========================================
END SUB
'=========================================
'   This subroutine clears comment window
'=========================================
SUB clean
  LOCATE 24, 1: PRINT SPC(75);
'=========================================
END SUB
'=========================================
```

```
' This subroutine will send a general command string to the DSO
' which is opened as COM1:
'=========================================
SUB commandtoscope (CommandString$)
  PRINT #1, CHR$(27) + "R"; CommandString$; CHR$(27) + "L"
'=========================================
END SUB
'=========================================
' This subroutine is designed to accept input in the form of a
' string or a number at the position where the current value is
' displayed and display the new value at that same position.
' Examples where this is used is in changing the path or filename
'=========================================
SUB comminput (lin, column, Spaces, stg$, Number)
IF Number = 0 THEN
   LOCATE lin, column
   PRINT SPC(Spaces);
   LOCATE lin, column
   INPUT ; "", stg$
   GOTO finished
END IF
   LOCATE lin, column
   PRINT SPC(Spaces);
   LOCATE lin, column
   INPUT ; "", Number
finished:
'=========================================
END SUB
'=========================================
' This subroutine is a submenu of the main menu designed for the
' aquisition of data from the LeCroy. Unique options include:
' specifying the current amplifier settings, aquisition of data
' and reinitializing the scope. This routine is incomplete
'=========================================
SUB dataaq (warningbeep%)
CLS
amp = 96.97    'assume 96.97 uAmp/volt for ouput1
AmpOut = 1
NumAvg = 1
' Set up command menu in cyan
90
key1$ = "Path": KEY 1, key1$ + CHR$(13)
key2$ = "FileN": KEY 2, key2$ + CHR$(13)
key3$ = "IOut": KEY 3, key3$ + CHR$(13)
key4$ = "GetDA": KEY 4, key4$ + CHR$(13)
key5$ = "Comm": KEY 5, key5$ + CHR$(13)
key6$ = "Write": KEY 6, key6$ + CHR$(13)
key7$ = "": KEY 7, key7$ + CHR$(13)
```

```
key8$ = "": KEY 8, key8$ + CHR$(13)
key9$ = "": KEY 9, key9$ + CHR$(13)
key10$ = "Main": KEY 10, key10$ + CHR$(13)
COLOR 11, 0: KEY ON: COLOR 15, 0
' Print Headerline
CALL locandpr(1, 20, "FCV Program version 1.2. June. 1991", 0, 15, 0)
'  Print Statements
6 CALL locandpr(19, 1, "Path: ", 0, 14, 0)
CALL locandpr(19, 19, "Filename: ", 0, 14, 0)
CALL locandpr(19, 47, "I_Amp (uA/V): ", 0, 14, 0)
CALL locandpr(19, 36, "Out: ", 0, 14, 0)
CALL locandpr(21, 1, "Comment: ", 0, 14, 0)
CALL locandpr(23, 1, "Program Status: ", 0, 14, 0)
' Print Values of Program Parameters
CALL locandpr(19, 7, path$, 0, 15, 0)
CALL locandpr(19, 29, filename$, 0, 15, 0)
CALL locandpr(19, 60, "", ABS(amp), 15, 0)
CALL locandpr(19, 40, "", AmpOut, 15, 0)
CALL locandpr(21, 10, comment$, 0, 15, 0)
CALL locandpr(19, 72, "   ", 0, 15, 0)
100
CALL prcomm("Hit a function key....")
 INPUT ; "", comm$: CALL prcomm("")
  SELECT CASE comm$
    CASE key1$
      CALL comminput(19, 7, 11, path$, 0)
      CHAN1$ = ""
    CASE key2$
      CALL comminput(19, 24, 12, filename$, 0)
      CHAN1$ = ""
    CASE key3$
       CALL prcomm("Enter 1 for Out1 or 2 for Out2 ?  ")
       INPUT ; "", AmpOut
       IF AmpOut = 1 OR AmpOut = 0 THEN
         amp = 96.97 'uA/V
         AmpOut = 1
       ELSE
         CALL prcomm("Enter value on 10 turn pot (10.00-0.00) ?  ")
         INPUT ; "", tur
         amp = -96.99 / (1 + .5 * tur)
         AmpOut = 2
       END IF
       CHAN1$ = ""
    CASE key4$
      CHAN1$ = "yes"
      CALL aqdata(warningbeep%)
    CASE key5$
      CALL comminput(21, 10, 40, comment$, 0)
```

```
      GOTO 100
    CASE key6$
      CALL writefile(warningbeep%)
      CHAN1$ = ""
    CASE key7$
      CHAN1$ = ""
    CASE key8$
     CHAN1$ = ""
    CASE key9$
      CHAN1$ = ""
    CASE key10$
      KEY OFF
      CLS 0
      GOTO quit.subroutine
  CASE ELSE
   CHAN1$ = ""
   BEEP
   CALL prcomm("Wrong key...")
   CALL waiting(1)
  END SELECT
   KEY OFF
   CLS 0
   GOTO 90
quit.subroutine:
'=========================================
END SUB
'=========================================
'  This subroutine is a submenu which can be entered from the main
'  menu or the basin submenu. It is designed to allow the user to
'  manipulate data files. Unique options include data smoothing,
'  background subtraction and semi-integral analysis.
'=========================================
SUB dataman (warningbeep%)
CLS
'if there is data in the array then graphit!
 IF curr(1) < > 0 THEN
    CALL graph(pot(), curr(), ndps, "E/V", "i/uA")
    CALL info(warningbeep%)
 END IF
'  Set up command menu in cyan
12 KEY OFF
key1$ = "Path": KEY 1, key1$ + CHR$(13)
key2$ = "FileN": KEY 2, key2$ + CHR$(13)
key3$ = "Dir": KEY 3, key3$ + CHR$(13)
key4$ = "Read": KEY 4, key4$ + CHR$(13)
key5$ = "Write": KEY 5, key5$ + CHR$(13)
key6$ = "Smoth": KEY 6, key6$ + CHR$(13)
key7$ = "Bsub": KEY 7, key7$ + CHR$(13)
```

```
key8$ = "Comm": KEY 8, key8$ + CHR$(13)
key9$ = "Semi": KEY 9, key9$ + CHR$(13)
key10$ = "Back": KEY 10, key10$ + CHR$(13)
COLOR 11, 0: KEY ON: COLOR 15, 0
' Print Headerline
CALL locandpr(1, 20, "FCV Program version 1.2. June 1991", 0, 15, 0)
CALL locandpr(2, 31, "Data Manipulation", 0, 15, 0)
'  Print Statements
CALL locandpr(19, 1, "Path: ", 0, 14, 0)
CALL locandpr(19, 25, "Filename: ", 0, 14, 0)
CALL locandpr(21, 1, "Comment: ", 0, 14, 0)
CALL locandpr(23, 1, "Program Status: ", 0, 14, 0)
' Print Values of Program Parameters
CALL locandpr(19, 7, path$, 0, 15, 0)
CALL locandpr(19, 35, filename$, 0, 15, 0)
CALL locandpr(21, 10, comment$, 0, 15, 0)
11 CALL prcomm("Hit a function key....")
  INPUT ; "", comm$: CALL prcomm("")
    SELECT CASE comm$
      CASE key1$
        CALL comminput(19, 7, 11, path$, 0)
        CHAN1$ = ""
        GOTO 11
      CASE key2$
        CALL comminput(19, 35, 12, filename$, 0)
        GOTO 11
      CASE key3$
         CALL dirwindow(warningbeep%)
         GOTO 11
      CASE key4$
        KEY OFF
        CLS 0
        CALL readdata(warningbeep%)
        GOTO 12
      CASE key5$
        CALL writefile(warningbeep%)
        GOTO 11
      CASE key6$
        CALL smooth(warningbeep%)
        GOTO 11
      CASE key7$
        CALL bsub(warningbeep%)
        GOTO 11
      CASE key8$
        CALL comminput(21, 10, 40, comment$, 0)
        GOTO 11
      CASE key9$
        KEY OFF
```

```
        CALL semi(warningbeep%)
        GOTO 12
      CASE key10$
        KEY OFF
        CLS 0
        GOTO quit.subr:
      CASE ELSE
        CHAN1$ = ""
        BEEP
        CALL prcomm("Wrong key...")
        CALL waiting(1)
    END SELECT
     GOTO 12
quit.subr:
'=========================================
END SUB
'=========================================
' This subroutine is designed to display the contents (*.DAT) of
' the directory specified by the current path (path$)'
'=========================================
SUB dirwindow (warningbeep%)
  DIM x$(500)
' Send DIR DOS command to list *.dat into a temporary file "tempfile"
  SHELL "dir " + path$ + "\*.dat > tempfile"
' open the temporary file, read its contents, close and kill it
  OPEN "tempfile" FOR INPUT AS #3
  count% = 0
  WHILE NOT EOF(3)
       LINE INPUT #3, x$(count%)
       count% = count% + 1
  WEND
  CLOSE #3
  KILL "tempfile"
' isolate the needed data obtained from the temporary file
' (ie. just the filename prefixes), and display them on screen
j = 4
FOR i = 4 TO (count% - 2) STEP 5
  LOCATE j, 5
  PRINT LEFT$(x$(i), 8), LEFT$(x$(i + 1), 8), LEFT$(x$(i + 2), 8), LEFT$(x$(i + 3),
        8), LEFT$(x$(i + 4), 8)
  j = j + 1
NEXT i
'=========================================
END SUB
'=========================================
' This subroutine is designed to save the screen colors which will
' be covered when a line is drawn, and to draw the line
'=========================================
```

```
SUB drawline (colorold%(), intercept, slope)
  FOR i = 1 TO ndps / 2 STEP 2
    y = intercept + slope * pot!(i)
    colorold%(i) = POINT(pot!(i), y)
    PSET (pot!(i), y), 15
  NEXT
'=========================================
END SUB
'=========================================
'  This subroutine is a modified form of SUB drawline which does
'  essentially the same thing but allows the use of the LINE
'  statement instead of PSET alone
'=========================================
SUB drawline2 (x1, y1, x2, y2, slope, intercept)
'save colors overwhich line will be drawn
FOR i = 1 TO ndps / 2
  y = intercept + slope * pot!(i)
  colorold%(i) = POINT(pot!(i), y)
NEXT
'draw line
  PSET (x1, y1), 15
  LINE -(x2, y2), 15, , &H9999
'=========================================
END SUB
'=========================================
'  This subroutine calculates values of Gamma and places them into
'  an array to be used during semi-integration
'=========================================
SUB gamma
  gma!(0) = 1.7725
  FOR i = 1 TO 1000 'ndps / 2
    Factorial = (2 * i - 1) / (2 * i)
    gma!(i) = Factorial * gma!(i - 1)
  NEXT
'=========================================
END SUB
'=========================================
'  This subroutine is from the TA program and is used during data
'  aquisition.
'=========================================
SUB getdataarray (c$, count, xr())
Begin.Read:
' Send read command to scope
    PRINT #1, c$
   ON TIMER(1) GOSUB TimeOut
    TIMER ON
    Cycle = 1
' Begin big loop for downloading character string from scope
```

```
    WHILE Cycle < > 0
' Enable the scope for transmission via ACK command
    PRINT #1, CHR$(6);
' Wait for characters to arrive from scope
    WHILE EOF(1)
    WEND
    TIMER OFF
      a$ = INPUT$(LOC(1), #1)
      c$ = MID$(a$, 1, LEN(a$))
'Check for end of transmission "%" prompt.
      L = INSTR(c$, "%")
     IF L > 0 THEN
        L = L - 1
        c$ = MID$(a$, 1, L)
        Cycle = 0
      END IF
       Avg$ = Avg$ + c$
    WEND
IF Avg$ = "" THEN GOTO Begin.Read
IF Avg$ = CHR$(13) THEN GOTO Begin.Read
'This section of the subroutine
'converts string data to numeric data.
'Check first ascii character of AVG$ to see if it is a "#".
'If it is a "#" then see if next charcter is a "L" or an "I".
'If "i" stop.  If "L" then get the value n and the ",".
'Read each number that follows and asign the value to the array X.
'Read in next block and add each value to X.
'When #I is reached calculate average value for array X.
count = 0
NEXT.BLOCK:
   z$ = LEFT$(Avg$, 1)
'  Get rid of garbage in string.
  WHILE z$ < > "#"
    Avg$ = RIGHT$(Avg$, (LEN(Avg$) - 1))
    z$ = LEFT$(Avg$, 1)
  WEND
'  Test first character and see if it is a "#".
  IF z$ = "#" THEN
'  Get rid of "#".
      Avg$ = RIGHT$(Avg$, (LEN(Avg$) - 1))
      z$ = LEFT$(Avg$, 1)
'  If it was a #, check next for an L or I.
      IF z$ = "I" GOTO END.OF.STRING
      IF z$ = "L" THEN
'  Get rid of "L,".
      Avg$ = RIGHT$(Avg$, (LEN(Avg$) - 2))
'  Get the number of data points, NDP.
      NDP = VAL(Avg$)
```

```
' Get rid of NDP and the ",".
    z$ = LEFT$(Avg$, 1)
    WHILE z$ < > ","
      Avg$ = RIGHT$(Avg$, (LEN(Avg$) - 1))
      z$ = LEFT$(Avg$, 1)
    WEND
    Avg$ = RIGHT$(Avg$, (LEN(Avg$) - 1))
' Read in data values and store them in the array X.
    FOR i = 1 TO NDP
      TEMP = VAL(Avg$)
      xr(count) = TEMP
      count = count + 1
' Pop off values after they have been stored in array X.
      z$ = LEFT$(Avg$, 1)
' Get rid of last value.
      WHILE z$ < > ","
        IF LEN(Avg$) = 0 THEN GOTO END.OF.STRING
        Avg$ = RIGHT$(Avg$, (LEN(Avg$) - 1))
        z$ = LEFT$(Avg$, 1)
      WEND
' Get rid of ",".
      Avg$ = RIGHT$(Avg$, (LEN(Avg$) - 1))
    NEXT i
    END IF
' Keep track of the number of blocks read.
   GOTO NEXT.BLOCK
  END IF
  GOTO NEXT.BLOCK
END.OF.STRING:
count = count - 1
'=========================================
END SUB
'=========================================
' This subroutine is designed to graph data including
' raw data, background subtracted data, and semi
' intigrated data
'=========================================
SUB graph (x(), y(), n, xlabel$, ylabel$)
' initialize flags
   semFlag = 0: RateFlag = 0
' determine what data we have
IF y(1) + y(2) + y(3) = sem!(1) + sem!(2) + sem!(3) THEN
  semFlag = 1
ELSEIF y(1) + y(2) + y(3) < > curr!(1) + curr(2) + curr(3) THEN
  RateFlag = 1
END IF
' get minimum and maximum values of x and y arrays
CALL minmax(x(), y!(), n, minx, maxx, miny, maxy, xminc, xmaxc)
```

```
' determine the graph scale min and max
IF ABS(miny) > maxy THEN
  maxy = ABS(miny)
ELSE
  miny = -maxy
END IF
'  set colors
ccolor = 2
gcolor = 3
'get difference between minimum and maximum x values for tics, etc
diffx = ABS(maxx - minx)
diffy = ABS(maxy - miny)
ticx = diffx / 8
ticy = diffy / 8
'define viewport on screen
VIEW (70, 30)-(570, 220)
'set scale to natural coordinates
'clear the graphics viewport
WINDOW (minx - ticx, maxy + ticy)-(maxx + ticx, miny - ticy)
IF semFlag = 0 AND RateFlag = 0 THEN CLS
'draw graph window
PSET (minx - ticx, maxy + ticy)
LINE -(minx - ticx, miny - ticy), ccolor
LINE -(maxx + ticx, miny - ticy), ccolor
LINE -(maxx + ticx, maxy + ticy), ccolor
LINE -(minx - ticx, maxy + ticy), ccolor
'draw in x tics
FOR i = 0 TO 4
  PSET ((minx + ticx + (ticx * 2 * i)), miny - ticy)
  LINE -((minx + ticx + (ticx * 2 * i)), (miny - (ticy / 1.3))), ccolor
NEXT i
'print x-scale
LOCATE 17, 8: PRINT USING "##.##"; minx - ticx
LOCATE 17, 21: PRINT USING "##.##"; minx + ticx
LOCATE 17, 33: PRINT USING "##.##"; minx + 3 * ticx
LOCATE 17, 46: PRINT USING "##.##"; minx + 5 * ticx
LOCATE 17, 58: PRINT USING "##.##"; minx + 7 * ticx
LOCATE 17, 71: PRINT USING "##.##"; maxx + ticx
'print x axis label
COLOR 15
LOCATE 18, 43: PRINT xlabel$;
'print y-scale
COLOR 10
IF semFlag = 1 THEN LOCATE 4, 10: PRINT USING "##.##"; sem!(ndps / 2)
'specify data color based on the data you have
IF semFlag = 1 THEN gcolor = 10
IF RateFlag = 1 THEN gcolor = 14
'plot graph based on data you have
```

```
PSET (x(1), y(1))
IF RateFlag = 1 THEN
  FOR i = 1 TO n - 1 STEP 2
    IF y(i) < > 0 THEN PSET (x(i), y(i)), gcolor
  NEXT i
ELSEIF semFlag = 1 THEN
  FOR i = 1 TO n - 1 STEP 4
    FOR j = 0 TO 2
      LINE -(x(i + j), y(i + j)), gcolor
    NEXT j
    FOR j = 2 TO 4
      LINE -(x(i + j), y(i + j)), 0
    NEXT j
  NEXT i
ELSE
  FOR i = 1 TO n - 1
    LINE -(x(i), y(i)), gcolor
  NEXT i
END IF
'==========================================
END SUB
'==========================================
' This subroutine is designed to plot the background estimate
'==========================================
SUB graphback (minx, maxx, slope, intercept, ccc)
  PSET (minx, minx * slope + intercept)
  LINE -(maxx, maxx * slope + intercept), 15, , ccc
'==========================================
END SUB
'==========================================
' This subroutine is designed to display peak currents, peak
' potentials, peak separation, formal potential and scan rate
'==========================================
SUB info (warningbeep%)
'initialize peak currents
ipa = curr(1)
ipc = curr(1)
'determine peak currents and peak potentials
FOR i = 1 TO ndps
   IF ipa > curr(i) THEN ipa = curr(i): epa = pot(i)
   IF ipc < curr(i) THEN ipc = curr(i): epc = pot(i)
NEXT i
' Print Statements
CALL locandpr(19, 50, "ipa:", 0, 14, 0)
CALL locandpr(19, 65, "ipc:", 0, 14, 0)
CALL locandpr(20, 50, "Epa:", 0, 14, 0)
CALL locandpr(20, 65, "Epc:", 0, 14, 0)
CALL locandpr(21, 50, "Eo':", 0, 14, 0)
```

```
CALL locandpr(21, 65, "dEp:", 0, 14, 0)
CALL locandpr(22, 50, "Scan rate:", 0, 14, 0)
' Print Values of Program Parameters
COLOR 15, 0
LOCATE 19, 55: PRINT USING "####.##"; ipa
LOCATE 19, 70: PRINT USING "####.##"; ipc
LOCATE 20, 55: PRINT USING "##.###"; epa
LOCATE 20, 70: PRINT USING "##.###"; epc
LOCATE 21, 55: PRINT USING "##.###"; (epa + epc) / 2
LOCATE 21, 70: PRINT USING "##.###"; ABS(epa - epc)
IF dt< >0 THEN LOCATE 22, 60: PRINT USING "##.###"; ABS(pot(1)-pot(2))/dt
'=========================================
END SUB
'=========================================
' This subroutine is designed to initialize the LeCroy and was
' obtained from the TA program
'=========================================
SUB initializescope
INITIALIZE:
   CPRM$ = "%"
   PRINT #1, CHR$(27); "["
   PRINT #1, "CHLP PPO"
   PRINT #1, "CTRL OFF"
   PRINT #1, "CFMT,L,BYTE,UNSIGNED_SHORT"
   PRINT #1, "CBLS 4096"
   PRINT #1, "MASK 6,1"  'Enable STB 1
   PRINT #1, "RS_CONF 6,13,0,0,0"   '<ACK>,<CR>
   PRINT #1, "CPRM " + CHR$(34) + CPRM$ + CHR$(34)
'=========================================
END SUB
'=========================================
' This subroutine is designed to perform IR compensation on data
' obtained from the BAS-100 and is used in basin
'=========================================
SUB ircomp (warningbeep%)
      CALL prcomm("Uncompensated Resistance (ohm) "): INPUT res
      FOR i = 1 TO ndps
        pot(i) = pot(i) + res * curr(i) / 1000000!
      NEXT i
      CALL minmax(pot(),curr(),ndps,minx,maxx,miny,maxy,xminc,xmaxc)
      CALL graph(pot(), curr(), ndps, "E/V", "i/uA")
      CALL info(warningbeep%)
'=========================================
END SUB
'=========================================
' This subroutine was obtained from the TA program and performs
' a linear least-square routine to determine slope and intercept
' I modified ndps to nd------charlie
```

```
' Subroutine calculates the least-squares fit of x.y data
' x() and y() are input arrays with data to be fitted to a line
' ndps is the number of data points
' Slope is the calculated slope
' Intercept is the calculated intercept
' Corr is the correlation coefficient (not implemented yet!)
'=========================================
SUB linleastsq (x(), y(), InitialN, slope, intercept, corr)
'Calculate required sums
FOR i = InitialN TO InitialN + 5
  sumx = sumx + x(i)
  sumy = sumy + y(i)
  sumxy = sumxy + (x(i) * y(i))
  sumxsq = sumxsq + (x(i) * x(i))
NEXT i
' Calculate required quantities
  Dee = (6 * sumxsq) - (sumx * sumx)
  slope = ((6 * sumxy) - (sumx * sumy)) / Dee
  intercept = ((sumxsq * sumy) - (sumx * sumxy)) / Dee
'=========================================
END SUB
'=========================================
' This subroutine was obtained from the TA program and prints either
' a string or an integer to the specified position on the screen and
' in the specified color
'=========================================
SUB locandpr (lin, column, word$, Number, Fore, back)
IF Number = 0 THEN
  COLOR Fore, back
  LOCATE lin, column
  PRINT word$;
  GOTO end.sub
END IF
  COLOR Fore, back
  LOCATE lin, column
  PRINT USING "###"; Number
end.sub:
'=========================================
END SUB
'=========================================
' This subroutine is the main menu which allows the user to access
' submenus
'=========================================
SUB mainmenu (warningbeep%)
CLS
33    'setup command menu
key1$ = "DataAq": KEY 1, key1$ + CHR$(13)
key2$ = "Manip": KEY 2, key2$ + CHR$(13)
```

```
key3$ = "BAS": KEY 3, key3$ + CHR$(13)
key4$ = "": KEY 4, key4$ + CHR$(13)
key5$ = "": KEY 5, key5$ + CHR$(13)
key6$ = "": KEY 6, key6$ + CHR$(13)
key7$ = "": KEY 7, key7$ + CHR$(13)
key8$ = "": KEY 8, key8$ + CHR$(13)
key9$ = "": KEY 9, key9$ + CHR$(13)
key10$ = "ExitP": KEY 10, key10$ + CHR$(13)
COLOR 11, 0: KEY ON: COLOR 15, 0
'print headline
CALL locandpr(1, 20, "FCV Program version 1.2. June 1991", 0, 15, 0)
CALL locandpr(2, 35, "Main Menu", 0, 15, 0)
CALL locandpr(23, 1, "Program Status: ", 0, 14, 0)
CALL locandpr(19, 72, "  ", 0, 15, 0)
55 CALL prcomm("Hit a function key....")
555  INPUT ; "", comm$: CALL prcomm("")
   SELECT CASE comm$
     CASE key1$
       KEY OFF
       CLS 0
       CALL dataaq(warningbeep%)
       GOTO 33
     CASE key2$
       KEY OFF
       CLS 0
       CALL dataman(warningbeep%)
       GOTO 33
     CASE key3$
       KEY OFF
       CLS 0
       CALL basin(warningbeep%)
       GOTO 33
     CASE key4$
       KEY OFF
       CLS 0
       GOTO 33
     CASE key5$
       KEY OFF
       CLS 0
       GOTO 33
     CASE key6$
       KEY OFF
       CLS 0
       GOTO 33
     CASE key7$
       KEY OFF
       CLS 0
       GOTO 33
```

```
      CASE key8$
        KEY OFF
        CLS 0
        GOTO 33
      CASE key9$
        KEY OFF
        CLS 0
        GOTO 33
      CASE key10$
        KEY OFF
        CLS 0
        CLOSE
        EXIT SUB
    CASE ELSE
      BEEP
      CALL prcomm("Wrong key...")
      CALL waiting(1)
    END SELECT
'=========================================
END SUB
'=========================================
' This subroutine is designed to determin the max and min of an x,y
' data array, and to determine the counter value associated with
' the max an min x values
'=========================================
SUB minmax (x(), y(), ndpts, minx, maxx, miny, maxy, xminc, xmaxc)
'initialize values
maxx = x(1)
minx = x(1)
maxy = y(1)
miny = y(1)
xmaxc = 1
xminc = 1
'determine values
FOR i = 2 TO ndpts
  IF x(i) > maxx THEN maxx = x(i): xmaxc = i
  IF x(i) < minx THEN minx = x(i): xminc = i
  IF y(i) > maxy THEN maxy = y(i)
  IF y(i) < miny THEN miny = y(i)
NEXT i
'=========================================
END SUB
'=========================================
' This subroutine is designed to move the marker used in the back-
' ground subtraction subroutine (bsub). It clears the current marker
' and draws the marker in the new position based on the specified
' step
'=========================================
```

```
SUB movesquare (xcorr, ycorr, dx, dy, ste)
'clear square
PSET (xcorr + 2 * dx, ycorr + 2 * dy), 0
LINE -(xcorr - 2 * dx, ycorr + 2 * dy), 0
LINE -(xcorr - 2 * dx, ycorr - 2 * dy), 0
LINE -(xcorr + 2 * dx, ycorr - 2 * dy), 0
LINE -(xcorr + 2 * dx, ycorr + 2 * dy), 0
'determine new y corrdinate
ycorr = ycorr + ste * dy
' draq square
PSET (xcorr + 2 * dx, ycorr + 2 * dy), 15
LINE -(xcorr - 2 * dx, ycorr + 2 * dy), 15
LINE -(xcorr - 2 * dx, ycorr - 2 * dy), 15
LINE -(xcorr + 2 * dx, ycorr - 2 * dy), 15
LINE -(xcorr + 2 * dx, ycorr + 2 * dy), 15
'=========================================
END SUB
'=========================================
' This subroutine was obtained from the TA program and normalizes an
' array
'    Subroutine to normalize an array for the number of averages
'      Z()  : input/output array
'      NDPS : number of data points in array
'      norm : the normalization factor
'=========================================
SUB normalize (z(), n, norm)
FOR i = 1 TO n
  z(i) = z(i) / norm
NEXT i
'=========================================
END SUB
'=========================================
' This subroutine was obtained from the TA program and is used to
' write a comment to the screen
'=========================================
SUB prcomm (comm$)
 LOCATE 23, 17: PRINT SPC(75);
 LOCATE 23, 17: PRINT comm$;
'=========================================
END SUB
'=========================================
'
'=========================================
SUB ratecon
DIM RateK(2000)
R = 8.31441: T = 298
n = 2: F = 96485
c = 1
```

```
E0! = (epa + epc) / 2
constant! = n * F / (R * T)
LOCATE 23, 17: PRINT SPACE$(40): LOCATE 24, 17: PRINT SPACE$(40);
COLOR 15
makesure:
LOCATE 23, 17: PRINT "Eo'=";
PRINT USING "##.###"; E0!;
LOCATE 23, 30: PRINT "n ="; n;
LOCATE 24, 20: PRINT "Correct? (Y/N)";
getkey: key$ = INKEY$: IF key$ = "" GOTO getkey
key$ = UCASE$(key$)
IF key$ = "N" THEN
LOCATE 23, 21: PRINT SPACE$(6): LOCATE 23, 21: INPUT "", E0!
LOCATE 23, 34: PRINT SPACE$(2): LOCATE 23, 34: INPUT "", n
'LOCATE 23, 17: PRINT SPACE$(40): LOCATE 24, 17: PRINT SPACE$(40);
GOTO makesure
END IF
'determine Ilforward and Ilback and adjust arrays
ini = 0
    seml1 = sem!(ndps / 2)
    seml2 = sem!(ndps) - seml1
FOR i = 1 TO ndps
  IF i >= ndps / 2 + 1 THEN
    sem!(i) = sem!(i) - seml2
  END IF
IF curr!(i)=0 THEN curr!(i)=(curr!(i+1)+curr!(i+2) + curr!(i+3)) / 3
  pd = pot!(i) - E0!
  IF pot!(1) - pot!(2) < 0 THEN pd = -pd
  IF i > ndps / 2 THEN pd = -pd
  term1! = 1 + c * EXP(constant! * (pd))
  term2! = seml - sem!(i) * term1!
  term3! = (term2! / curr!(i))
IF term3! <= 0 THEN       'term3! = 10 ^ (-5)
  RateK(i) = 0
ELSE
  RateK(i) = -LOG(term3!)
  IF ini = 0 THEN ini = i
END IF
NEXT
              'ini is initial data point
fini = ini + 5        'on which linear regression is performed
linet = &HF0F0 ' line type
    CALL graph(pot!(), RateK(), ndps, try$, try$)
stepp = 5
COLOR 15
LOCATE 23, 17: PRINT SPACE$(40): LOCATE 24, 17: PRINT SPACE$(40);
CALL prcomm("+/- to move, Step (2-9), ESC ")
LOCATE 24, 25: PRINT "Step speed: ";
```

```
PRINT stepp;
        COLOR 14
        LOCATE 4, 52: PRINT "Slope";
        LOCATE 4, 60: PRINT "Potential";
        COLOR 15
123 DO
  char$ = INKEY$
   IF char$ = CHR$(27) THEN     'if ESC is pressed then redraw and exit
   CALL graph(pot(), curr(), ndps, "E/V", "i/uA")
   EXIT DO
  END IF
  IF char$ = "+" THEN   'if + is pressed advance background
   IF fini + 10 > = ndps THEN BEEP: GOTO 123
323  ini = ini + stepp
    fini = fini + stepp
    IF RateK(ini) = 0 THEN GOTO 323
      FOR i = 1 TO ndps / 2 STEP 2
       y = intercept + slope * pot!(i)
       PSET (pot!(i), y), colorold%(i)
      NEXT
       CALL drawline(colorold%(), intercept, slope)
       LOCATE 5, 52: PRINT USING "###.##"; slope;
       LOCATE 5, 60: PRINT USING "##.###"; pot!((ini + fini) / 2);
     END IF
    IF char$ = "-" THEN
    IF ini - 10 < 1 THEN BEEP: GOTO 123
324     ini = ini - stepp
       fini = fini - stepp
       IF RateK(ini) = 0 THEN GOTO 324
       FOR i = 1 TO ndps / 2 STEP 2
         y = intercept + slope * pot!(i)
         PSET (pot!(i), y), colorold%(i)
       NEXT
        CALL drawline(colorold%(), intercept, slope)
        LOCATE 5, 52: PRINT USING "###.##"; slope;
        LOCATE 5, 60: PRINT USING "##.###"; pot!((ini + fini) / 2);
  END IF
  IF "1" < char$ AND char$ < ":" THEN
     stepp = ASC(char$) - 48
     LOCATE 24, 25: PRINT "Step speed: ";
     PRINT stepp;
  END IF
LOOP
escape:
LOCATE 23, 17: PRINT SPACE$(40): LOCATE 24, 17: PRINT SPACE$(40);
LOCATE 1, 55: PRINT SPACE$(17): LOCATE 2, 55: PRINT SPACE$(17);
'=======================================
END SUB
```

```
'=========================================
' This subroutine is designed to read data in the BAS-100 format
' after it has been converted into an ASCII format using our modified
' version of BAS conversion program
'=========================================
SUB readbasdata (warningbeep%)
'open the specified data file
OPEN path$ + "\" + filename$ + ".dat" FOR INPUT AS #2
'notify if file is not found
IF ERR = 53 THEN CALL prcomm("File not found")
'input data and convert to this programs format until end of file
i = 1
WHILE NOT EOF(2)
  INPUT #2, pot(i), curr(i)
  pot(i) = pot(i) / 1000              'convert to V
  curr(i) = curr(i) * 1000000!        'Convert to uA
  i = i + 1
WEND
ndps = i - 1
CLOSE #2
'determine max and min's, then graph data
CALL minmax(pot(), curr(), ndps, minx, maxx, miny, maxy, xminc, xmaxc)
CALL graph(pot(), curr(), ndps, "E/V", "i/uA")
'=========================================
END SUB
'=========================================
' This subroutine is designed to read data in the program's format
' (ie. first line is dt, following lines contain pot(),curr(),sem()
'=========================================
SUB readdata (warningbeep%)
OPEN path$ + "\" + filename$ + ".dat" FOR INPUT AS #2
IF ERR = 53 THEN CALL prcomm("File not found")
INPUT #2, dt
i = 1
WHILE NOT EOF(2)
  INPUT #2, pot(i), curr(i), sem(i)
  i = i + 1
WEND
ndps = i - 1
CLOSE #2
CALL minmax(pot(), curr(), ndps, minx, maxx, miny, maxy, xminc, xmaxc)
CALL graph(pot(), curr(), ndps, "E/V", "i/uA")
CALL info(warningbeep%)
'=========================================
END SUB
'=========================================
' This subroutine is designed to restore the screen colors which
' which have been covered by a line
```

```
'=========================================
SUB restorel (x1, y1, x2, y2, slope, intercept)
'erase old line
  PSET (x1, y1), 0
  LINE -(x2, y2), 0
'restore old colors
  FOR i = 1 TO ndps / 2
    y = intercept + slope * pot!(i)
    PSET (pot!(i), y), colorold%(i)
  NEXT
'=========================================
END SUB
'=========================================
' This subroutine is designed to semi-integrate data
'=========================================
SUB semi (dummy%)
KEY OFF
'LOCATE 23, 30: PRINT "Wait for a monent, please."
'IF sem!(ndps / 2) < > 0 GOTO Plot
IF gma!(1) = 0 THEN CALL gamma
n = ndps
qq = 0
FOR k = 1 TO n / 2
summf! = 0
      FOR j = 1 TO k
      summf! = summf! + gma!(k - j) * SQR(dt) * curr!(j)
      NEXT
sem!(k) = summf!
qq = qq + 1
LOCATE 23, 20
IF qq = 1 THEN PRINT "|";
IF qq = 2 THEN PRINT "/";
IF qq = 3 THEN PRINT "-";
IF qq = 4 THEN PRINT "\"; : qq = 0
NEXT
qq = 0
FOR k = n / 2 + 1 TO n
summb! = 0
      FOR j = 1 + n / 2 TO k
      summb! = summb! + gma!(k - j) * SQR(dt) * curr!(j)
      NEXT
sem!(k) = summb! + sem!(n / 2)
qq = qq + 1
 LOCATE 23, 20
 IF qq = 1 THEN PRINT "|";
 IF qq = 2 THEN PRINT "\";
 IF qq = 3 THEN PRINT "-";
 IF qq = 4 THEN PRINT "/"; : qq = 0
```

```
NEXT
Plot:
CALL graph(pot!(), sem!(), ndps, try$, try$)
'determine II values....by pointing
CALL ratecon
LOCATE 23, 17: PRINT SPACE$(40): LOCATE 24, 17: PRINT SPACE$(40);
KEY ON
'=========================================
END SUB
'=========================================
' This subroutine was obtained from the TA program and is used
' during data aquisition
'     Subroutine sets up tables for conversion factors
'     Values are vertical gain in volts/division
'
'=========================================
SUB setuptables (VG(), TD())
     VG(22) = .005
     VG(23) = .01
     VG(24) = .02
     VG(25) = .05
     VG(26) = .1
     VG(27) = .2
     VG(28) = .5
     VG(29) = 1!
     VG(30) = 2!
     VG(31) = 5!
'   TD values are time/point in us
TD(16) = .01: TD(17) = .02: TD(18) = .04: TD(19) = .08: TD(20) = .2
TD(21) = .4:TD(22) = .8:TD(23) = 2!:TD(24) = 4!:TD(25) = 8!:TD(26) = 20!
TD(27) = 40!: TD(28) = 80!: TD(29) = 200!: TD(30) = 400!: TD(31) = 800!
TD(32) = 2000!: TD(33) = 4000!: TD(34) = 8000!: TD(35) = 20000!
TD(36) = 40000!: TD(40) = .1: TD(41) = 1!: TD(42) = 10!: TD(43) = 100!
TD(44) = 1000!: TD(45) = 10000!
'=========================================
END SUB
'=========================================
' This subroutine is designed to determine slope and intercept from
' two data points
'=========================================
SUB slopeintercept (x1, y1, x2, y2, slope, intercept)
  slope = (y1 - y2) / (x1 - x2)
  intercept = y1 - x1 * slope
'=========================================
END SUB
'=========================================
' This subroutine smooths pot(),curr() data using a 5 point
' smoothing routine
```

```
'=========================================
SUB smooth (warningbeep%)
' 5 point smoothing routine
FOR i = 1 TO ndps - 6
      curr(i+2) = (curr(i) + curr(i+1) + curr(i+3) + curr(i+4)) / 4
      pot(i + 2) = (pot(i) + pot(i + 1) + pot(i + 3) + pot(i + 4)) / 4
NEXT i
CALL graph(pot(), curr(), ndps, "E/V", "i uA")
CALL info(warningbeep%)
'=========================================
END SUB
'=========================================
' This subroutine was obtained from the TA program and allows a
' program pause for time seconds
'=========================================
SUB waiting (time)
WaitTime! = time
StartTime! = TIMER
DO
  TimeNow! = TIMER
LOOP UNTIL (TimeNow! - StartTime!) > = WaitTime!
'=========================================
END SUB
'=========================================
' This subroutine writes data to a file in the program's format
'=========================================
SUB writefile (warningbeep%)
OPEN path$ + "\" + filename$ + ".DAT" FOR OUTPUT AS #2
   PRINT #2, dt
   FOR i = 1 TO ndps
    PRINT #2, USING "####.###"; pot(i);
    PRINT #2, USING "  #.###^^^^^^"; curr(i);
    PRINT #2, USING "##.###^^^^^^"; sem(i)
   NEXT i
CLOSE #2
'=========================================
END SUB
```

APPENDIX B
CHRONOAMPEROMETRIC SIMULATION AND OPTIMIZATION
PROGRAM SOURCE CODE

```
'*************************************************************
'  This program is designed to determine the optimal value of
'  Theta based on a least-square best fit of experimental data
'  to simulated responses
'*************************************************************
dim cex(2,500),ut(3,4000),q(500)
screen 9,0
color 11,0
'function designed to determine normalized current at a unit cell
'microelectrode based on normalized time and theta (Shoup and
'Szabo, 1984)
def fnch(t3,theta)
        e=0.8862
        t1=0.2146
        s=0.7823
        t2=(3-2*theta)
        t=1/(t3^2)
        ch1=e*t3+0.7854
        ch2=t1*exp(-s*theta2*t2*t3)
        et=(-e*theta/(1-theta)+s*t1(theta^2)*t2)*t3
        if et<-60 then et=-60
        ch3##=-exp(et)/(1+2.6587*theta^3/(t*(1-theta)))
        fnch=ch1+ch2+ch3##
end def
gosub 5 'user input
gosub 20 'data input
gosub 25 'find max ss
locate 11,25
rr$="R=#.###^^^^ cm2"
aa$="a=#.###^^^^ cm2"
tt$="Theta=##.###"
qq$="Rmax=#.###^^^^ cm"
zz$="Rmin=#.###^^^^ cm"
ttt=1-(aamax/rmax)^2
locate 11,25:print using rr$;rmax
locate 12,25:print using aa$;aamax
locate 13,25:print using tt$;ttt
```

```
locate 18,25:print using qq$;r
locate 19,25:print using zz$;rr
locate 23,1:input "Do you want simulation output [Y]";un$
if yn$="N" or yn$="n" then stop
gosub 98
999 end
'*********************************************************
' End of Program
'*********************************************************
'=========================================
25'                output sum of squares
'=========================================
rr=sqr(area)/3.141
lrr=log10(rr)/50
lr=lrr
ssmax=0
rmax=0
aamax=0
ttt$="### %"
sss$="maximum SS=#.###^^^^"
tht$="Theta= #.###"
q=0
for ii=1 to 50
        lr=lr+lrr
        aa=0
        r=exp10(lr)
        tn=area/(3.141*r^2)
        locate 10,24:print using ttt$;ii*100/50
        junk=r/50
for jjj=1 to 49
        aa=aa+junk
        gosub 40
        if ssmax<ss then
                locate 11,24:print using sss$;ss
                locate 12,24:print using tht$;1-(aa/r)^2
                ssmax=ss
                rmax=r
                aamax=aa
        end if
next jjj
next ii
'=========================================
return
'=========================================
'=========================================
5 cls'          user input
'=========================================
print"This program is designed to simulate chronoamperomet"
```

```
input"Press ENTER to continue";yn$
nn=1                              'Default prameters
co=4.001e-6
d=7.63e-6
area=0.068
input"Do you want the electrode area to be determined from CC data [Y]";yn$
10 cls
print"These are the default parameters.";
scic$="C=#.##^^^^ mole/cm3"
scid$="D=#.##^^^^ cm2/s"
area$="A=#.#### cm@"
nn$="n=#"
print using nn$;nn
print using scic$;co
print using scid$;D
if yn$="N" or yn$="n" then print using area$;area
print ""
print ""
input "Do you want to change anything [N]";yn2$
        if yn2$="y" or yn2$="Y" then
                cls
                print using nn$;nn;
                input nnn
                        if nnn<>0 then nn=nnn
                print using scic$;co;
                input coo
                        if coo<>0 then co=coo
                print using scid$;d;
                input dd
                        if dd<>0 then d=dd
        if yn$="N" or yn$="n" then
                print using area$;area;
                input areao
                        if areao<>0 then area=areao
        end if
                goto 10
        end if
cca$=yn$
'=========================================
return
'=========================================
'=========================================
20'                     data input
'=========================================
input"What directory is you data in";p$
p$="c:\mike"
p$=p$+"\"
cls
```

```
junk$="dir "+p$+"*.dat/w"
'shell junk$
input"Which file contains your data (extension assumed)";fl$
fl$="etccf"
input"Which file contains your background (ENTER if none)";bk$
bk$="etccb"
input"What was the pulse width [500 ms]";pw
if pw=0 then pw=500
open p$+fl$+".dat" for input as #1
2
input #1,junk
for j=1 to pw              'input CC data
        input #1, cex(1,j), cex(2,j)
next j
30 close #1
jj=j

if bk$<>"" then        'if background read and subtract
        open p$+bk$+".dat" for input as #1
        input #1,junk
        for j=1 to pw
                input #1, bk
                cex(2,j)=cex(2,j)-bk
        next j
end if
 if cca$<>"N" or cca$<>"n" then gosub 22
'=========================================
return
'=========================================
'=========================================
40'                    sum squares
'=========================================
thet=(1-(aa/r)^2)
tot=0
last=0
for k=1 to pw-1 step pw/10
        omt=1-thet
        tau=4*d*cex(1,k)/((aa^2)*1000)
        tau2=1/sqr(tau)
        sim=fnch(tau2,thet)
        q=3.859e5*d*aa*nn*co*sim*tn
        q(k)=q+last
        last=q(k)
next k
for k=1 to pw-1 step pw/10
        diff=((cex(2,k)-q(k))/q(k))^2          'square of the difference normalized
        tot=tot+diff
next k
```

```
ss=1/tot
'=========================================
return
'=========================================
'=========================================
98                      'output best simulation
'=========================================
thet=1-(aamax/rmax)^2
taum=4*d/(aamax^2)
dtau=taum/pw
taut=0
open p$+"sim.dat" for output as #3
zow2=1-thet
last=0
for ii=1 to pw
        taut=taut+dtau
        zow=1/sqr(taut)
        cen2=fnch(zow,thet)
        cen2=cen2*area*d*nn*co*zow2/(8.140e-6*aamax)+last
        print #3,cex(1,ii),cen2
        last=cen2
next ii
close #3
'=========================================
return
'=========================================
'=========================================
22'                     determine area from CC data
'=========================================
sxy=0
sx=0
sy=0
sx2=0
for j=1 to pw
        x=sqr(cex(1,j))
        y=cex(2,j)
        sxy=sxy+x*y
        sx=sx+x
        sy=sy+y
        sx2=sx2+x^2
next j
slope=(pw*sxy-sx*sy)/(pw*sx2-sx^2)
slope=abs(slope)
area=slope*5.809e-4/(2*nn*sqr(d)*co*1e6)
'=========================================
return
'=========================================
```

APPENDIX C
CYCLIC VOLTAMMETRIC SIMULATION PROGRAM SOURCE CODE

```
'*************************************************************************
' Variable important throughout the program include:
'       fanew() and fbnew() - new value of normalized concentration in each volume
'               element of reactant and product, respectively
'       faold() and  fbold() - old value of normalized concentration in each volume
'               element of reactant and product, respectively
'       z() - normalized current
'       e() - normalized potential
'       surf() - normalized conentration in first volume element
'       de - change in normalized potential
'       Kaads and Kbads - equilibrium constant between first and second volume
'               element of reactant and product, respectively
'*************************************************************************
DECLARE SUB maxmin (n!, x(), y(), maxx!, minx!, maxy!, miny!)
CLEAR 4001
SCREEN 12
11 CLS
'*************************************************************************
'setup arrays and model variables
'*************************************************************************
DIM faold(4000), fanew(4000), fbold(4000), fbnew(4000), z(4000), e(4000), surf(4000)
'*************************************************************************
'common constants
'*************************************************************************
R = 8.31441: T = 298: F = 96485: n = 1: v = 1
A = .01: D = .00001: c0 = .000001
'*************************************************************************
'normalize potential (assume Eo'=0)
'*************************************************************************
ei = 7
e(0) = ei
'*************************************************************************
'input initial parameters
'*************************************************************************
LOCATE 1, 1: PRINT SPACE$(40)
LOCATE 1, 1: INPUT "de (0.1)= "; de: IF de = 0 THEN de = .1
LOCATE 1, 1: PRINT SPACE$(40)
LOCATE 1, 1: INPUT "Ka,ads (0)= "; Kaads
```

```
LOCATE 2, 1: INPUT "Kb,ads (0)= "; Kbads
l = 2 * ei / de
dma = .45
dmb = dma
nvemax = 6 * SQR(l)
nve = 50'nvemax / 2
zmax = .6
redraw = 1
dde = ABS(ei) / 10
dda = 0
ddb = 0
'*************************************************************************
'initial conditions
'*************************************************************************
FOR j = 1 TO 2
  faold(j) = 1
  fanew(j) = 1
  fbold(j) = 0
  fbnew(j) = 0
NEXT
'*************************************************************************
'adjust surface concentrations of a and b
'*************************************************************************
IF Kaads < > 0 THEN dda = ABS((fanew(2) * Kaads - fanew(1)) / (Kaads + 1))
fanew(1) = fanew(1) + dda * 2 * dma
fanew(2) = fanew(2) - dda * 2 * dma
IF Kbads < > 0 THEN ddb = ABS((fbnew(2) * Kbads - fbnew(1)) / (Kbads + 1))
fbnew(1) = fbnew(1) + ddb * 2 * dmb
fbnew(2) = fbnew(2) - ddb * 2 * dmb
IF dda > ddb THEN
  scale = dda
ELSE
  scale = ddb
END IF
FOR j = 2 TO l
  faold(j) = 1
  fanew(j) = 1
  fbold(j) = 0
  fbnew(j) = 0
NEXT
VIEW (60, 50)-(110, 400), , 12
WINDOW (0!, 0!)-(1.05, 1 + scale)
   FOR z = 2 TO nve
    LINE (z / nve, 1 + scale)-(z / nve, 1), 1
   NEXT
k = 0
zot = 0 'used in progress
'*************************************************************************
```

```
'start iteration loop
'*************************************************************************
WHILE k < 2 * l
  k = k + 1
'*************************************************************************
'change potential
'*************************************************************************
  e(k) = e(k - 1) - de
'*************************************************************************
'adsorption
'*************************************************************************
IF Kaads < > 0 THEN
  da = (fanew(2) * Kaads - fanew(1)) / (Kaads + 1)  'change in concentration
  fanew(1) = fanew(1) + da
  fanew(2) = fanew(2) - da
END IF
IF Kbads < > 0 THEN
  db = (fbnew(2) * Kbads - fbnew(1)) / (Kbads + 1)  'change in concentration
  fbnew(1) = fbnew(1) + db
  fbnew(2) = fbnew(2) - db
END IF
'*************************************************************************
'convert surface concentrations based on nernst
'*************************************************************************
  nern = EXP(e(k))
  df = (fanew(1) - nern * fbnew(1)) / (nern + 1)    'change in concentration
  zz = df * dma * 2
  z(k) = zz / SQR(dma * ABS(de))
'*************************************************************************
'Setup old arrays for next iteration
'*************************************************************************
  FOR j = 1 TO nvemax'l
    faold(j) = fanew(j)
    fbold(j) = fbnew(j)
  NEXT
    surf(k) = fbnew(1) + df
'*************************************************************************
'Diffusion into the first block
'*************************************************************************
    fanew(1) = faold(1) + dma * (faold(2) - faold(1)) - zz
    fbnew(1) = fbold(1) + dmb * (fbold(2) - fbold(1)) + zz
'*************************************************************************
'Diffusion beyond the first box
'*************************************************************************
  FOR j = 2 TO nvemax'l
    fanew(j) = faold(j) + dma * (faold(j - 1) - 2 * faold(j) + faold(j + 1))
    fbnew(j) = fbold(j) + dmb * (fbold(j - 1) - 2 * fbold(j) + fbold(j + 1))
  NEXT
```

```
IF k = 1 THEN de = -de
'*************************************************************************
'  show progress ( the growth of diffusion layer)
'*************************************************************************
IF k * 100 / 1 > zot THEN    'if at least 1% of calculations
   zot = zot + 1                    'has been completed show progress
   VIEW (60, 50)-(110, 400), , 12
   WINDOW (0!, 0!)-(1.05, 1 + scale)
   FOR z = 1 TO nve
     hi! = fanew(z)
     LINE (z / nve, 1 + scale)-(z / nve, hi!), 1
     LINE -(z / nve, 0), 2
   NEXT
END IF
'*************************************************************************
'show progress (normalized current)
'*************************************************************************
 IF ABS(z(k)) > zmax THEN redraw = 1
 VIEW (110, 50)-(510, 400), , 12
 WINDOW (-ABS(ei) - dde, -zmax)-(ABS(ei) + dde, zmax)
   IF redraw = 1 THEN
     'erase old cv
     PSET (e(1), z(1)), 0
     FOR z = 2 TO k
       LINE (e(z - 1), z(z - 1))-(e(z), z(z)), 0
     NEXT
     'reset maximum z
     zmax = zmax + .2
     'reset window
     WINDOW (-ABS(ei) - dde, -zmax)-(ABS(ei) + dde, zmax)
     'redraw z
     PSET (e(1), z(1)), 14
     FOR z = 2 TO k
       LINE (e(z - 1), z(z - 1))-(e(z), z(z)), 14
     NEXT
     redraw = 0
  ELSE
     LINE (e(k - 1), z(k - 1))-(e(k), z(k)), 14
   END IF
WEND
LOCATE 1, 1: PRINT SPACE$(40) 'clear progress
CALL maxmin(l, z(), e(), maxi, mini, maxe, mine)
LOCATE 1, 1: PRINT maxi, 1 - surf(l)
LOCATE 2, 2: INPUT "continue"; yn$: IF UCASE$(yn$) = "N" THEN GOTO dataout
LOCATE 2, 1: PRINT SPACE$(40) 'clear progress
GOTO 11
'*************************************************************************
dataout:                    'output results
```

```
'*********************************************************************
LOCATE 1, 1: PRINT SPACE$(40)
LOCATE 1, 1: INPUT "d:\path\filename (no extention): "; filename$
IF filename$ = "" THEN GOTO quit
OPEN filename$ + ".dat" FOR OUTPUT AS #1
PRINT #1, ABS(e(1) - e(2)) * R * T / (n * F * v)
FOR k = 1 TO 2 * l
  PRINT #1, e(k) * R * T / (n * F);
  PRINT #1, z(k) * c0 * SQR(D * v) * A * n ^ (1.5) * 6.02E+11;
  PRINT #1, (surf(k)) * c0 * n * F * A * SQR(D) * 1000000!
NEXT
CLOSE
'*********************************************************************
'*********************************************************************
quit:             'exit program
'*********************************************************************
END
'*********************************************************************
'End of Program
'*********************************************************************
'=========================================
SUB maxmin (n, x(), y(), maxx, minx, maxy, miny)
'=========================================
'n=number of data points
'x()=x array
'y()=y array
'max?=array maximum
'min?=array minimum
maxx = minx = x(1)
maxy = miny = y(1)
FOR j = 1 TO n
  IF maxx < x(j) THEN maxx = x(j)
  IF maxy < y(j) THEN maxy = y(j)
  IF minx > x(j) THEN minx = x(j)
  IF miny > y(j) THEN miny = y(j)
NEXT
'=========================================
END SUB
'=========================================
```

REFERENCE LIST

Albery, W.J. *Electrode Kinetics*; Clarendon: Oxford, 1975.

Albery, W.J.; Bartlett, P.N. An organic conductor electrode for the oxidation of NADH, *J. Chem. Soc. Chem. Comm.*, **1984**, 234-236.

Albery, W.J.; Bartlett, P.N. Amperometric enzyme electrodes. Part I. Theory, *J. Electroanal. Chem.*, **1985**, *194*, 211-222.

Albery, W.J.; Bartlett, P.N.; Craston, D.H. Amperometric enzyme electrodes. Part II. Conducting salts as electrode materials for the oxidation of glucose oxidase, *J. Electroanal. Chem.*, **1985**, *194*, 223-235.

Albery, W.J.; Bartlett, P.N.; Cass, A.E.G; Craston, D.H.; Haggett, B.G.D. Amperometric enzyme electrodes, *J. Chem. Soc. Faraday Trans. 1*, **1986**, *82*, 1033.

Albery, W.J.; Bartlett, P.N.; Bycroft, M.; Craston, D.H.; Driscoll, B.J. Amperometric enzyme electrodes. Part III. A conducting salt electrode for the oxidation of four different flavoenzymes, *J. Electroanal. Chem.*, **1987a**, *218*, 119-126.

Albery, W.J.; Bartlett, P.N.; Cass, A.E.G. Amperometric enzyme electrodes, *Phil. Trans. R. Soc. Lond. B*, **1987b**, *316*, 107-119.

Albrecht, T.R.; Quate, C.F. Atomic resolution imaging of a nonconductor by atomic force microscopy, *J. Appl. Phys.*, **1987**, *62*, 2599-2602.

Amatore, C.; Savéant, J.-M.; Tessier, D. Charge transfer at partially blocked surfaces. A model for the case of microscopic active and inactive sites, *J. Electroanal. Chem.*, **1983**, *147*, 39-51.

Anderson, J.E.; Hopkins, D.; Shadrick, J.W.; Ren, Y. Apparatus for the fabrication of poly(chlorotrifluoroethylene) composite electrodes, *Anal. Chem.*, **1989**, *61*, 2330-2332.

Andrieux, C.P.; Blocman, C.; Dumas-Bouchiat, J.-M.; Savéant, J.-M. Heterogeneous and homogeneous electron transfer to aromatic halikes. An electrochemical redox catalysis study in the halobenzene and halopyridine series, *J. Am. Chem. Soc.*, **1979**, *101*, 3431-3441.

Andrieux, C.P.; Garreau, D.; Hapiot, P.; Pinson, J.; Savéant, J.-M. Fast sweep cyclic voltammetry at ultra-microelectrodes. Evaluation of the method for fast electron-transfer kinetic measurements, *J. Electroanal. Chem.*, **1988**, *243*, 321-335.

Andrieux, C.P.; Hapiot, G.P.; Savéant, J.M. Fast kinetics by means of direct and indirect electrochemical techniques, *Chem. Rev.*, **1990**, *90*, 723-738.

Andrieux, C.P.; Savéant, J.-M. In *Investigation of Rates and Mechanisms of Reactions*; Bernasconi, C.F., Ed.; Wiley & Sons: New York, 1986; Chapter 7.

Anson, F.C. Innovations in the study of adsorbed reactants by chronocoulometry, *Anal. Chem.*, **1966**, *38*, 54-57.

Aoki, K.; Osteryoung, J. Diffusion-controlled current at the stationary finite disk electrode, *J. Electroanal. Chem.*, **1981**, *122*, 19-35.

Bard, A.J.; Faulkner, L.R. *Electrochemical Methods: Fundamentals and Applications*; Wiley & Sons: New York, 1980.

Beck, F.; Junge, H.; Krohn, H. Graphite intercalation compounds as positive electrodes in galvanic cells, *Electrochim. Acta*, **1981**, *26*, 799-809.

Binnig, G.; Rohrer, H. Scanning tunneling microscopy, *IBM J. Res. Develop.*, **1986**, *30*, 355-369.

Binnig, G.; Quate, C.F.; Gerber, Ch. Atomic force microscope, *Phy. Rev. Lett.*, **1986**, *56*, 930-933.

Bockris, J.O'M.; Nagy, Z. Symmetry factor and transfer coefficient, *J. Chem. Ed.*, **1973**, *50*, 839-843.

Bodalbhai, L.; Brajter-Toth, A. Scanning electron microscopy in the analysis of the activity of graphite electrodes, *Anal. Chim. Acta*, **1990**, *231*, 191-201.

Bottom, V.E. *Introduction to Quartz Crystal Unit Design*; Van Nostrand Reinhold: New York, 1982.

Bowling, R.; McCreery, R.L. Diagnosis of adsorption on solid electrodes with semi-integral voltammetry, *Anal. Chem.*, **1988**, *60*, 605-608.

Bowling, R.; Packard, R.T.; McCreery, R.L. Mechanism of electrochemical activation of carbon electrodes: role of graphite lattice defects, *Langmuir*, **1989a**, *5*, 683-688.

Bowling, R.J.; Packard, R.T.; McCreery, R.L. Activation of highly ordered pyrolytic graphite for heterogeneous electron transfer: Relationship between electrochemical performance and carbon microstructure, *J. Am. Chem. Soc.*, **1989b**, *111*, 1217-1223.

Buttery, D.A. In *Electroanalytical Chemistry*; Bard, A.J., Ed.; Marcel Dekker: New York, 1991; Vol. 17; Chapter 1.

Cabaniss, G.E.; Diamantis, A.A.; Murphy, W.R.; Linton, R.W.; Meyer, T.J. Electrocatalysis of proton-coupled electron-transfer reactions at glassy carbon electrodes. *J. Am. Chem. Soc.*, **1985**, *107*, 1845-1853

Calvo, E.J. In *Comprehensive Chemical Kinetics*; Bamford, C.H.; Compton, R.G., Eds.; Vol. 26; Elsevier: New York, 1986; Chapter 1.

Cenas, N.K.; Kulys, J.J. Biocatalytic oxidation of glucose on the conductive charge transfer complexes, *Bioelectrochem. Bioenerg.*, **1981**, *8*, 103-113.

Chang, H.; Bard, A.J. Formation of monolayer pits of controlled nanometer size on highly oriented pyrolytic graphite by gasification reactions as studied by scanning tunneling microscopy, *J. Am. Chem. Soc.*, **1990**, *112*, 4598-4599.

Conway, B.E. *Theory and Principles of Electrode Processes*; Ronald: New York, 1965.

Cowlard, F.C.; Lewis, J.C. Vitreous carbon- a new form of carbon, *J. Mater. Sci.*, **1967**, *2*, 507-512.

Deakin, M.R.; Kovach, P.M.; Stutts, K.J.; Wightman, R.M. Heterogeneous mechanisms of the oxidation of catechols and ascorbic acid at carbon electrodes, *Anal. Chem.*, **1986**, *58*, 1474-1480.

Dong, S.; Kuwana, T. Activation of glassy carbon electrodes by dispersed metal oxide particles, *J. Electrochem. Soc.*, **1984**, *131*, 813-819.

Dryhurst, G.; McAllister, D.L. In *Laboratory techniques in Electroanalytical Chemistry*; Kissinger, P.T., Heineman, W.R., Eds.; Marcel Dekker: New York, 1984; Chapter 10.

Engstrom, R.C. Electrochemical pretreatment of glassy carbon electrodes, *Anal. Chem.*, **1982**, *54*, 2310-2314.

Engstrom, R.C.; Strasser, V.A. Characterization of electrochemically pretreated carbon electrodes, *Anal. Chem.*, **1984**, *56*, 136-141.

Evans, J.F.; Kuwana, T. Radiofrequency oxygen plasma treatment of pyrolytic graphite electrode surfaces, *Anal. Chem.*, **1977**, *49*, 1632-1635.

Fagan, D.T.; Hu, I.F.; Kuwana, T. Vacuum heat treatment for activation of glassy carbon electrodes, *Anal. Chem.*, **1985**, *57*, 2759-2763.

Feldberg, S.W. In *Computers in Chemistry and Instrumentation*; Mattson, J.S., Mark, H.B., MacDonald, H.C., Eds.; Marcel Dekker: New York, 1972; Vol. 2; Chapter 7.

Ferraris, J.; Cowan, D.O.; Walatka, V.; Perlstein, J. Electron transfer in a New Highly Conducting Donor-Acceptor Complex, *J. Am. Chem. Soc.*, **1973**, *95*, 948-949.

Freund, M.S. Determination of surface excess and surface concentration in the presence of weak adsorption using semi-integral analysis of cyclic voltammetry, *J. Electrochem. Soc.*, **1992**, *139*, 8C-13C.

Freund, M.S.; Bodalbhai, L.; Brajter-Toth, A. Anion-excluding polypyrrole films, *Talanta*, **1991**, *38*, 95-99.

Freund, M.S.; Brajter-Toth, A. Ultramicroelectrode array behavior of one dimensional organic conductor electrodes, *Anal. Chem.*, **1989**, *61*, 1048-1052.

Freund, M.S.; Brajter-Toth, A.; Ward, M.D. Electrochemical and quartz crystal microbalance evidence for mediation and direct electrochemical reactions of small molecules at tetrathiafulvalene-tetracyanoquinodimethane (TTF-TCNQ) electrodes, *J. Electroanal. Chem.*, **1990**, *289*, 127-141.

Freund, M.S.; Brajter-Toth, A. Determination of ultramicroelectrode array dimensions at graphite and one-dimensional organic conductor electrodes, *J. Electroanal. Chem.*, **1991**, *300*, 347-363.

Freund, M.S.; Brajter-Toth, A. Semi-integral analysis in voltammetry: Determination of surface excess and concentration in presence of weak adsorption and thin films, submitted for publication in *J. Phys. Chem.*

Freund, M.S.; Brajter-Toth, A.; Cotton, T.M.; Henderson, E.R.; Scanning tunneling mocroscopy and atomic force microscopy in the characterization of activated graphite electrodes, *Anal. Chem.*, **1991**, *63*, 1047-1049.

Gerhardt, G.; Adams, R.N. Determination of diffusion coefficients by flow injection analysis, *Anal. Chem.*, **1982**, *54*, 2618-2620.

Gewirth, A.A.; Bard, A.J. In situ scanning tunneling microscopy of the anodic oxidation of highly oriented pyrolytic graphite surfaces, *J. Phys. Chem.*, **1988**, *92*, 5563-5566.

Gueshi, T.; Tokuda, K.; Matsuda, H. Voltammetry at partially covered electrodes. Part I. Chronopotentiometry and chronoamperometry at model electrodes, *J. Electroanal. Chem.*, **1978**, *89*, 247-260.

Hale, P.D.; Skotheim, T.A. Cyclic voltammetry at TCNQ and TTF-TCNQ modified platinum electrodes: A study of the glucose oxidase/glucose and galactose oxidase/glactose systems, *Synth. Met.*, **1989**, *28*, C853-C858.

Hale, P.D.; Wightman, R.M. Enzyme-modified tetrathiafulvalene tetracyanoquinodimethane microelectrodes: Direct amperometric detection of acetylcholine and choline, *Mol. Cryst. Liq. Cryst.*, **1988**, *160*, 269-279.

Hill, B.S.; Scolari, C.A.; Wilson, G.S. Enzyme electrocatalysis at organic salt electrodes, *J. Electroanal. Chem.*, **1988**, *252*, 125-138.

Hu, I.F.; Karweik, D.H.; Kuwana, T. Activation and deactivation of glassy carbon electrode, *J. Electroanal. Chem.*, **1985**, *188*, 59-72.

Hu, I.F.; Kuwana, T. Oxidative mechanism of ascorbic acid at glassy carbon electrodes, *Anal. Chem.*, **1986**, *58*, 3235-3239.

Imbeaux, J.C.; Saveant, J.-M. Convolutive potential sweep voltammetry: Introduction, *J. Electroanal. Chem.*, **1973**, *44*, 169-187.

Jaeger, C.D.; Bard, A.J. Electrochemical behavior of tetrathiafulvalene-tetracyanoquinodimethane electrodes in aqueous media, *J. Am. Chem. Soc.*, **1979**, *101*, 1690-1699.

Jaeger, C.D.; Bard, A.J. Electrochemical behavior of donor-tetracyanoquinodimethane electrodes in aqueous media, *J. Am. Chem. Soc.*, **1980**, *102*, 5435-5442.

Jenkins, G.M.; Kawamura, K. Structure of glassy carbon, *Nature*, **1971**, *231*, 175-176.

Kazee, B.; Weisshaar, D.E.; Kuwana, T. Evidence for the presence of a thin carbon-particle layer on polished glassy carbon electrodes, *Anal. Chem.*, **1985**, *57*, 2739-2740.

Kepley, L.J.; Bard, A.J. Ellipsometric, electrochemical, and elemental characterization of the surface phase produced on glassy carbon electrodes by electrochemical activation, *Anal. Chem.*, **1988**, *60*, 1459-1467.

Kinoshita, K. *Carbon: Electrochemical and Physicochemical Properties*; Wiley & Sons: New York, 1988.

Kovach, P.M.; Deakin, M.R.; Wightman, R.M. Electrochemistry at partially blocked carbon-fiber microcylinder electrodes, *J. Phys. Chem.*, **1986**, *90*, 4612-4617.

Kovach, R.M.; Ewing, A.G.; Wilson, R.L.; Whightman, R.M. In vitro comparison of selectivity of electrodes for in vivo electrochemistry, *J. Neurosci. Meth.*, **1984**, *10*, 215-227.

Kulys, J.J.; Svirmickas, G.J.S. Reagentless lactate sensor based on cytochrome b2, *Anal. Chim. Acta*, **1980**, *117*, 115-120.

Laveron, E. In *Electroanalytical Chemsitry*; Bard, A.J., Ed.; Marcel Dekker: New York, 1982; Vol. 12.

Lu, C.; Lewis, O. Investigation of film-thickness determination by oscillating quartz resonators with large mass load, *J. Appl. Phys.*, **1972**, *43*, 4385-4390.

Maeda, Y.; Okemoto, Y.; Inagaki, M. Electrochemical formation of graphite-sulfuric acid intercalation compounds on carbon fibers, *J. Electrochem. Soc.*, **1985**, *132*, 2369-2372.

Massart, D.L.; Vandeginste, B.G.M.; Deming, S.N.; Michotte, Y.; Kaufman, L. *Chemometrics: A Textbook*; Elsevier: New York, 1988; Chapter 5.

Matsuda, H.; Ayabe, Y. Zur Theorie der Randles-Sevcikschen Kathodenstrahl-Polarography, *Z. Elektrochem.*, **1955**, *59*, 494.

Melby, L.R.; Harder, R.J.; Hertler, W.R.; Mahler, W.; Benson, R.E.; Mochel, W.E. Substituted quinodimethans. II. Anion-radical derivatives and complexes of 7,7,8,8,-tetracyanoquinodimethane, *J. Am. Chem. Soc.*, **1962**, *84*, 3374-3387.

McCreery, R.L. In *Electroanalytical Chemistry*; Bard, A.J., Ed.; Marcel Dekker: New York, 1991; Vol. 17; pp. 221-374.

McKenna, K.; Boyette, S.E.; Brajter-Toth, A. Electrochemical behavior of small biological molecules at organic donor-acceptor electrodes in aqueous media, *Anal. Chim. Acta*, **1988**, *206*, 75-84.

McKenna, K.; Brajter-Toth, A. Tetrathiafulvalene tetracyanoquinodimethane xanthine oxidase amperometric electrode for the determination of biological purines, *Anal. Chem.*, **1987**, *59*, 954-958.

Nagaoka, T.; Fukunaga, T.; Yoshino, T.; Watanabe, I.; Nakayama, T.; Okazaki, S. Uptake on ions into electrochemically treated glassy carbon, *Anal. Chem.*, **1988**, *60*, 2766-2769.

Nagaoka, T.; Yoshino, T. Surface properties of electochemically pretreated glassy carbon, *Anal. Chem.*, **1986a**, *58*, 1037-1042.

Nagaoka, T.; Yoshino, T. Oxygen reduction at electrochemically treated glassy carbon electrodes, *Anal. Chem.*, **1986b**, *58*, 1953-1955.

Naoi, K.; Lien, M.M.; Smyrl, W.H. Quartz crystal microbalance analysis. Part I. Evidence of anion or cation insertion into electropolymerized conducting polymers, *J. Electroanal. Chem.*, **1989**, *272*, 273-275.

Nicholson, R.S. Theory and application of cyclic voltammetry of measurement of electrode reaction kinetics, *Anal. Chem.*, **1965**, *37*, 1351-1355.

Nicholson, R.S.; Shain, I. Theory of stationary electrode polarography single scan and cyclic methods applied to reversible, irreversible and kinetic systems, *Anal. Chem.*, **1964**, *36*, 706-723.

Oldham, K.B. Analytical expressions for the reversible Randles-Sevcik function, *J. Electroanal. Chem.*, **1979**, *105*, 373-375.

Oldham, K.B. Edge effects in semi-infinite diffusion, *J. Electroanal. Chem.*, **1981**, *122*, 1-17.

Parsons, R. The structure of the mercury-electrolyte interphase in the presence of thiourea, *Proc. Roy. Soc. (London)*, **1961**, *A261*, 79-90.

Parsons, R. Electrical double layer: recent experimental and theoretical developments, *Chem. Rev.*, **1990**, *90*, 813-826.

Penner, R.M.; Martin, C.R. Preparation and electrochemical characterization of ultramicroelectrode ensembles, *Anal. Chem.*, **1987**, *59*, 2625-2630.

Poon, M.; McCreery, R.L. In situ laser activation of glassy carbon electrodes, *Anal. Chem.*, **1986**, *58*, 2745-2750.

Reller, H.; Kirowa-Eisner, E.; Gileadi, E. Ensembles of microelectrodes. A digital simulation, *J. Electroanal. Chem.*, **1982**, *138*, 65-77.

Rugar, D.; Hansma, P. Atomic force microscopy, *Physics Today*, **1990**, *Oct.*, 23-30.

Salt, D. *Hy-Q Handbook of Quartz Crystal Devices*; Van Nostrand Reinhold: New York, 1987.

Sauerbrey, G. Verwendung von schwingquarzen sur wagung dunner schichten und sur mikrowagung, *Zeit. Phys.*, **1959**, *155*, 206-222.

Savéant, J.-M.; Tessier, D. Convolution potential sweep voltammetry: Determination of charge transfer kinetics deviating from the butler-volmer behaviour, *J. Electroanal. Chem.*, **1975**, *65*, 57-66.

Shoup, D.; Szabo, A. Chronoamperometry at an ensemble of microdisk electrodes, *J. Electroanal. Chem.*, **1984**, *160*, 19-26.

Sleszynski, N.; Osteryoung, J. Arrays of very small voltammetric electrodes based on reticulated vitreous carbon, *Anal. Chem.*, **1984**, *56*, 130-135.

Smyrl, W.H.; Atanasoski, R.T.; Atanasoska, L.; Hartshorn, L.; Lien, M.; Nygren, K.; Fletcher, E.A. Morphology changes due to anodic treatment of glassy carbon electrodes, *J. Electroanal. Chem.*, **1989**, *264*, 301-304.

Spanier, J.; Oldham, K.B. *Atlas of Functions*; Hemisphere: New York, 1987; p 411.

Spiro, M. In *Comprehensive Chemical Kinetics*; Compton, R.G., Ed.; Elsevier: New York, 1989; Vol. 28, 69-159.

Sternitzke, K.D.; McCreery, R.L. Laser microfabrication and activation of graphite and glassy carbon electrodes, *Anal. Chem.*, **1990**, *62*, 1339-1344.

Stockbridge, C.D. In *Vacuum Microbalance Techniques*; Behrndt, K., Ed.; Plenum: New York, 1966; Vol. 5.

Strohben, W.E.; Smith, D.K.; Evans, D.H. Characterization of arrays of microelectrodes for fast voltammetry, *Anal. Chem.*, **1990**, *62*, 1709-1712.

Stutts, K.L.; Kovach, P.M.; Kuhr, W.G.; Wightman, R.M. Enhanced electrochemical reversibility at heat-treated glassy carbon electrodes, *Anal. Chem.*, **1983**, *55*, 1632-1634.

Tokuda, K.; Morita, K.; Shimizu, Y. Cyclic voltammetry at microhole array electrodes, *Anal. Chem.*, **1988**, *61*, 1763-1768.

Wang, J.; Tuzhi, P. Enhanced stability of glassy carbon detectors following a simple electrochemical pretreatment, *Anal. Chem.*, **1986**, *58*, 1787-1790.

Wang, J.; Lin, M.S. In situ electrochemical renewal of glassy carbon electrodes, *Anal. Chem.*, **1988**, *60*, 499-502.

Wang, J.; Martinez, T.; Yaniv, D.R.; McCormick, L.D. In situ characterization of electrochemically activated glassy carbon electrodes with scanning tunneling microscopy, *J. Electroanal. Chem.*, **1990**, *278*, 379-386.

Ward, M.D. Investigation of open circuit reactions of polymer films using the quartz crystal microbalance. Reactions of polyvinylferrocene films, *J. Phys. Chem.*, **1988**, *92*, 2049-2054.

Ward, M.D. In *Electroanalytical Chemistry*; Bard, A.J., Ed.; Marcel Dekker: New York, 1989; Vol. 16.

Weaver, M.J. In *Comprehensive Chemical Kinetics*; Compton, R.G., Ed.; Elsevier: New York, 1987; Vol. 27, Chapter 1.

Weisshaar, D.E.; Tallman, D.E. Chronoamperometric response at carbon-based composite electrodes, *Anal. Chem.*, **1983**, *55*, 1146-1151.

Wightman, R.M.; Deakin, M.R.; Kovach, P.M.; Kuhr, W.G.; Stutts, K.J. Methods to improve electrochemical reversibiliby at carbon electrodes, *J. Electrochem. Soc.*, **1984**, *131*, 1578-1583.

Wopschall, R.H.; Shain, I. Effects of adsorption of electroactive species in stationary electrode polarography, *Anal. Chem.*, **1967**, *39*, 1514-1527.

BIOGRAPHICAL SKETCH

Michael S. Freund was born on January 12, 1964, in Gainesville, Florida. He attended Gainesville High School and graduated in 1982. In the Fall of 1982 he began his undergraduate education in chemistry at Emory University in Atlanta, Georgia. In the Summer of 1985, he transferred to Florida Atlantic University in Boca Raton, Florida, where he continued his undergraduate education and began research under the supervision of Frank A. Schultz. He obtained his B.S. degree in chemistry in 1987.

Before entering graduate school he began research at the University of Florida under the supervision of Anna Brajter-Toth and participated in the du Pont Summer Research Program under the supervision of Michael D. Ward. While at the University of Florida his research has included collaborations with Therese M. Cotton and Eric R. Henderson at Iowa State University. In 1991 he received the Joseph W. Richards Fellowship of the Electrochemical Society, and in 1992 he received the Shell Fellowship. Mr. Freund completed his Ph.D. in analytical chemistry at the University of Florida in 1992 and will begin a postdoctoral fellowship at the California Institute of Technology.

I certify that I have read this study and that in my opinion it conforms to acceptable standards of scholarly presentation and is fully adequate, in scope and quality, as a dissertation for the degree of Doctor of Philosophy.

Anna Brajter-Toth, Chair
Associate Professor of Chemistry

I certify that I have read this study and that in my opinion it conforms to acceptable standards of scholarly presentation and is fully adequate, in scope and quality, as a dissertation for the degree of Doctor of Philosophy.

James Winefordner
Graduate Research Professor of Chemistry

I certify that I have read this study and that in my opinion it conforms to acceptable standards of scholarly presentation and is fully adequate, in scope and quality, as a dissertation for the degree of Doctor of Philosophy.

Vaneica Young
Associate Professor of Chemistry

I certify that I have read this study and that in my opinion it conforms to acceptable standards of scholarly presentation and is fully adequate, in scope and quality, as a dissertation for the degree of Doctor of Philosophy.

Dan Talham
Assistant Professor of Chemistry

I certify that I have read this study and that in my opinion it conforms to acceptable standards of scholarly presentation and is fully adequate, in scope and quality, as a dissertation for the degree of Doctor of Philosophy.

Christopher Batich
Professor of Materials Science
and Engineering

This dissertation was submitted to the Graduate Faculty of the Department of Chemistry in the College of Liberal Arts and Sciences and to the Graduate School and was accepted as partial fulfillment of the requirements for the degree of Doctor of Philosophy.

August 1992

_____

Dean, Graduate School